UNIVERSITÉ DE GRENOBLE

THÈSE

Pour obtenir le grade de

DOCTEUR DE L'UNIVERSITÉ DE GRENOBLE

Spécialité : **Physique de la Matière Condensée et du Rayonnement**

Arrêté ministérial : 7 août 2006

Présentée par

Paweł KWAŚNIEWSKI

Thèse dirigée par **Mme Catherine QUILLIET**

préparée au sein **de l'ESRF**
et de **l'Ecole Doctorale de Physique**

Etude en rayons X cohérents de la dynamique de suspensions concentrées de sphères dures

Thèse soutenue publiquement le **26/06/2012**,
devant le jury composé de :

M., Luigi CRISTOFOLINI
Associate Professor, University of Parma, Italy , Rapporteur

M., Doru CONSTANTIN
Chargé de Recherches CNRS, Laboratoire de Physique des Solides, Orsay, France, Rapporteur

Mme, Judith PETERS
Professeur, Université Joseph Fourier Grenoble, France , Examinateur

Mme, Catherine QUILLIET
Maître de Conférences, Université Joseph Fourier Grenoble, France , Directeur de thèse

M., Anders MADSEN
Group leader, European X-ray Free Electron Laser, Hamburg, Germany , Co-Directeur de thèse

M., Andrei FLUERASU
Group leader, Brookhave National Laboratory, Upton NY, USA , Co-Directeur de thèse

Université Joseph Fourier, Grenoble

EDPHYS DOCTORAL SCHOOL

ECOLE DOCTORALE DE PHYSIQUE

P H D T H E S I S

to obtain the title of

PhD of Science

of the Joseph Fourier University, Grenoble

Defended by

Paweł KWAŚNIEWSKI

Probing dynamics of hard sphere suspensions at high volume fractions with coherent X-rays

Thesis Advisor : Catherine QUILLIET

prepared at ESRF Grenoble

defended on June 26th, 2012

Jury :

Reviewers :	Luigi CRISTOFOLINI	-	University of Parma
	Doru CONSTANTIN	-	LPS, Orsay
Advisor :	Catherine QUILLIET	-	UJF (LiPhy)
Examinator :	Judith PETERS	-	UJF
Co-advisors :	Anders MADSEN	-	European XFEL (Hamburg)
	Andrei FLUERASU	-	NSLS II (BNL)

Contents

List of Figures

Acronyms

ASD	accelerated Stokesian dynamics
CRL	Compound Refractive Lenses
DLS	Dynamic Light Scattering
DWS	Diffusing Wave Spectroscopy
ESRF	European Synchrotron Radiation Facility
FCC	face centred cubic
HI	hydrodynamic interactions
ISF	intermediate scattering function
KWW	Kohlrausch-Williams-Watts
MCT	mode-coupling theory
OZ	Ornstein-Zernike
PCS	Photon Correlation Spectroscopy
PG	propylene glycol
PHSA	poly-12-hydroxystearic acid
PLD	path length difference
PMMA	poly(methyl methacrylate)
PY	Percus-Yevick
RCP	random close-packing
SAXS	Small-Angle X-ray Scattering
VFT	Vogel-Fulcher-Tammann
XPCS	X-ray Photon Correlation Spectroscopy

Symbols

B	brilliance
$\Delta\Omega$	observed solid angle
$\mathrm{d}\sigma/\mathrm{d}\Omega$	differential scattering cross-section
η_0	dynamic viscosity of the suspending liquid
$g_2(\vec{q},t)$	intensity correlation function
$H(q)$	hydrodynamic function
$I(\theta)$	Angle-dependent scattered intensity
$I(\theta,t)$	Angle- and time-dependent scattered intensity
$\vec{k_f}$	final (scattered) wavevector
$\vec{k_i}$	incident wavevector
λ	wavelength
Φ	volume fraction
$\vec{q}$	momentum transfer vector
q_m	momentum transfer vector value of the $S(q)$ peak
q	magnitude of $\vec{q}$
R	particle radius
r_0	classical electron radius
τ_B	Brownian relaxation time
τ_H	hydrodynamic interactions relaxation time
τ_R	structural relaxation time
2θ	scattering angle
ξ_L	longitudinal coherence length

ξ_T	transverse coherence length
Z	atomic number

Declaration of Authorship

I, Paweł Kwaśniewski, declare that this thesis titled, "Probing dynamics of hard sphere suspensions at high volume fractions with coherent X-rays" and the work presented in it are my own. I confirm that:

- This work was done wholly while in candidature for a research degree at this University.
- Where I have consulted the published work of others, this is always clearly attributed.
- Where I have quoted from the work of others, the source is always given. With the exception of such quotations, this thesis is entirely my own work.
- I have acknowledged all main sources of help.
- Where the thesis is based on work done by myself jointly with others, I have made clear exactly what was done by others and what I have contributed myself.

Signed: P. Kwaśniewski

Date: 26/06/2012

Acknowledgements

I would not be able to write this thesis without the help and support of many people during these three years. First of all, I would like to thank Anders Madsen and Andrei Fluerasu – my supervisors who gave me the opportunity to take up this Ph.D. project. They dedicated a significant amount of their time to guide me sharing their impressive knowledge and experience.

I sincerely thank Catherine Quilliet, the director of this thesis, for helping me organize my thoughts and providing stimulation to write.

I express my gratitude to the members of the jury: Judith Peters, Doru Constantin and Luigi Cristofilini, who kindly agreed to take this function and dedicated their time to carefully read and comment on this thesis.

I wish to thank Yuriy Chushkin and Chiara Caronna who developed the computer programs for data processing and analysis and shared them with me, providing explanations and comments whenever I needed them.

I would also like to thank Orsolya Czakkel and Beatrice Ruta for their support during beam times, helpful discussions and advices.

This work could not have been done without the colloidal particles, provided by Andrew Schofield from Edinburgh University, who also quickly and exhaustively answered all my colloid related questions.

I thank Ralf Schweins for committing his time to perform light scattering measurements of my samples. I am grateful to Narayanan Theyencheri, Michael Sztucki and Jeremie Gummel from ID02 for sharing their beam time, conducting SAXS measurements and helping with data analysis.

I also wish to acknowledge Jean-Baptiste Salmon and Jacques Leng from LOF--Bordeaux for their time and effort offered to introducing me into the subject of microfluidics.

I thank Abdellatif Moussaïd, who helped me a lot both in professional and private matters.

I would like to thank my father-, mother- and brother-in-law: Andrzej, Wanda and Grzegorz Woźniak, who helped and supported me and my family from the very beginning of this project. Without them it would be much more difficult for us to move and live in Grenoble.

I am deeply grateful to my parents, who always supported me and believed in me, making me the person I am now.

Finally, I would like to express my gratitude to the two women of my life: my wife Agata, for her love, understanding, courage and support, and my daughter Zuzia, whose bright smile overcomes all fatigue.

Résumé (français)

Les suspensions colloïdales de particules sphériques présentant des interactions de type sphères dures font partie des systèmes les plus simples et les plus largement étudiés en Matière Molle. Elles peuvent être considérées comme systèmes modèles pour tester des théories plus générales, par exemple en ce qui concerne la cristallisation [Pusey 1986] ou la transition vitreuse [Pusey 1987]. Malgré de nombreux résultats théoriques et expérientaux dans ce domaine, le comportement dynamique des suspensions de sphères dures n'a pas été complètement élucidé.

La spectroscopie à corrélation de photons X (XPCS) est une technique de diffusion cohérente équivalente à la Diffusion Quasi-Elastique de la Lumière (DQEL) [Martinez 2011], qui est un des principaux outils d'investigation de la dynamique colloïdale [Berne 2000]. Comparée à la lumière visible, l'utilisation de rayons X procure des renseignements sur les transferts de moment de plus haute énergie, et évite les diffusions multiples - phénomène qui complique sensiblement les études en DQEL pour les échantillons concentrés. De plus, l'utilisation du détecteur 2D compteur de photons (MAXIPIX) disponible sur la ligne ID10 (ESRF) donne des renseignements sur l'évolution de la dynamique de l'échantillon au cours de l'exposition, via les fonctions de corrélation à deux temps.

Dans ce travail, nous avons étudié une suspension de sphères colloïdales de PMMA (poly(méthylmétacrylate)) stériquement stabilisées. La distribution en taille des particules et leur concentration ont été obtenues par diffusion de rayons X aux petits angles (SAXS). Les expériences de XPCS effectuées aux plus grandes fractions volumiques en particules ($\Phi > 0.5$) mettent en évidence à la fois des temps de diffusion courts et des temps longs autour des pics de Bragg. Une comparaison avec une précédente étude [Orsi 2012b] montre, pour une petite gamme de fractions volumiques, une modification drastique de la loi d'échelle entre les temps de relaxation courts et les temps longs qui avait été initialement proposée par Segrè et Pusey [Segrè 1996]. L'analyse des fonctions de corrélation à deux temps révèle un comportement dynamique complexe des échantillons légèrement au-dessus de la transition vitreuse, alors qu'on n'observe aucun signe de modifications structurales via diffusion statique. Utiliser la XPCS sur des suspensions en écoulement dans des canaux cylindriques avait fait ses preuves pour renseigner à la fois sur les propriétés dynamiques et d'écoulement de suspensions diluées [Fluerasu 2010]. Ici, nous discutons les potentialités et les limites de cette méthode, en étudiant l'interaction entre les propriétés rhéologiques et dynamiques dans ces systèmes complexes modèles que sont les verres colloïdaux.

Abstract

Colloidal suspensions of spherical particles presenting hard-sphere like interactions is one of the simplest and most widely studied systems of soft condensed matter. They can be treated as a model for testing fundamental theories, regarding e.g. crystallization [Pusey 1986] or glass transition [Pusey 1987]. Despite the long history of both theoretical and experimental research, the dynamic behavior of hard sphere suspensions still lacks a complete understanding.

X-ray Photon Correlation Spectroscopy (XPCS) is a coherent scattering technique equivalent to Dynamic Light Scattering (DLS) [Martinez 2011], which is one of the main tools used in the study of colloidal dynamics [Berne 2000]. Comparing to visible light, the use of X-rays provides access to higher momentum transfer vector values and allows to avoid multiple scattering – a phenomena significantly complicating DLS measurements on concentrated samples. Moreover, the use of a fast, single photon counting area detector (MAXIPIX) available at the ID10 beamline at ESRF gives insight into the evolution of sample dynamics during the measurement time by the means of two-time correlation functions.

In this work suspensions of sterically stabilized poly(methyl methacrylate) (PMMA) colloidal spheres were used. Particle size, polydispersity and volume fractions of the samples were obtained using the Small-Angle X-ray Scattering (SAXS) technique. XPCS measurements at high volume fractions ($\Phi > 0.5$) show both short- and long-time diffusive behaviour for scattering vector values around, but not restricted to the structure factor peak position. A comparison with an earlier study [Orsi 2012b] shows a dramatic change in the approximate scaling between the short- and long-time relaxation rates, initially proposed by Segrè and Pusey in [Segrè 1996], over a small range of volume fractions. The analysis of two-time correlation functions reveals complex dynamic behaviour of a sample slightly above the glass transition, while no signs of structural changes are observed in the static scattering patterns. The studies indicate the dynamics being governed by a jamming transition driven by restrictions in free volume rather than a glass transition as know from the mode-coupling theory. A combination of XPCS with flow in a cylindrical channel has demonstrated previously to give both dynamic and flow properties of dilute suspensions [Fluerasu 2010]. Here we discuss the potential and limitations of this method in the study of the interplay between rheological properties and dynamics in complex systems such as colloidal glasses.

Introduction (français)

"Suspension colloïdale" est un terme qui peut s'appliquer à une large gamme de substances. Les colloïdes sont très présents dans la vie de tous les jours, d'autant plus que beaucoup de constituants du vivant eux-même sont de nature colloïdale, comme les suspensions de protéines ou de polysaccharides, ou le sang. On rencontre facilement dans les applications industrielles des dispersions d'une phase dans une autre, les plus courantes étant par exemple le ciment, le papier, certaines encres et les peintures. La science des colloïdes concerne une large variété de matériaux et de propriétés, ce qui en fait un domaine de recherches multidisciplinaire, aux confins de la physique, de la chimie, et du génie chimique.

Outre leur importance pratique, les colloïdes présentent un intérêt en tant que système modèle pour l'échelle atomique: une suspension de particules quasi-identiques peut être décrite à l'aide des outils et théories statistiques développés pour les états liquides et solides simples [Pusey 1991]. Il a été montré qu'une collection de particules de type sphères dures peut présenter des transitions de phase, comme la cristallisation ou la transition vitreuse [Pusey 1986, Pusey 1987], les particules jouant le rle des atomes. Etant d'une taille typiquement de trois ordres de grandeur au-dessus des atomes, les colloïdes sont considérablement ralentis. Ceci rend la dynamique des colloïdes beaucoup plus accessible expérimentalement.

Il peut sembler surprenant que le comportement dynamique d'un système composé de sphères dures dans un liquide ne soit pas encore complètement compris, malgré un long passé de recherche théorique et expérimentale. Plusieurs aspects des colloïdes contribuent à cet état de fait. Tout d'abord, les particules colloïdales sont généralement polydisperses en taille, surtout celles d'origine synthétique. Ceci joue sur les comportements à la fois dynamique et structural du système. Ensuite, il peut y avoir plusieurs types d'interactions entre les particules, et leur résultante peut être lourdement influencée par leur environnement. Enfin, le liquide qui suspend les particules transmet quasi-instantanément les interactions hydrodynamiques, rendant encore plus complexe la description du comportement des particules.

Une des gageures de la science des colloïdes concerne la dynamique aux temps longs des suspensions concentrées. Ce sujet a été défriché par les travaux expérimentaux pionniers de Pusey, van Megen et collaborateurs en Diffusion Quasi-Elastique de la Lumière (DQEL) (par ex. [Pusey 1986, Pusey 1987, van Megen 1991, van Megen 1994]). Des procédures de préparation d'échantillons non triviales et des techniques de diffusion complexes ont été développées pour diminuer la diffusion multiple au sein des phases denses de colloïdes, comme la Diffusion de Lumière Dynamique à Deux Couleurs (TCDLS) [Segrè 1995c]. Une étude utilisant la TCDLS, rapportée dans [Segrè 1996], montre un comportement proche

d'une loi d'échelle pour les fonctions de diffusion intermédiaires d'une population de particules stériquement stabilisées, qui se réduisent à une courbe matresse quand elles sont divisées par le coefficient de diffusion aux temps courts $D_S(q)$. Ceci indique une proportionnalité simple, indépendante de q, entre $D_S(q)$ qui décrit la diffusion d'une particule dans une cage formée par les voisins à haute fraction volumique, et le coefficient de diffusion aux temps longs $D_L(q)$, associé au temps de vie des cages. Une explication semi-quantitative de cette loi d'échelle a été proposé dans la théorie idéalisée du couplage de modes de [Fuchs 1999], avec la remarque qu'elle pourrait ne pas être valide dans des systèmes autres que les suspensions de sphères dures stériquement stabilisées. De fait, une étude expérimentale effectuée par la suite sur une suspension stabilisée par des charges de surface [Lurio 2000] et qui utilise l'équivalent X de la DQEL, à savoir la spectroscopie de correlation de photons X (XPCS), n'a pas montré ce type de loi d'échelle. De manière surprenante, une étude plus récente effectuée elle aussi en DQEL sur des systèmes stabilisés par des charges a clairement montré des données qui suivent le même comportement que celui décrit par Segrè et Pusey [Holmqvist 2010]. Il est peu probable que la différence provienne des deux techniques utilisées, puisqu'une comparaison détaillée entre XPCS et DQEL a montré que les deux méthodes donnent des résultats équivalents [Martinez 2011]. Dans le même papier, les auteurs montrent qu'ils pouvaient définir sans ambigité un régime de diffusion aux temps longs, du type de celui utilisé dans [Segrè 1996], uniquement autour du pic du facteur de structure, dans une suspension de particules stériquement stabilisées. Le comportement de $D_S(q)/D_L(q)$ n'a donc pas pu être testée.

Le but de cette thèse est de clarifier le comportement de suspensions concentrées de sphères dures aux temps longs. Les échantillons étudiés contiennent des particules stériquement stabilisées de poly(méthyl méthacrylate) (PMMA) suspendues dans de la décaline - un système semblable à celui utilisé par Segrè et Pusey dan [Segrè 1996]. La gamme de fractions volumiques testées atteint la fraction volumique critique de transition vers le verre colloïdal ($\Phi \approx 0.58$). La dynamique des particules a été étudiée en XPCS, ce qui évite la diffusion multiple et les techniques de préparation d'échantillons délicates. Un soin particulier a été apporté pour éviter l'endommagement des échantillons par le rayonnement pendant les mesures. Les fonctions de corrélation mesurées à proximité du pic de $S(q)$ montrent une relaxation caractéristique en deux temps, avec deux régions clairement identifiées (temps courts et temps longs). Le coefficient de diffusion aux temps courts dépendant de q, obtenu par ajustement des fonctions de diffusion intermédiaires, s'avère suivre les oscillations de $S(q)$ ainsi que prédit et observé précédemment. Les fonctions de diffusion intermédiaires normalisées par $D_S(q)$ se rassemblent sur une courbe unique jusqu'au début de la région diffusive aux temps longs, identifiée pour les q proches du pic de $S(q)$. L'utilisation d'un détecteur 2D autorise le calcul des fonctions de corrélation à deux temps. Elles sont discutées pour l'échantillon le plus concentré que nous ayions étudié, près de la transition vitreuse, où un comportement hors d'équilibre complexe est observé. De plus, une étude de XPCS sous écoulement a été publiée, où le traitement des résultats fournit à la fois des

informations dynamiques et des informations liées à l'écoulement [Fluerasu 2010]. Des expériences préliminaires dans des conditions d'écoulement semblables ont été également effectuées sur des échantillons concentrés. La possibilité d'en faire une étude quantitative est discutée dans ce travail.

La thèse est organisée comme suit:

- Le premier chapitre présente la technique de diffusion de rayons X aux petits angles (SAXS), qui a été utilisée pour obtenir des informations structurales sur les échantillons étudiés. Les principes de base de la diffusion X sont discutés, suivis par une description plus détaillée des modèles pertinents pour ce travail.
- La technique principalement utilisée dans cette étude, la spectroscopie de corrélation de photons X (XPCS), est présentée dans le deuxième chapitre. Les propriétés de cohérence du rayonnement X du synchrotron y sont discutées, en introduction au paragraphe traitant de la diffusion cohérente des matériaux désordonnés. On y trouve une description des quantités mesurées et de leur signification physique. Le chapitre se clôt sur une vue d'ensemble d'un dispositif expérimental typique.
- Le troisième chapitre introduit l'essence de la physique des systèmes colloïdaux, en insistant sur les supensions de sphères dures qui sont étudiées dans cette thèse. Les méthodes permettant d'éviter l'agglomération des particules sont présentées ainsi que le diagramme de phase général des suspensions de sphères dures. Le type de suspensions utilisé dans cette étude est détaillé (propriétés, synthèse). La fin du chapitre comporte un rappel de l'état de l'art en ce qui concerne la dynamique des suspensions cocnentrées de sphères dures.
- Le chapitre 4 présente les résultats de XPCS sur suspensions colloïdales diluées en écoulement. Ces résultats ont été publiés dans [Fluerasu 2010]. L'influence du cisaillement sur la dynamique des particules, suivie par XPCS, y est discutée, suivie par une description du dispositif expérimental dédié. Les résultats présentés montrent que la XPCS peut être utilisée pour mesurer à la fois la réponse advective au cisaillement appliqué, et la dynamique diffusive d'une suspension colloïdale en écoulement continu.
- Le cinquième chapitre discute le résultats de mesures dynamiques sur colloïdes concentrés. Tout d'abord, le point est fait sur les recherches concernant le comportement en loi d'échelle de la fonction de diffusion intermédiaire, qui est l'un des sujets principaux de cette thèse. Cette mise au point est suivie par une description des procédures d'acquisition et de traitement de données. Ensuite, les résultats expérimentaux sont présentés, qui étendent les études précédemment évoquées au domaine des fractions volumiques proches de la transition vitreuse. Le comportement hors d'équilibre de l'échantillon le plus concentré, observé en correlation à deux temps, est discuté.
- Le dernier chapitre de la thèse présente des résultats préliminaires de mesures de suspensions concentrées en écoulement, suivis par une discussion sur la possibilité d'utiliser le type d'analyse exposé au chapitre 4 pour des colloïdes

dilués sans interactions. Il se termine avec un rappel général des résultats, et des commentaires sur les perspectives de continuation du sujet.

Introduction

Colloidal suspension is a very broad term, which can be attributed to an extremely wide range of substances. Colloids are ubiquitous in every-day life, including the fact that many components of "life" itself have colloidal nature, like protein and polysaccharide solutions or blood. Dispersions of one phase in another are common in industrial applications, with cement, paper, inks and paints as just a few examples. This large variety of materials and properties makes colloid science a multidisciplinary discipline, spanning physics, chemistry and chemical engineering.

Beside of their practical importance, the interest in studying colloids lies in their ability to serve as models of atomic systems. A suspension of (nearly) identical particles can be described using tools from statistical mechanics and theories developed for simple liquid and solid states [Pusey 1991]. An assembly of hard-sphere like particles has been shown to present phase transitions, like crystallization and glass transition [Pusey 1986, Pusey 1987], as known from atomic and molecular systems. Being typically more than three orders of magnitude larger than atoms, colloids move significantly slower. This makes colloidal dynamics much more accessible for studies.

It may seem surprising that the dynamic behaviour of a system composed of hard spheres suspended in a liquid still lacks complete understanding, despite a long history of theoretical and experimental research. Several aspects of colloids contribute to this state. Firstly, colloidal particles, especially those of synthetic origin, are usually polydisperse in size. This influences both the dynamic and structural behaviour of the system. Secondly, various types of interaction can be present between the particles, often heavily influenced by their environment. Thirdly, the suspending liquid is a mediator of quasi-instantaneous *hydrodynamic interactions*, making the description of particle behaviour even more complex.

One of the challenging issues in colloid science is the long-time dynamics of concentrated suspensions. Experimental studies of this subject were pioneered by Pusey, van Megen and collaborators (e.g. [Pusey 1986, Pusey 1987, van Megen 1991, van Megen 1994]) using Dynamic Light Scattering. To decrease the amount of multiple scattering present in dense colloids, elaborate sample preparation procedures or complex scattering techniques, like Two-Color DLS (TCDLS) [Segrè 1995c] have been developed. In a study reported in [Segrè 1996] using TCDLS the authors observed an approximate scaling behaviour of the measured intermediate scattering functions of an assembly of sterically stabilized particles, which collapsed onto a single master curve when divided by the short-time diffusion coefficient $D_S(q)$. This indicates a simple, q independent proportionality between $D_S(q)$, describing particle diffusion in a cage of neighbours formed at high packing

fraction, and the long-time diffusion coefficient $D_L(q)$, associated with the breakdown of the cages. A semi-quantitative explanation of the scaling has been proposed within the idealized mode-coupling theory in [Fuchs 1999], with a remark that it may not be valid in systems other than sterically stabilized hard spheres. In fact, an experiment performed later on a *charge* stabilized suspension [Lurio 2000], using the X-ray equivalent of DLS – X-ray Photon Correlation Spectroscopy (XPCS), showed no such scaling in this system. Surprisingly, a more recent study of a charge stabilized system using DLS, published in [Holmqvist 2010] clearly shows data following the same behaviour as found by Segrè and Pusey. It is unlikely that the difference comes from the different techniques used, since a detailed comparison of XPCS and DLS, published in [Martinez 2011] shows that the two methods give equivalent results. In the same paper the authors show that they were unable to unambiguously define a long-time diffusive regime away from the structure factor peak in a suspension of sterically stabilized particles, similar to the one used in [Segrè 1996]. Consequently, the q behaviour of $D_S(q)/D_L(q)$ ratio could not be tested.

The aim of this thesis is to clarify the subject of long-time behaviour of hard sphere colloids at high volume fractions. The samples are sterically stabilized poly(methyl methacrylate) (PMMA) particles suspended in decalin – a system similar to the one studied by Segrè and Pusey in [Segrè 1996]. The range of volume fractions probed reaches the colloidal glass transition ($\Phi \approx 0.58$). Particle dynamics was probed using XPCS, avoiding multiple scattering and difficult sample preparation techniques, e.g. index matching. Much care was taken to avoid radiation damage during the measurements. The measured correlation functions show the characteristic two-step decay, with clearly identified short-and long-time diffusive regions in the vicinity of the $S(q)$ peak. The q dependent short-time diffusion coefficient extracted from fits of the intermediate scattering functions is found to follow the oscillations of $S(q)$, as predicted and observed before. Intermediate scattering functions scaled by $D_S(q)$ collapse on a single curve up to the time which marks the beginning of the long-time diffusive region identified for q close to the $S(q)$ peak. The use of a fast 2D detector allows for calculations of two-time correlation functions that can be used to study non-equilibrium dynamics. They are discussed for the sample at highest volume fraction probed, near the glass transition, where complex non-equilibrium behaviour is observed. The results support a picture where less free volume at high concentrations leads to kinetic arrest rather than a glass transition as in the mode-coupling description.

Additionally, results of XPCS measurements under flow of dilute colloidal suspensions are reported, which allowed to extract flow-related and dynamic information at the same time [Fluerasu 2010]. Preliminary measurements in similar conditions were also performed with concentrated samples. The possibility of their quantitative analysis is discussed in this work.

The thesis is organized as follows:

– The first chapter introduces the Small-Angle X-ray Scattering (SAXS) technique, which has been used to gain structural information about the samples

investigated. Basic principles of X-ray scattering are discussed, followed by a more detailed description of models relevant for this work.

– The main technique used in this study, X-ray Photon Correlation Spectroscopy (XPCS) is described in the second chapter. Coherent properties of synchrotron X-rays are discussed as an introduction to the subject of coherent scattering from disordered materials. An explanation of the measured quantities and their physical meaning is given. The chapter ends with an overview of a typical experimental setup.
– The third chapter gives a basic introduction to the physics of colloidal systems, focusing on hard-sphere suspensions, which are studied in this thesis. The methods of preventing particle agglomeration are discussed, followed by the phase diagram of a hard-sphere suspension. Next, the samples used in this study are described with their basic properties and preparation procedures. An overview of the current knowledge concerning dynamics of concentrated hard-sphere suspensions is given at the end of this chapter.
– Chapter four presents the results of XPCS measurements performed under flow on a *dilute colloidal suspension*. These results were published in [Fluerasu 2010]. The influence of shear flow on particle dynamics measured with XPCS is discussed, followed by a description of the specific experimental setup. The presented results show that XPCS can be used to measure both the advective response to applied shear and the diffusive dynamics of a dilute colloidal suspension under continuous flow.
– The fifth chapter discusses the results of dynamics measurements on *colloids at high volume fractions*. First, a summary is given on the dynamics of hard-sphere suspensions at high volume fractions. The review is followed by a description of the data acquisition and processing procedures. Next, experimental results are presented, which extend the previously reported studies to volume fractions near the colloidal glass transition. The non-equilibrium behaviour of the sample at highest Φ analysed, observed in the two-time correlation functions is discussed.
– The final chapter of this thesis presents preliminary results of measurements of the concentrated suspensions under flow, followed by a discussion of the possibility of applying a similar kind of analysis as the one reported in chapter 4 for dilute, non-interacting colloids. It ends with a general view of the results and comments on the perspectives of the subject continuation.

Résumé du Chapitre 1

Ce chapitre comporte une introduction à la technique de diffusion de rayons X aux petits angles (SAXS). Les principes théoriques du rayonnement sont présentés dans le contexte du rayonnement X synchrotron. L'intensité diffusée par une suspension colloïdale est calculée, tout d'abord en considérant la diffusion d'une particule unique (facteur de forme), puis en introduisant le terme qui rend compte des interactions interparticulaires dans une suspension concentrée (facteur de structure). Le facteur de structure est calculé en utilisant l'approximation courante de Percus-Yevick pour la fonction de corrélation directe. Les effets de la polydispersité en taille sont discutés. Pour une suspension de référence de sphères dures polydisperses dont les rayons présentent une distribution de Schultz, une solution analytique exacte est donnée. La fin du chapitre présente une comparaison, pour l'intensité diffusée, entre la solution analytique et la factorisation couramment pratiquée en un produit de facteurs de structure et de forme.

Chapter 1

Small-Angle X-ray Scattering

Contents

1.1 Introduction

This chapter introduces the Small-Angle X-ray Scattering (SAXS) technique performed with X-rays produced in a synchrotron facility – the European Synchrotron Radiation Facility (ESRF) in Grenoble, France. The term *synchrotron radiation*, originating from a specific type of particle accelerator, is currently used more generally to describe electromagnetic radiation produced by charged particles moving at relativistic velocities in magnetic fields. The Lorentz force acting on the particles along the direction perpendicular to their instantaneous velocities makes them travel along curved paths. Radiation emission is a consequence of the *radial* acceleration experienced by the charge, as opposed to *bremsstrahlung*, emitted by electrons encountering *linear* deceleration when impinging on a metal anode in an X-ray tube.

In a III generation synchrotron light source, like the ESRF, electrons are kept circulating in a closed orbit in a *storage ring* (see figure 1.1). Three types of devices are used to produce X-rays: *bending magnets*, inserted into the path of charged particles, keep them circulating, at the same time being a source of a broad spectrum of intense electromagnetic radiation. *Wigglers* and *undulators* are situated in straight sections. They are composed of magnetic arrays producing alternating forces making the particles oscillate, emitting radiation at each turn. A *III generation* synchrotron facility is mainly based on insertion devices (wigglers and undulators).

Irradiation of an inhomogeneous medium will cause scattering by the *fluctuations*. This statement is generally valid, independent of the type of radiation. The difference appears when the details of the interaction with the scattering medium are considered. Visible light is scattered due to differences in the index of refraction, while in case of X-rays it is due to *electron density* fluctuations. Neutrons scatter on atomic nuclei.

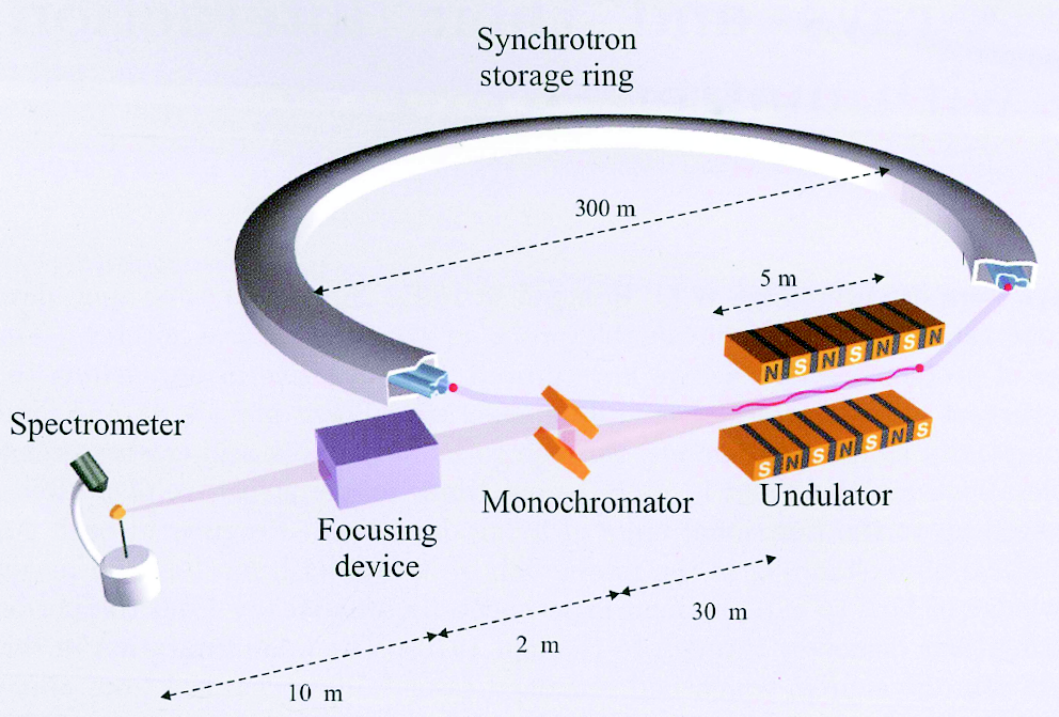

Figure 1.1: A sketch of a typical X-ray beamline at a III generation syncrhotron source. Radiation is produced by bunches of charged particles (electrons or positrons) which circulate in a storage ring. The ring is composed of straight sections with undulators or wigglers, forcing the particles to follow an oscillatory path along their average trajectory. The intense radiation produced is then formed by a number of optical elements, such as a monochromator, focusing device, etc., in order to fulfill the experimental requirements. Reproduced from [Als-Nielsen 2011].

Figure 1.2 shows a schematic representation of a scattering experiment. Some of the radiation impinging on a sample passes through unaffected, some is scattered. A detector can be used to measure the intensity of the scattered radiation at a certain angle 2θ. In principle, the scattering geometry allows to perform three types of experiments [Pusey 2002]: (i) measurement of angular dependence of the average scattered intensity $I(\theta)$, called *static* scattering, yielding structural information, (ii) if the incident radiation is coherent, the analysis of time and angular dependence of fluctuations in the scattered radiation $I(\theta, t)$ is possible (instead of time dependence, the frequency or energy changes can be measured) – this is *dynamic* (quasi-elastic or inelastic) scattering, yielding dynamic information, (iii) provided that the equipment is well calibrated, a measurement of the time (frequency) averaged absolute magnitude of the scattered intensity will give information on the mass or molecular weight of the scatterers.

In this work the first two methods are applied to investigate a disordered, soft matter system. This chapter presents the basic principles of static scattering applied to X-rays – the SAXS, used to gain structural information about the samples. An

introduction to X-ray Photon Correlation Spectroscopy (XPCS), exploiting quasi-elastic scattering of coherent radiation to study sample dynamics, will be given in the following chapter.

1.2 Small-Angle X-ray Scattering

As already mentioned in the introduction, the derivation of basic scattering theory is independent of the type of scattered radiation. Here it is presented in the context of synchrotron X-rays.

1.2.1 Basic principles

A schematic layout of a SAXS experiment is presented in figure 1.2. The highly collimated, monochromatic X-ray beam impinges on a sample. The scattered intensity is recorded using a two dimensional detector, which is guarded from the transmitted beam by a beamstop placed just in front of it. Looking at the geometry of the incident and scattered wavevectors $\vec{k_i}$ and $\vec{k_f}$ (Figure 1.3), the momentum transfer or scattering vector $\vec{q}$ can be defined as $\vec{q} = \vec{k_i} - \vec{k_f}$. Its magnitude is related to the scattering angle 2θ by:

$$q = |\vec{q}| = \frac{4\pi}{\lambda} \sin(\theta), \tag{1.1}$$

where λ is the X-ray wavelength. Having a unit of reciprocal length, q indicates the length scales probed by the scattering experiments. Typical values covered in a synchrotron SAXS experiment are between $0.006 < q < 6\ nm^{-1}$ [Narayanan 2008]. Wavevector magnitude is related to wavelength as $|\vec{k}| = 2\pi/\lambda$. Knowing this the given q range can be translated into real space dimensions between 1 μm and 1 nm.

The usual approach deriving a formula describing the scattered intensity begins with a consideration of single electron scattering. A detailed derivation can be found e.g. in [Glatter 1982, Als-Nielsen 2011]. The fundamental quantity measured in a scattering experiment is the *differential scattering cross section* $\mathrm{d}\sigma/\mathrm{d}\Omega$. It is defined as the ratio between the scattered intensity I_{sc} (number of photons registered by the detector per second) to the incident beam flux ϕ_0 (number of photons passing through unit area per second) and the observed solid angle $\Delta\Omega$. It can be expressed in terms of the Thomson scattering length, equal to the classical electron radius r_0:

$$\left(\frac{\mathrm{d}\sigma}{\mathrm{d}\Omega}\right) = \frac{I_{sc}}{\phi_0 \Delta\Omega} = r_0^2 P, \tag{1.2}$$

where r_0 is:

$$r_0 = \frac{e^2}{4\pi\varepsilon_0 mc^2} = 2.82 \times 10^{-5}\ \mathring{A} \tag{1.3}$$

and P is the polarization factor, which depends on the X-ray source. Radiation coming from a synchrotron insertion device is linearly polarized in the horizontal

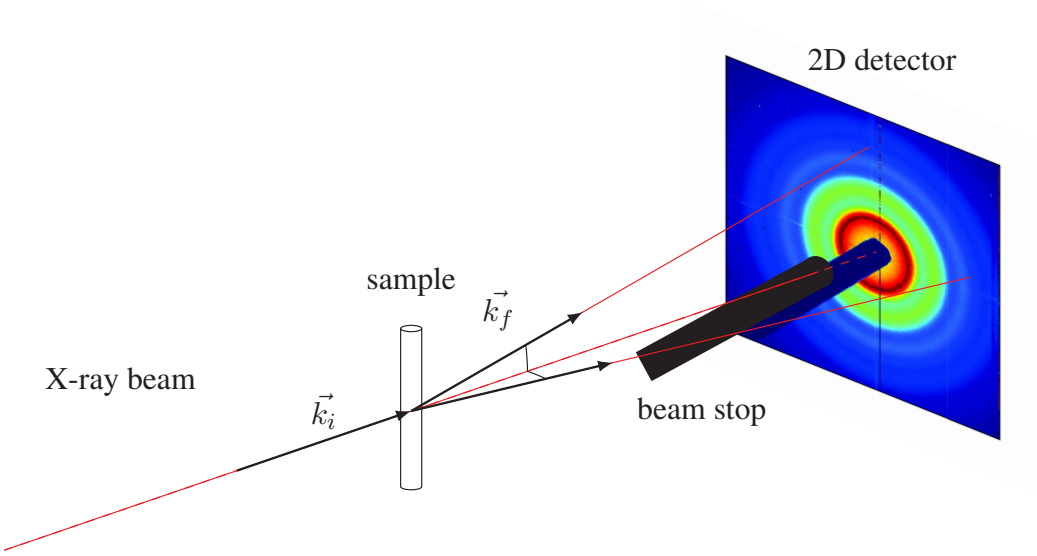

Figure 1.2: Schematic layout of a SAXS experimental setup, showing the incident, scattered and transmitted X-ray beams, beamstop and a 2D detector with an isotropic scattering pattern.

plane and elliptically polarized out of this plane [Als-Nielsen 2011]. The polarization factor for different scattering planes is equal to:

$$P = \begin{cases} 1 & \text{vertical scattering plane} \\ \cos^2\theta & \text{horizontal scattering plane} \end{cases} \tag{1.4}$$

Consequently, the scattered intensity at $\theta = 90^\circ$ vanishes in the horizontal plane. In the small angle limit (typically $\theta < 5^\circ$) the influence of polarization can be neglected, assuming $P \approx 1$.

The classical derivation of equation 1.2 is based on relating the incident and scattered intensities to the values of the corresponding electric fields. The electron is then treated as a source of a spherical wave, for which the electric field can be evaluated from Maxwell's equations [Jackson 1998, Als-Nielsen 2011]. It should be noted that the resulting differential cross section, as well as the total cross section found by integrating $\mathrm{d}\sigma/\mathrm{d}\Omega$ over all possible scattering angles, is a constant, independent of energy. This is not valid at low photon energies (visible light) and near the so called absorption edges – energies which correspond to electron transition or ionization potentials.

Proceeding to X-ray scattering from an atom with Z electrons, whose distribution can be described by a number density $\rho(\vec{r})$, the scattered radiation is a superposition of contributions from all volume elements of the charge distribution. The total scattering length of an atom is:

$$-r_0 f^0(\vec{q}) = -r_0 \int \rho(\vec{r}) \exp\left(i\vec{q}\cdot\vec{r}\right)\mathrm{d}\vec{r}, \tag{1.5}$$

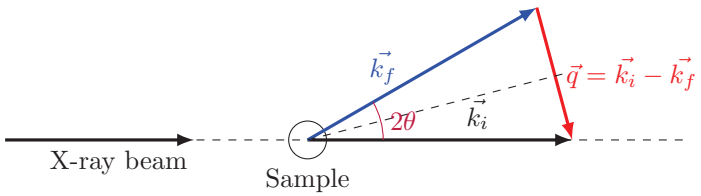

Figure 1.3: Definition of the momentum transfer (scattering) vector $\vec{q}$.

where $f^0(\vec{q})$ is the atomic form factor, which in the limit of $\vec{q} \to 0$ takes the maximum value $f^0(\vec{q} = 0) = Z$. With $\vec{q} \to \infty$ and the different volume elements scattering out of phase the form factor $f^0(\vec{q} \to \infty) = 0$.

Considering higher complexity level – molecules, adequate form factors can be defined by summing the $f^0(\vec{q})$ of individual atoms.

In a real experiment, the incident radiation is not only scattered, but also absorbed by the sample. This can be taken into account by giving the absorption coefficient μ, relating the intensity I_T transmitted through a sample of thickness l_s to the initial value I_0:

$$I_T = I_0 \exp[\mu l_s]. \tag{1.6}$$

The intensity scattered at small angles also depends on the sample thickness [Glatter 1982]:

$$I_{sc} \propto l_s \exp[-\mu l_s]. \tag{1.7}$$

This expression has a maximum at $l_{max} = 1/\mu$, which defines the optimal sample thickness – the compromise between absorption and scattering. The value of transmission $T = I_T/I_0$ at l_{max} can be calculated from equation 1.6: $T = 1/e$.

Including absorption and the detector efficiency ε, the experimental scattered intensity can be expressed as [Lindner 2002]:

$$I_{sc} = I_0 \varepsilon T \Delta\Omega A_s l_s \frac{\mathrm{d}\Sigma}{\mathrm{d}\Omega}, \tag{1.8}$$

with A_s being the cross section of the beam and $\mathrm{d}\Sigma/\mathrm{d}\Omega$ - the differential scattering cross section per unit volume: $\mathrm{d}\Sigma/\mathrm{d}\Omega = 1/V\,\mathrm{d}\sigma/\mathrm{d}\Omega$. Since the value which contains structural information is the differential scattering cross section, an essential step of quantitative SAXS analysis is the normalization of the measured intensities to $\mathrm{d}\Sigma/\mathrm{d}\Omega$, which will from now on be denoted by $I(q)$ with units of reciprocal length [Narayanan 2008].

1.2.2 Discrete scatterers – form and structure factor

After the general introduction a more specific case of discrete scattering objects suspended in a liquid will now be discussed. These objects, referred to as “particles”,

consist of many molecules, and may correspond to polymer molecules, micelles, colloidal particles, etc.

Starting with the simplest case – a dilute suspension of N identical particles per unit volume, the inter-particle interactions can be neglected, leading to a simple expression for the scattered intensity, which depends mainly on the shape and size of an individual scatterer [Narayanan 2008]

$$I(\vec{q}) = N|F(\vec{q})|^2, \tag{1.9}$$

where $F(q)$ is the single particle form factor, which can be defined by analogy to the atomic form factor (equation 1.5), as a *coherent* sum of scattering amplitudes of individual scattering centres building the particle. It can be derived from the electron density distribution by calculating its Fourier transform. Here coherent implies preserving the phase relationship between different scattered waves and summation of their amplitudes. Assuming a continuous electron density distribution, the $F(q)$ can be expressed as an integral over the particle volume V [Narayanan 2008]:

$$F(\vec{q}) = \int_V \Delta\rho(\vec{r}) \exp\left[i\vec{q}\vec{r}\right] \mathrm{d}V, \tag{1.10}$$

where $\Delta\rho(\vec{r}) = \rho(\vec{r}) - \rho_s$ is the relative scattering length density – the difference between the value for the sample ($\rho(\vec{r})$) and the suspending liquid (ρ_s). For uniform electron density $\rho(\vec{r})$ becomes independent of $\vec{r}$ and is given by:

$$\rho = \frac{n_e d_M N_A}{M_W} r_0 \tag{1.11}$$

with n_e being the number of electrons in a molecule, d_M – mass density, N_A – the Avogadro number and M_W – molar mass.

In some cases the integral in equation 1.10 can be evaluated analytically, in others – numerically. A collection of form factors for particles of different shapes can be found for instance in [Pedersen 1997] and references therein. Here only the simplest example of a homogeneous sphere of radius R is given:

$$F(q) = \frac{3}{(qR)^3} \left[\sin(qR) - qR\cos(qR)\right]. \tag{1.12}$$

In the derivation of equation 1.12 the $\Delta\rho(\vec{r})$ is replaced by a constant value of the density difference between the particle and the suspending medium. Because of the spherical symmetry of the discussed system only the magnitude of the scattering vector $|\vec{q}|$ needs to be taken into account, which for brevity will from now on be denoted as q.

Equation 1.12 assumes that all particles are identical. In real systems this is most often not true – the scatterers are polydispersed. Instead of just the particle radius, a normalized distribution function $D(R)$ ($\int_0^\infty D(R)\mathrm{d}R = 1$) is needed to describe the size. This complicates the expression for scattered intensity:

$$I(q) = N\Delta\rho^2 \int_0^\infty D(R)V^2(R)|F(q,R)|^2 \mathrm{d}R. \tag{1.13}$$

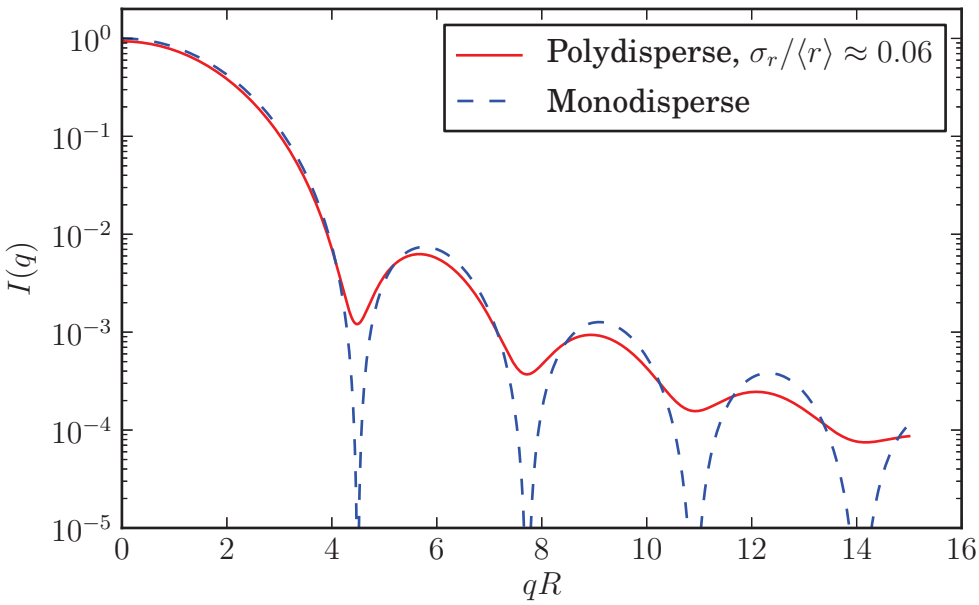

Figure 1.4: The influence of particle radius polydispersity on the form factor of spheres. The dashed blue line is a plot of equation 1.12. The solid red line presents a polydisperse sphere function derived from equation 1.13 assuming Schulz radius distribution.

Here $V(R)$ is the particle volume and the integration is performed over all possible particle radii R. For spherical particles an analytical expression can be derived for different distributions, such as Gaussian, Schulz or rectangular [Aragon 1976, Kotlarchyk 1983]. The effect of polydispersity is demonstrated in figure 1.4 on the example of spherical particles with a Schulz size distribution, expressed as:

$$f(r) = \left(\frac{Z+1}{\langle r\rangle}\right)^{Z+1} r^Z \exp\left[-\left(\frac{Z+1}{\langle r\rangle}\right) r\right] / \Gamma(Z+1),\ Z > -1, \tag{1.14}$$

with the particle radius root mean square deviation from the mean $\langle r\rangle$ given by:

$$\sigma_r = \frac{\langle r\rangle}{\sqrt{Z+1}}. \tag{1.15}$$

In the above equations Z is the Schulz "width factor", which has been set to $Z = 300$ for the calculation of the red curve presented in figure 1.4. An example of the Schulz distribution function for different values of Z (1, 10, 50 and 100) is plotted in figure 1.5.

In order to extend the theory to concentrated systems of particles, an additional term – the structure factor $S(q)$ needs to be introduced to account for inter-particle interactions. In general, $S(q)$ is a function of the interaction potential and N. In the limit of dilute, non-interacting particles, $S(q) \approx 1$. If the scatterers are spherically

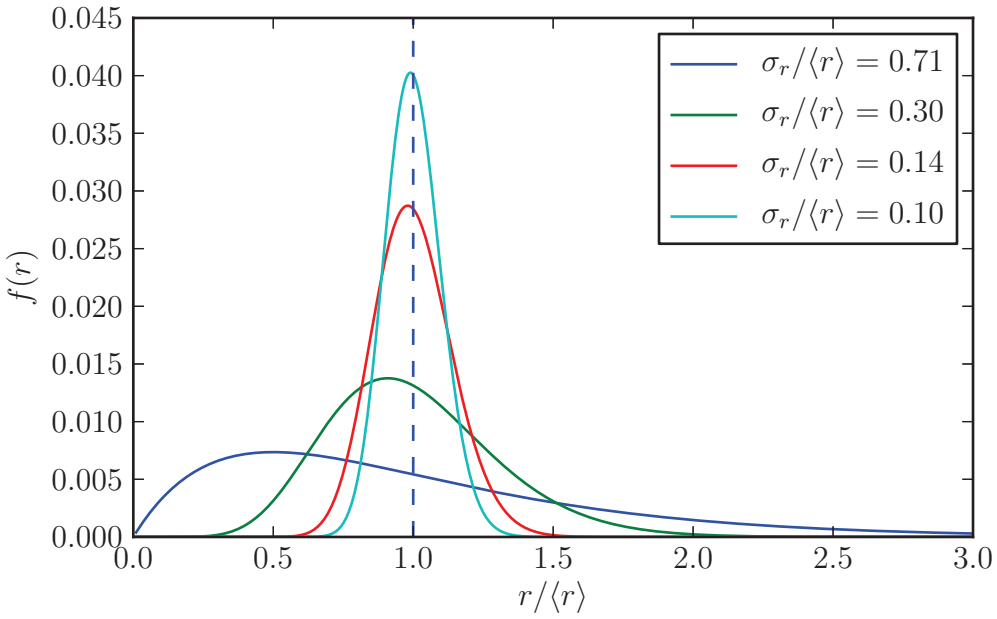

Figure 1.5: A plot of the Schulz distribution function (equation 1.14) for different values of Z parameter.

symmetric and the size distribution is narrow, $I(q)$ can be factorized to the form [Pedersen 1997, Als-Nielsen 2011]

$$I(q) = NV^2\Delta\rho^2 P(q)S(q), \tag{1.16}$$

where $P(q) = |F(q)|^2$. The $S(q)$ can be related to a function defined in direct space – the radial distribution function $g(r)$ (also called the pair correlation function), which gives a statistical description of the structure of a disordered system [Klein 1996]:

$$S(q) = 1 + 4\pi N \int_0^\infty (g(r) - 1)\frac{\sin(qr)}{qr} r^2 \mathrm{d}r \tag{1.17}$$

More exactly, $g(r)$ is related to the probability of finding a particle at a distance r from the centre of a given particle. The first term in brackets in the integral of equation 1.17 is the so called total correlation function $h(r) \equiv g(r) - 1$. In a many-body system the $h(r)$ is given in terms of the *a priori* unknown direct, two--particle correlation function $c(r)$ and multiple indirect correlations. The indirect part describes the contributions of chains of direct correlations starting from one of the particles of the pair and ending at the other. This leads to the Ornstein-Zernike (OZ) equation [Klein 1996]:

$$h(r) = c(r) + n \int c(|\vec{r} - \vec{r}\,'|)h(\vec{r}\,')\,\mathrm{d}\vec{r}\,' \tag{1.18}$$

In order to use the OZ equation to calculate $h(r)$, and from this the structure factor, an assumption needs to be made about the form of $c(r)$. This is the so-called *closure relation*, which introduces approximations. Several closure relations have been developed. A more detailed overview is given e.g. in [Klein 2002]. One commonly used is the Percus-Yevick (PY) approximation, given by [Narayanan 2008]:

$$c(r) = g(r)\left(1 - \exp\left[-\frac{U(r)}{k_B T}\right]\right) \tag{1.19}$$

It allows to obtain an analytical solution of the OZ equation and works well for short-range potentials $U(r)$, such as the hard-sphere interaction [Klein 1996, Chen 2002] used in this thesis.

Knowing the form of $c(r)$ allows to calculate its Fourier transform to obtain $c(q)$ and calculate the $S(q)$ in the monodisperse case from:

$$S(q) = \frac{1}{1 - Nc(q)} \tag{1.20}$$

It is more complicated to obtain the structure factor of polydisperse particles. The separation of $P(q)$ and $S(q)$, as in equation 1.16, is no longer possible. The expression for the scattering intensity for a system containing a continuous distribution of particles with radii r_i can be given in terms of their scattering amplitudes F_i and partial structure factors S_{ij} [Griffith 1987]:

$$I(q) = N\int_0^\infty F_i^2(q) f(r_i)\mathrm{d}r_i + N\int_0^\infty\int_0^\infty F_i(q)F_j(q)S_{ij}(q)f(r_i)f(r_j)\mathrm{d}r_i\mathrm{d}r_j \tag{1.21}$$

Here $f(r_i)$ and $f(r_j)$ are the distribution functions of particles i and j.

The integrals in equation 1.21 can be solved analytically by taking the scattering amplitude of a uniform sphere (equation 1.12) and $S_{ij}(q)$, as derived in [Blum 1979] within the Percus-Yevick approximation. Detailed derivation and the complete expression is presented in [Griffith 1987], and omitted here for the sake of brevity. In this approach the static structure factor of a polydisperse system can be obtained by setting $F_i(q) = F_j(q) = 1$ in equation 1.21. Solving just the first integral in equation 1.21 gives the expression for the polydisperse form factor, equivalent to the one published previously in [Aragon 1976]. Figure 1.6 presents a comparison of the analytical solution for $I(q)$ (red solid line) and the factorized form, $I(q) \propto P(q)S(q)$ (blue solid line). Both curves were calculated using identical input parameters, that is particle radius of 100 nm, $Z = 100$, which corresponds to polydispersity $\sigma = \sigma_r/\langle r\rangle = 0.1$ and volume fraction $\Phi = 0.3$. The factorized form clearly deviates from the analytical solution at low q values and at the first minimum.

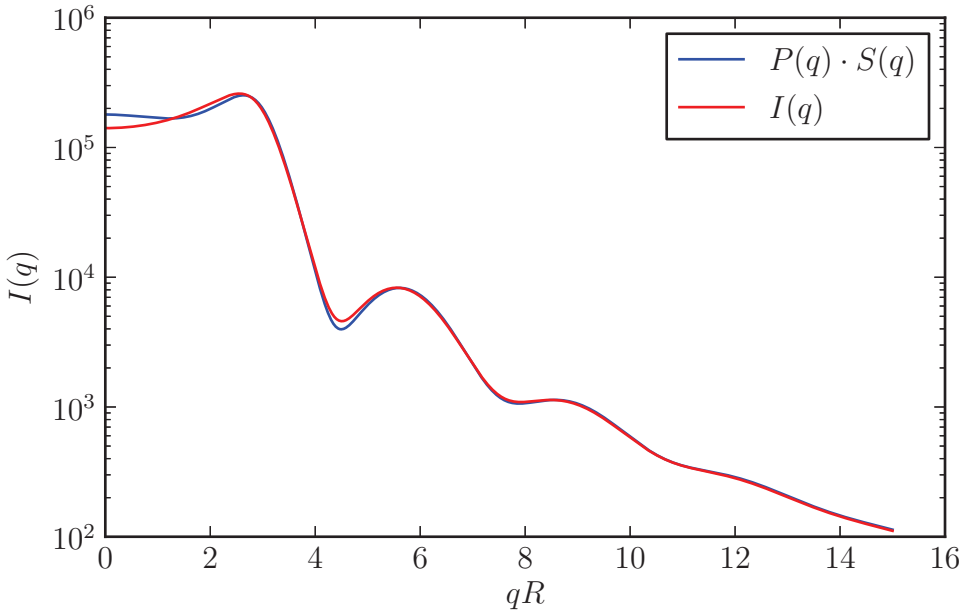

Figure 1.6: Comparison of two models of scattered intensity for a hard-sphere suspension, assuming Schulz size distribution of the particles. The input parameters are identical: $R = 100$ nm, $Z = 100$, $\Phi = 0.3$. The red solid line is the analytical solution of equation 1.21 derived in [Griffith 1987]. The blue solid line is the intensity calculated using equation 1.16, with the form and structure factors obtained from equation 1.21.

Résumé du Chapitre 2

Ce chapitre donne une vue d'ensemble de la technique de spectroscopie de corrélation de photons X (XPCS) l'outil expérimental principalement utilisé dans cette thèse. La XPCS permet d'accéder aux propriétés dynamiques d'un système désordonné, comme les suspensions colloïdales, en mesurant les fluctuations en intensité d'une figure de diffusion de faisceau cohérent. L'utilisation du rayonnement synchrotron, de forte intensité, donne accès à une gamme unique de vecteurs diffusion (pour l'échelle des longueurs) et de fréquences (échelle des énergies). La première partie du chapitre présente une discussion des propriétés de cohérence du faisceau synchrotron de troisième génération. Les figures de diffraction aléatoires (tavelures optiques, ou "speckle"), qui reflètent l'arrangement spatial des centres diffuseurs, sont ensuite introduites. Quand les éléments diffusants sont en mouvement, par exemple sous l'effet du mouvement brownien, les figures dues à la diffraction cohérente fluctuent. Ces fluctuations peuvent être analysées quantitativement via les fonctions de corrélation moyennées dans le temps. La fonction de corrélation mesurée par XPCS donne accès à la fonction de diffusion intermédiaire, qui est reliée au facteur de structure dynamique – une quantité accessible via théorie et simulations. En illustration, le calcul de la fonction de diffusion intermédiaire pour un ensemble dilué de sphères dures montre que le coefficient de diffusion de Stokes-Einstein peut être obtenu par ajustement des courbes expérimentales. L'utilisation d'un détecteur 2D permet de calculer la fonction de corrélation à deux temps, qui peut être utilisée dans les études de dynamique hors équilibre. Le chapitre se clôt sur une description du dispositif expérimental, des détecteurs et des méthodes de calcul des fonctions de corrélation.

Chapter 2

X-ray Photon Correlation Spectroscopy

Contents

2.1 Introduction

X-ray Photon Correlation Spectroscopy is a scattering technique giving information about the dynamic properties of a disordered system. It is equivalent to Dynamic Light Scattering (DLS), which is a well established method performed with visible light [Berne 2000]. Both require a coherent source of radiation – only then the scattered light forms a random diffraction or speckle pattern in the far-field.

It means that the information on the temporal evolution of the scatterers can be deduced from the study of temporal changes of the scattered intensity. This principle is applied in DLS (also named Photon Correlation Spectroscopy (PCS)). Using visible coherent light limits the available q range to values[1] smaller than $\sim 4 \times 10^{-3}$ $\mathring{A}^{-1}$. Shorter X-ray wavelength allows to extend this limit up to several $\mathring{A}^{-1}$, with the additional advantage of negligible multiple scattering – the phenomena common for visible light, where the photon scattered by one scatterer is scattered again, multiple times, by other scatterers before reaching the detector. This significantly complicates DLS measurements and data analysis because the information about the scattering vector is lost. Multiple scattering can be overcome in

1. The calculation of the maximum q assumes back-scattering geometry ($2\theta \approx 180^{\circ}$) and the use of a blue laser with $\lambda = 445$ nm. It should be noted that when calculating the q value for visible light, equation 1.1 has to be modified to include the refractive index n_0 of the sample: $q = 4\pi n_0/\lambda \sin(\theta)$. Taking the refractive index of water: $n_0 = 1.33$ [Lide 2010], the maximum q value is 3.76×10^{-3} $\mathring{A}^{-1}$

visible light regime, to a certain extent, with the use of two-color dynamic light scattering (TCDLS) [Segrè 1995c] or Diffusing Wave Spectroscopy (DWS) [Pine 1988]. Both DLS and XPCS probe slow dynamics ($\omega = Dq^2 < 10^6\ Hz$, with D being the diffusion coefficient). Figure 2.1 presents an overview of the frequency-scattering vector range accessible by these and other methods applied in the study of dynamics in disordered systems [Leheny 2012].

Development of a PCS technique performed with X-rays has only been possible since third generation synchrotrons have been built, providing enough coherent flux.

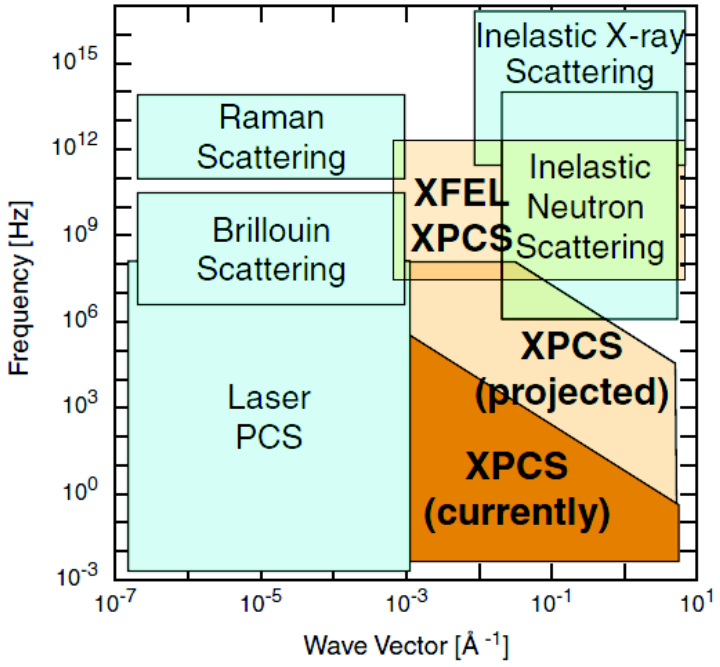

Figure 2.1: Presentation of the frequency-scattering vector space covered by different techniques, reproduced from [Leheny 2012]. XPCS – X-ray Photon Correlation Spectroscopy, PCS – Photon Correlation Spectroscopy (also named DLS – Dynamic Light Scattering).

2.2 Coherent properties of Synchrotron X-rays

The electrons in a storage ring based facility radiate spontaneously and independently. Consequently, only partial coherence may be attributed to the photon beam. A quantitative description of the coherence properties of synchrotron light can be given by providing the values of *longitudinal* and *transverse* coherence lengths.

2.2.1 Coherence of an X-ray beam

An X-ray beam produced by an insertion device deviates from an ideal plane wave in two aspects: it is not perfectly monochromatic and its propagation direction is not perfectly well defined. In this case it is useful to define a length scale on which the beam may be considered coherent [Als-Nielsen 2011].

Longitudinal coherence length, ξ_L takes into account the wavelength (energy) distribution. It is schematically presented in the top part of figure 2.2, showing the wavefronts of two plane waves, initially in phase in point P. Due to the wavelength difference between the two waves ($\Delta\lambda$), phase difference will accumulate along the propagation direction. The distance after which the two waves are out of phase defines ξ_L. Consequently, when the distance from point P is equal to $2\xi_L$, the two waves are in phase again. Marking the number of periods occurring from in-phase to in-phase as N:

$$2\xi_L = N\lambda = (N+1)(\lambda - \Delta\lambda) \tag{2.1}$$

Looking at the second part of the above equation which implies that $(N+1)\Delta\lambda = \lambda$, it can be written that $N \approx \lambda/\Delta\lambda$, and equation 2.1 can be rearranged to obtain the longitudinal coherence length as a function of the wavelength λ and the bandwidth $\Delta\lambda$:

$$\xi_L = \frac{1}{2}\frac{\lambda^2}{\Delta\lambda} \tag{2.2}$$

Coherence loss due to beam divergence is depicted in figure 2.2 (b). The two waves, A and B, have the same wavelength, but their directions of propagation are different by an angle θ. Noting that the wavefronts coincide at point P, the *transverse* coherence length ξ_T can be defined as the distance along the wavefront of wave A after which it is out of phase with wave B. Again, after a distance of $2\xi_T$, the two waves will be in phase. Assuming that the angle θ is small, it can be written that $2\xi_T\theta = \lambda$. The factor responsible for beam divergence is the finite source dimension, marked as D in figure 2.2 (b). By denoting the source-sample distance as R, ξ_T can be written as a function of practical parameters:

$$\xi_T = \frac{\lambda}{2}\frac{R}{D} \tag{2.3}$$

The requirement for a photon beam to be spatially coherent can be written as:

$$\Sigma_x\Sigma'_x\Sigma_z\Sigma'_z \geq \left(\frac{\lambda}{4\pi}\right) \tag{2.4}$$

where Σ is the source size and Σ' is the beam divergence. Typically, this is not fulfilled for X-ray sources, but may be achieved by using collimating apertures, acting as secondary sources of smaller size. The drawback is the photon flux reduction.

Using the above definitions, coherent sample illumination requirement is fulfilled when the maximum path length difference (PLD) for waves scattered by the sample

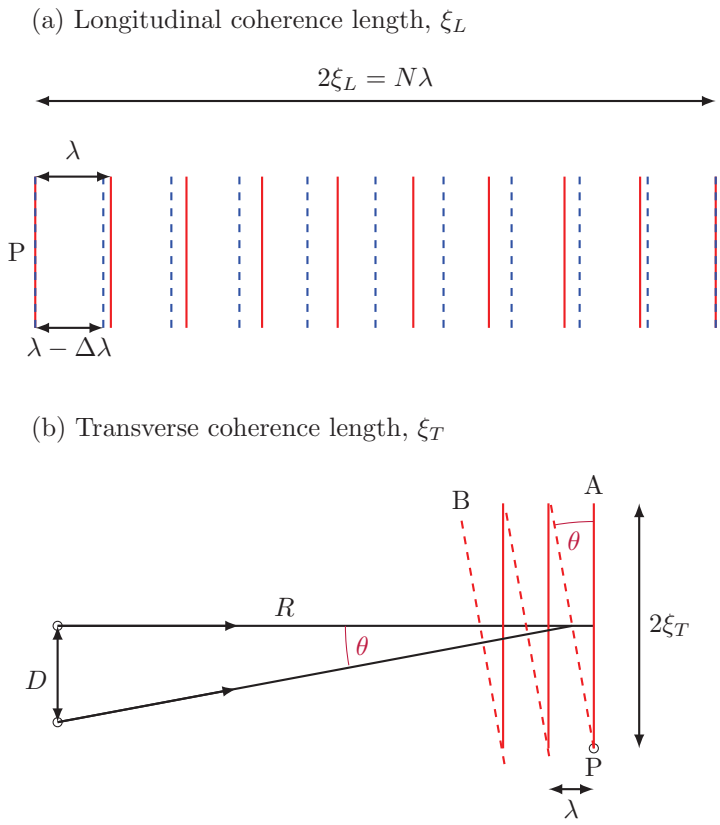

Figure 2.2: Schematic representation of longitudinal and transverse coherence lengths (ξ_L and ξ_T respectively). Adapted from [Als-Nielsen 2011]

is smaller or equal to ξ_L and the lateral size of the illuminated sample is comparable to ξ_T [Grübel 2004]. In transmission geometry, the maximum path length difference is:

$$PLD \approx 2W \sin^2(\theta) + D \sin(2\theta) \tag{2.5}$$

for sample of thickness W, a beam of size D and a scattering angle θ. Knowing the sample thickness and the beam size, equation 2.5 can be used to determine the maximum angle θ_{max}, thus the maximum scattering vector value for which the scattering is still coherent: $q_{max} = (4\pi/\lambda)\sin(\theta_{max})$.

Another important parameter for a scattering experiment is the number of photons in the coherence volume. It can be estimated using a quantity commonly applied to compare the quality of different X-ray beams, called the *brilliance* B. It takes into account not only the number of photons emitted per second, but also the collimation of the beam and its monochromaticity. It is defined as:

$$B = \frac{\text{Photons/sec}}{(\text{mrad})^2(A_s)(0.1\%\text{BW})} \tag{2.6}$$

where A_s is the source area in mm^2. Different X-ray sources produce different spectra – they may be smooth or have peaks at certain energies. Which range of photon energies is present in the measured intensity is an important aspect when a comparison is to be made between the sources. That is why the photon energy range is defined in equation 2.6 as a fixed relative energy bandwidth (BW $= \Delta\lambda/\lambda$), chosen to be 0.1%.

The *coherence area* A_c is defined by the horizontal and vertical transverse coherence lengths, ξ_T^h and ξ_T^v respectively, calculated using equation 2.3 and assuming an elliptical beam cross section:

$$A_c = \pi \xi_T^h \xi_T^v = \frac{\pi(\lambda R)^2}{4 D_h D_v}. \tag{2.7}$$

Here D_h and D_v denote the source size in horizontal and vertical direction, respectively. Analogically, the coherence volume can be defined as $V_c = \xi_L A_c$. The average number of photons Δ_c in V_c can now be expressed by the brilliance, coherence time $\tau_c = \xi_L/c$, the solid angle $\delta\Omega_T = A_c/L^2$ and source area A_s [Lengeler 2001]:

$$\Delta_c = B \cdot \tau_c \cdot \delta\Omega_T \cdot \mathrm{BW} \cdot A_s = B \frac{\lambda^3}{\pi c}, \tag{2.8}$$

where c is the speed of light. The proportionality of Δ_c to λ^3 explains the difficulty of performing a coherent X-ray experiment. The short wavelength ($\lambda \approx 1$ Å) needs to be compensated by high brightness in order to have enough coherent flux. For this reason XPCS became feasible only since third generation synchrotron sources have been available, with undulators giving a brilliance of the order of 10^{20}photons/s/mm^2/mrad^2/0.1%BW.

2.3 Coherent illumination of disordered systems

Scattering of light results in a diffraction pattern. The use of coherent radiation can provide additional information due to the resulting constructive or destructive interference. As an illustration, a pinhole diffraction experiment is considered. In the far field (Fraunhofer) approximation, the diffraction pattern can be fully described by the Fourier power spectrum of the distribution function describing the aperture [Goodman 2005]. Taking a circular pinhole, such as the one shown in figure 2.3 a, a diffraction (or scattering) experiment can be simulated by calculating its Fourier transform. The logarithm of the squared magnitude of the Fourier transform of image 2.3 a is presented in figure 2.3 b. The concentric rings contain information about the structure of the diffracting (scattering) object - the circular pinhole. When the single object is replaced by many, randomly placed ones (figure 2.3 c), individual diffraction patterns interfere with each other, also in a random way, leading to the so called *speckle* pattern (seen as grainy noise on top of the concentric rings – figure 2.3 d). In addition to the information about the shape, it also encodes the spatial arrangement of the diffracting objects. This can be shown

by changing the position of just a single "particle", as marked by the arrow in figure 2.3 c. The resulting speckle pattern (figure 2.3 e) also changes. To better visualize the change, figure 2.3 f shows the intensity values along the diagonal cross sections of panels d (green) and e (red), plotted over the azimuthally averaged radial profile of the figure in panel e (blue).

In a real experiment, when all particles are moving, a point detector employed to measure the scattered intensity in a fixed position in space would register a fluctuating signal. This signal can be analysed with the use of correlation functions.

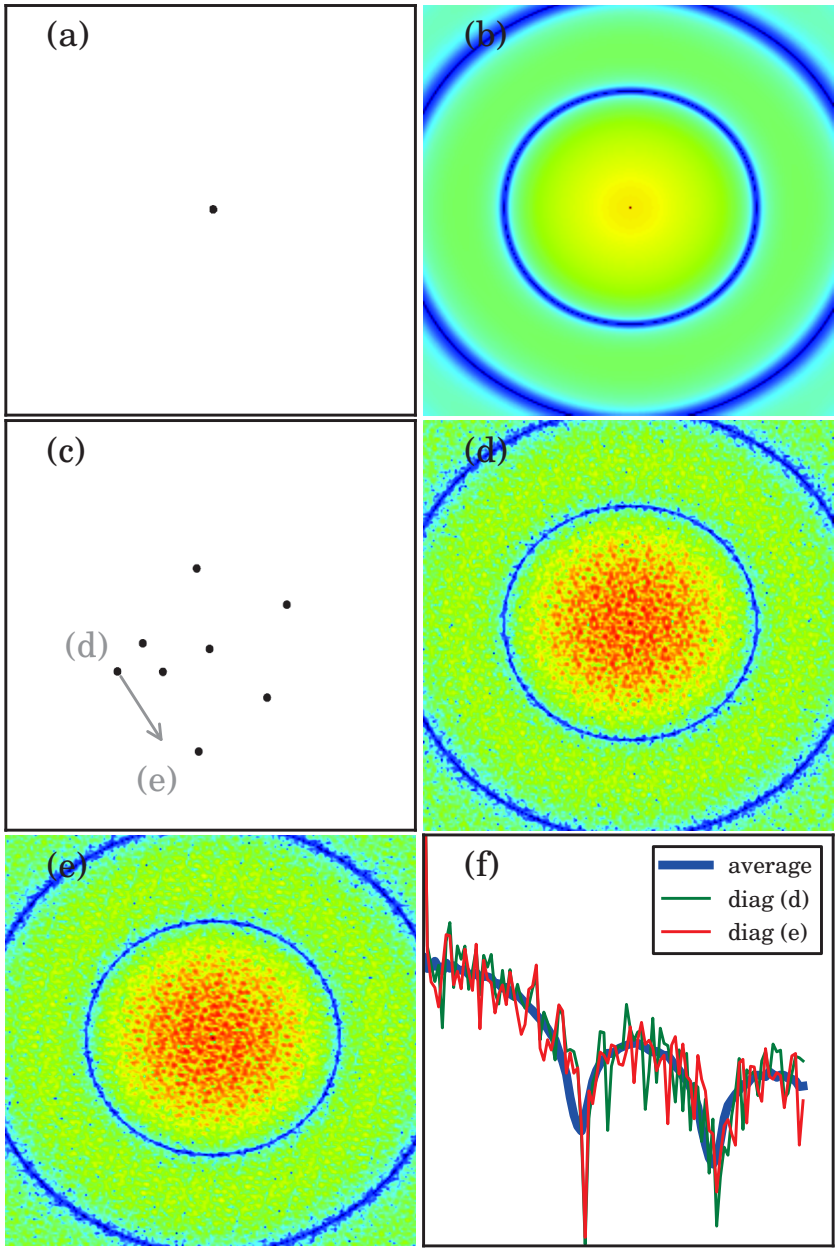

Figure 2.3: Logarithm of the magnitude of the Fourier transform of a single circle image presented in panel (a) is shown in panel (b). The characteristic concentric rings contain the information about the shape of the "scattering" object. Due to coherence, the intensity scattered from multiple, randomly placed identical objects (panel (c)) produces a random diffraction pattern – the *speckle* pattern, shown in panel (d). A displacement of a single "particle", marked by the gray arrow in panel (c), significantly changes the speckle arrangement, as can be seen in the diagonal cross sections presented in panel (f).

2.3.1 Correlation functions

Quantitative analysis of speckles [Grübel 2008] is done by calculating time-averaged temporal intensity autocorrelation functions $g_2(\vec{q},t)$:

$$g_2(\vec{q},t) = \frac{\langle I(\vec{q},\tau)I(\vec{q},\tau+t)\rangle}{\langle I(\vec{q})\rangle^2}. \tag{2.9}$$

Here, $I(\vec{q},\tau)$ denotes the scattered intensity measured at wave vector $\vec{q}$ and time τ. Since intensity is probed with time interval Δt (see figure 2.4), calculation is performed by choosing a point in time τ_0 to serve as origin. $I(\vec{q},\tau_0)$ is multiplied by $I(\vec{q},\tau_1)$, where $\tau_1 = \tau_0 + \Delta t$, and normalized to the time-averaged intensity $\langle I(\vec{q})\rangle^2$. This calculation is averaged for every possible time origin, averaging being indicated by angular brackets in equation 2.9. Subsequent points of the correlation function are calculated by varying the delay time $t = n\Delta t$. This procedure assumes that

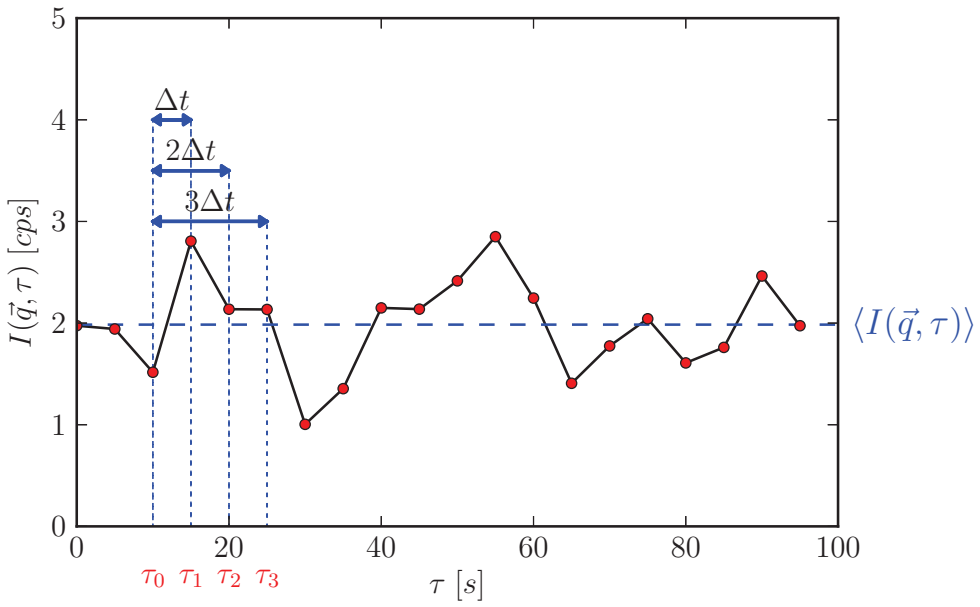

Figure 2.4: A schematic representation of the temporal averaging performed during correlation function calculation using equation 2.9

the value of $g_2(\vec{q},t)$ is independent of the sample age, which is valid only when the sample is *ergodic*, that is when time averages are equivalent to ensemble averages.

The experimentally accessible correlation function can be related to a theoretically accessible quantity if the scattering contains a large number of independent scatterers which undergo thermally excited motion in equilibrium. In this case the central limit theorem implies that the fluctuations in the coherent scattering intensity follow a Gaussian distribution and $g_2(\vec{q},t)$ fully describes the correlation spectrum [Sutton 2002]. The connection with the normalized intermediate scatter-

ing function (ISF) $g_1(\vec{q},t)$ is then provided by the Siegert relation:

$$g_2(\vec{q},t) = 1 + \beta(\vec{q})|g_1(\vec{q},t)|^2, \tag{2.10}$$

where $g_1(\vec{q},t)$ is a ratio of the dynamic structure factor $S(\vec{q},t)$ and the static structure factor $S(\vec{q},0)$:

$$g_1(\vec{q},t) = \frac{S(\vec{q},t)}{S(\vec{q},0)} \tag{2.11}$$

and

$$S(\vec{q},t) = \frac{1}{N[b^2(\vec{q})]} \sum_{n=1}^{N} \sum_{m=1}^{N} \langle b_n(\vec{q}) b_m(\vec{q}) \cdot \exp\left[i\vec{q}[\vec{r}_n(0) - \vec{r}_m(t)]\right]\rangle \tag{2.12}$$

for N scatterers with $b^2(\vec{q})$ being the square of the scattering amplitude averaged over the size distribution of the scatterers, and $\vec{r}_n(t)$ – the position of scatterer n at time t. In equation 2.12 the angular brackets denote ensemble averages over the scattering volume, which for stationary dynamics are equivalent to the time averages performed in equation 2.9.

Parameter $\beta(\vec{q})$ in equation 2.10 denotes the speckle pattern contrast which can be related to the ratio of the coherence volume V_c and the illuminated sample volume V_s. Being close to 1 for visible laser light, the contrast takes a value $0 < \beta < 1$ for partially coherent X-ray beam.

A simple example of dilute, monodisperse, spherical particles undergoing Brownian motion [Berne 2000, Pusey 1991] will now be considered as an illustration. It can be shown that when the positions of different molecules are statistically independent, due to lack of interactions, the cross terms ($n \neq m$) in equation 2.12 average to zero, and $S(\vec{q},0) = 1$. The displacement $\vec{r}_n(0) - \vec{r}_n(t)$ of a free Brownian particle is a Gaussian variable. Its mean square value is given by [Pusey 1991]

$$\langle[\vec{r}_n(0) - \vec{r}_n(t)]^2\rangle = 6D_{0,n}t \tag{2.13}$$

with $D_{0,n}$ being the free particle diffusion coefficient of a particle with radius R_n, known from the Stokes-Einstein relation [Einstein 1905]:

$$D_{0,n} = \frac{k_B T}{6\pi\eta_0 R_n}, \tag{2.14}$$

where k_B is the Boltzman constant, T – temperature and η_0 – shear viscosity of the surrounding medium. Then equation 2.12 reduces to:

$$S(\vec{q},t) = \frac{1}{N[b^2(\vec{q})]} \sum_{n=1}^{N} b_n^2(\vec{q}) \cdot \exp\left[-D_{0,n}q^2 t\right] \tag{2.15}$$

A short-time expansion of 2.15 leads to [Pusey 1991]:

$$S(\vec{q},t) = 1 - \langle D_0\rangle q^2 t + \ldots \tag{2.16}$$

where

$$\langle D_0 \rangle = \sum_{n=1}^{N} b_n^2(\vec{q}) D_{0,n} \tag{2.17}$$

is the diffusion coefficient averaged over the distribution of particle sizes. For monodisperse, non-interacting particles the equation 2.15 reduces to:

$$S(\vec{q},t) = \exp\left[-D_0 q^2 t\right] = g_1(\vec{q},t) \tag{2.18}$$

An example of a correlation function measured for a single value of the scattering vector on a sample of dilute spherical silica particles, suspended in propylene glycol, is shown in figure 2.5. The data points are fitted with an exponential decay, following equations 2.18 and 2.10:

$$g_2(\vec{q},t) = 1 + \beta \exp\left[-2D_0 q^2 t\right] \tag{2.19}$$

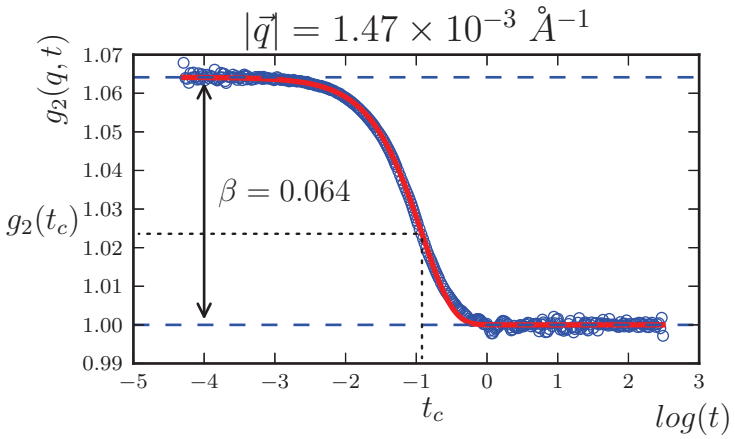

Figure 2.5: An example of a measured correlation function (circles) fitted with a simple exponential decay – equation 2.19 (red solid line). The contrast β determines the value of the initial plateau from which g_2 starts to decay. Correlation time $t_c = 1/2D_0q^2$ marks the point where $g_2(t_c) = 1 + \beta/e$.

2.3.2 Two time correlation functions

When the measured system is non-ergodic, the time averages employed in calculation of $g_2(\vec{q},t)$ are no longer justified. They should be replaced by direct ensemble averaging. One of possible experimental realizations is to use an area detector to record multiple speckles at each point in time [Madsen 2010, Sutton 2003].

To follow the age-dependence of the sample dynamics a two-time correlation function can be calculated:

$$G(q,t_1,t_2) = \frac{\langle I(\vec{q},t_1) I(\vec{q},t_2) \rangle_\Phi}{\langle I(q,t_1) \rangle_\Phi \langle I(q,t_2) \rangle_\Phi}. \tag{2.20}$$

The subscript Φ in the above equation indicates averaging over the ensemble of pixels which correspond to a range of wave vectors $|\vec{q}| = q + \Delta q$ for which the variations of the correlations can be neglected. This method exploits the symmetries of the scattering pattern, such as the azimuthal symmetry of isotropic scattering.

If the time averaging is valid, the regular correlation functions $g_2(q,t)$ can be retrieved by averaging $G(q,t_1,t_2)$ at a fixed delay time $t = t_2 - t_1$:

$$g_2(q,t) = \langle G(q,t_1,t_d)\rangle_{t_d}. \tag{2.21}$$

This procedure is illustrated in figure 2.6. The left panel shows a typical representation of a stationary two time correlation function, with the color-encoded value of $G(q,t_1,t_2)$, increasing from blue to red. The shaded regions, numbered from 1 to 4, indicate where $g_2(q,t)$ was calculated using equation 2.21. The average over $t_d = (t_1 + t_2)/2$ at a fixed delay time $t = t_2 - t_1$ means averaging along the line parallel to the main diagonal ($t_1 = t_2$), at a distance t from the diagonal. The calculated $g_2(q,t)$ curves are shown in the upper right panel. All of them fall on top of each other, indicating that the dynamics does not evolve during the experiment.

Even for non-equilibrium systems examples can be found where the dynamics evolves slowly compared to the measurement time and the time averages involved in the $g_2(q,t)$ calculation are not obviously problematic. Nevertheless, temporal variations of the correlations deduced from $G(q,t_1,t_2)$ can contain important information, not accessible for time-averaged correlation functions. For example, in the case of equilibrium and diffusive motion, the values of $G(q,t_1,t)$ at different t_1 follow a Gaussian probability distribution. Its width is related to the intrinsic statistical noise of the measurement. The time-averaged $g_2(q,t)$ contains all the dynamic information of such a system. If the fluctuations in $G(q,t_1,t)$ are not Gaussian this may indicate non-equilibrium dynamics or collective motion. This information would be lost by time averaging [Madsen 2010].

A quantitative measure of the two time correlation function fluctuations can be obtained by calculating the normalized variance [Duri 2006]:

$$\chi(q,t) = \frac{\langle G^2(q,t_1,t)\rangle_{t_d} - \langle G(q,t_1,t)\rangle^2_{t_d}}{[g_2(q,0)-1]^2}. \tag{2.22}$$

As in equation 2.21, the averages $\langle\ldots\rangle_{t_d}$ are calculated along lines parallel to the mean diagonal at a distance given by t. The value of $\chi(q,t)$ is equal to zero in the case of equilibrium dynamics, as shown in the lower right panel of figure 2.6.

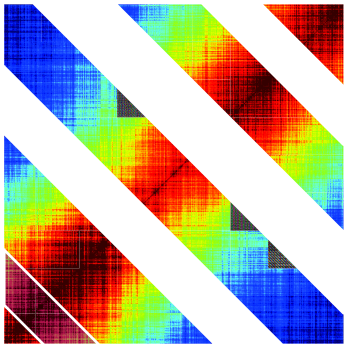

beam, these slits produce a parasitic scattering pattern, which is reduced by placing guard slits just a few centimetres before the sample.

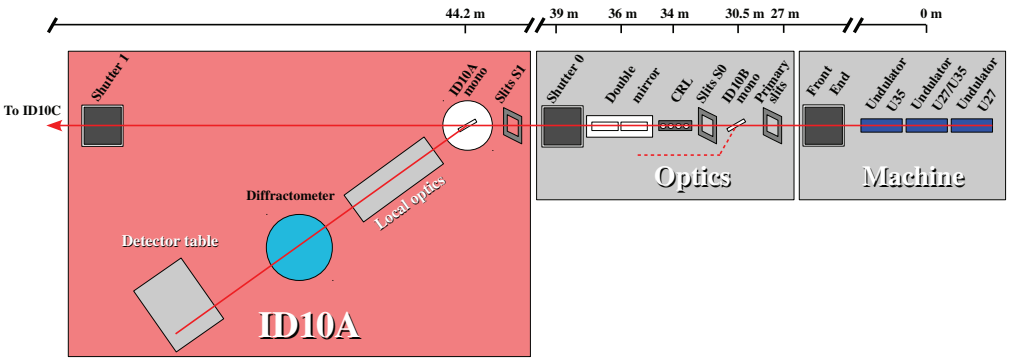

Figure 2.7: Schematic representation of the ID10A beamline layout with typical element distances.

Angular size of an individual speckle d_s is determined by the setup and can be calculated from [Grübel 2008]:

$$d_s \approx \sqrt{\left(\frac{\lambda}{d}\right)^2 + (\Delta\theta)^2} \tag{2.23}$$

with $\Delta\theta$ being the effective angular source size. For optimal measurement conditions, the detector size (pixel size in case of an area detector) should not be larger than the speckle size.

2.4.1 Detectors and correlators

Intensity autocorrelation functions at a selected q value can be readily obtained using a point detector (scintillation counter or avalanche photodiode) and a hardware correlator. There are several factors which determine the fastest time scales accessible for XPCS. One of them is the count rate – approximately one photon per second should be counted, thus a measurement of 100 Hz dynamics requires at least 100 Hz count rate. Another limiting factor is the detector's dead time. With avalanche photodiodes, having a dead time in the order of 1 ns or less, the limits of the correlator electronics may be reached, or the time structure of the synchrotron storage ring starts to be visible in the measured correlation functions [Grübel 2008].

When the measured dynamics is slow enough a 2D detector can be used to collect a series of scattering patterns which allow for a *multispeckle* analysis [Lumma 2000b]. In this study the MAXIPIX pixelated detector [Ponchut 2011] has been used. It consists of a single MEDIPIX-2 photon-counting chip comprising 256×256 pixels, each with an area of 55×55 μm^2. Maximum acquisition rate

is 1 kHz. Each pixel is an independent scintillation counter with properly defined detection limits and gain, therefore no dark current can be observed.

In the case of isotropic scattering pattern, a correlation function calculated for a single pixel can be averaged with the ones calculated for pixels corresponding to the same $|\vec{q}|$ (the ring depicted in figure 2.8). In this work the analysis was performed using a program developed in Python programming language by Chiara Caronna and Yuriy Chushkin. The code is based on the *multi-tau* algorithm for calculating correlation functions, described in details e.g. in [Cipelletti 1999]. In this algorithm the spacing of the correlator channels is quasi-logarithmic, which allows to probe several decades in delay times with a limited number of channels. The basic principle is to implement a set of linear correlators, each with a small number of channels (typically 16), evenly spaced in time. The delay time, as well as the sampling time, doubles from one correlator to the next. The final correlation function is obtained by merging the output of all linear correlators.

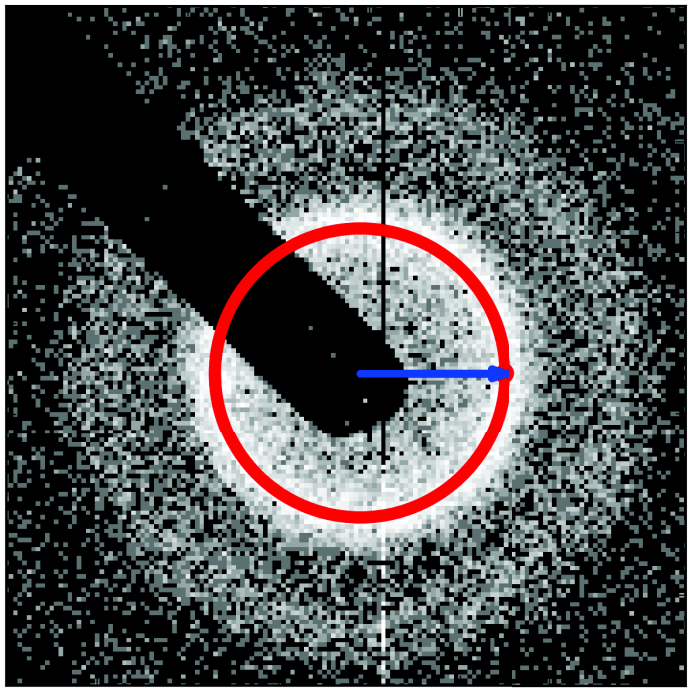

Figure 2.8: Speckle pattern registered with a 2D detector. Since the scattering is isotropic, the correlation function calculated for a single pixel, corresponding to a single $\vec{q}$, can be ensemble averaged with correlation functions calculated for other pixels corresponding to the same magnitude of the scattering vector $|\vec{q}|$.

Despite requiring more elaborate and time consuming data processing, the use of an area detector has several important advantages over the point detector. Firstly,

the correlation functions for multiple q values are measured at the same time. This gives a set of correlation functions measured at the same sample age – an important factor when the dynamics evolves in time.

Secondly, the pixel-averaging (see the numerator of equation 2.24) performed before normalization (denominator in equation 2.24) is equivalent to ensemble average. This is very important when non-ergodic samples are studied, as shown e.g. in [Pusey 1989].

Thirdly, *fully symmetric* normalization is applied, described as:

$$g_2(\vec{q},t) = \frac{\langle\langle I_p(\vec{q},\tau) I_p(\vec{q},\tau+t)\rangle_\Phi\rangle_\tau}{\langle\langle I_p(\vec{q},\tau)\rangle_\Phi\rangle_{0\leq\tau\leq(\tau_r-t)}\langle\langle I_p(\vec{q},\tau)\rangle_\Phi\rangle_{t\leq\tau\leq\tau_r}}, \tag{2.24}$$

where τ_r is the duration of the measurement, $\langle\ldots\rangle_\Phi$ marks averaging over pixels, and $\langle\ldots\rangle_{t_1\leq t\leq t_2}$ denotes the time averaging from t_1 to t_2, with starting time $t = 0$. It reduces the sensitivity to drifts and instabilities of the X-ray beam, by averaging the values of the mean intensity (denominator in equation 2.24) over the same periods of time during which the data used to calculate the numerator of equation 2.24 are accumulated.

Finally, a multi-speckle scattering pattern can be used to perform analysis of anisotropic dynamics, by choosing the pixels corresponding to a specific direction of $\vec{q}$ (see figure 2.9). With a point detector, this would require repeating the measurement, while a series of 2D data allows to obtain correlation functions for different orientations of $\vec{q}$ by masking different pixels.

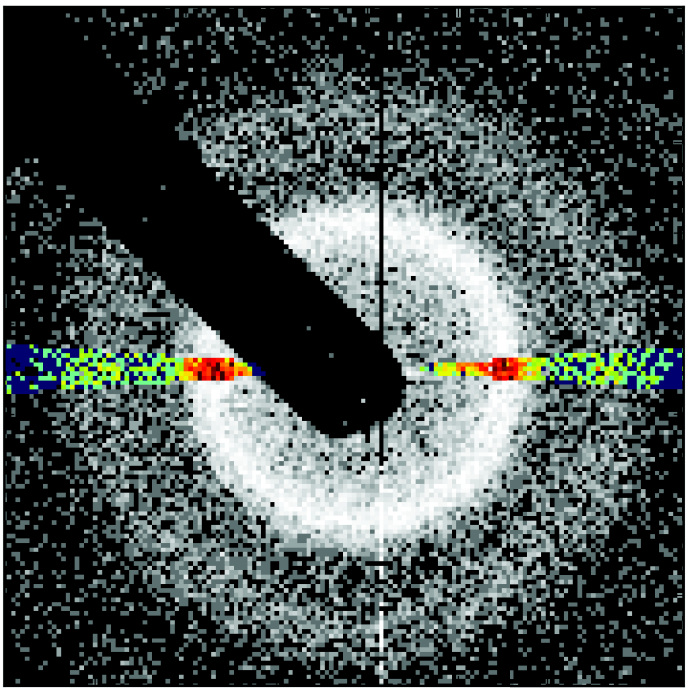

Figure 2.9: Having a data series recorded with a 2D detector facilitates the analysis of anisotropic dynamics. Pixels to calculate the correlation function can be chosen corresponding to a given direction of $\vec{q}$. Correlation functions corresponding to different orientations of $\vec{q}$ can be obtained from a single data set.

Résumé du Chapitre 3

Le système étudié dans cette thèse est une suspension colloïdale modèle de sphères dures. C'est un des systèmes les plus simples et les plus largement étudiés, et pourtant il n'est pas encore totalement compris. Le chapitre donne une introduction générale au sujet des suspensions colloïdales, en s'intéressant particulièrement aux particules de type sphères dures. Ces particules nécessitent d'être stabilisées afin de contrer les forces de Van der Waals attractives, qui ne sont pas négligeables aux échelles colloïdales. Les principes de base des stabilisations stérique et électrostatique sont donc introduits. La deuxième partie du chapitre décrit les détails de la préparation et de la caractérisation des échantillons pour les deux systèmes utilisés: sphères de silice en suspension dans le propylène glycol, et particules de poly(méthyl méthacrylate) (PMMA) dans la décaline. Les particules de silice ont été étudiées en suspension diluée, où les particules peuvent être considérées comme diffusant librement. Les suspensions de PMMA ont été préparées à haute fraction volumique par centrifugation et aspiration de la quantité requise de surnageant. Le chapitre finit sur une description des propriétés dynamiques des suspensions très concentrées. Plusieurs échelles de temps caractéristiques peuvent être distinguées, qui sont discutées.

Chapter 3

Colloidal suspensions

Contents

3.1 Introduction to colloids

Colloidal suspension is a very general term, applied to a broad range of systems present in every-day life, like smoke, fog, printing ink, paints, milk, mayonnaise, insulating foam, ... The common feature of these different substances is that all of them consist of at least two components, A and B, which do *not* form a mixture on molecular level. In other words, substance A is insoluble in substance B. Instead, A is broken down into small particles uniformly distributed in B. Substance A is called the *disperse phase*, and substance B – *dispersion medium*. Both of them may be either solids, liquids or gases.

The size range of the disperse phase is not strictly defined. Usually, the lower limit is given as around 1 nm radius, with the justification that smaller particles would be indistinguishable from true solutions. The arbitrary upper limit is typically set to 1 μm, with a remark that there is no clear difference in the behavior of somewhat larger particles, often present in different systems [Hunter 1990].

Ubiquitous in every-day life, colloids play also a great role in fundamental science [Pusey 1991]. Availability of synthetic model systems composed of spherical particles (e.g. [Antl 1986]) enabled experimental studies which can be compared to theoretical and simulation results. A suspension of nearly identical colloidal particles can be often treated with the formalism derived for atomic systems, as their thermodynamic properties are almost the same [Onsager 1933]. Colloids, regarded as an assembly of "super-atoms" are very attractive to study phenomena like phase

transitions [Löwen 1994]. Due to their *mesoscopic* length scale they are simpler to approach with experimental techniques.

Because of the attractive van der Waals forces, acting between any two bodies of matter, a suspension of particles would inevitably aggregate without an additional protection. Two commonly used approaches include charge and steric stabilization.

3.1.1 Colloidal stability

The description of inter-particle interactions can be obtained with the use of a potential of mean force $U[\vec{r}_j]$, depending on the particle positions $\vec{r}_j$. It is assumed to be a sum of pair potentials $V(\vec{r}_j - \vec{r}_k)$. For spherical particles it can be taken to be spherically symmetrical, and expressed as:

$$U[\vec{r}_j] = \sum_{j>k} |\vec{r}_j - \vec{r}_k|. \tag{3.1}$$

This description implies that the interaction between a pair of particles, j and k, is not affected by the presence of other particles, which is a good approximation in case of short-range interactions. With long-range forces, like the screened Coulombic interaction of charged particles discussed later in this paragraph, the presence of a third particle will affect the pair interactions. Even in this case it can be assumed that an *effective* pair potential can be defined.

The first component of the interaction is the attractive van der Waals, or London-van der Waals force, for particles of radius R described by equation:

$$V_A(r) = -\frac{A}{6}\left[\frac{2R^2}{r^2-4R^2} + \frac{2R^2}{r^2} + \ln\left(1 - \frac{4R^2}{r^2}\right)\right] \tag{3.2}$$

where r is the centre-to-centre separation and A is the Hamaker constant, depending on material properties of both the particles and the suspending medium. In the limit of large distances ($r \to \infty$), equation 3.2 leads to a $V_A(r) \propto r^{-6}$ behaviour:

$$\lim_{r\to\infty} -\frac{16}{9} A \left[\frac{R}{r}\right]^6, \tag{3.3}$$

similar to the long range limit of the Lennard-Jones potential, describing the attraction between two atoms. The small distance limit ($r \to 2R$ - particles are close to touching) of the form:

$$\lim_{r\to 2R} -\frac{A}{12}\frac{R}{r-2R} \tag{3.4}$$

is a deep attractive potential, theoretically infinite when $r = 2R$, in practice limited by the repulsion of overlapping electron clouds and solvation forces, associated with the finite size of the suspending liquid molecules [Pusey 1991].

One way of preventing particle aggregation due to the van der Waals forces is by introducing charges. Charged colloidal particles can be described as *macroions*. Their dispersion in a polar liquid, like water, will cause partial dissociation of the ionisable surface groups. The acquired particle charge, typically of the order 10^2 –

10^5 elementary charges e, leads to formation of an electrical *double layer* surrounding the particle. It is kept by the Coulombic forces acting on the counterions, not allowing them to completely diffuse from the particle. The effective pair interaction of charged macroions can be approximately described by the screened Coulombic (Yukawa) potential:

$$V_C(r) = \begin{cases} \infty & r < 2R \\ \frac{q_e^2}{\varepsilon r} \exp\left(-\kappa_e r\right) & r > 2R \end{cases} \tag{3.5}$$

Here, q_e is the effective particle charge, κ_e an effective screening parameter, and ε – the dielectric constant of the suspending liquid. The complete pair potential of charged particles is a sum of the van der Waals attraction (equation 3.2) and the Coulombic repulsion (equation 3.5). Its exact form depends on particle concentration and temperature via the parameter A, κ_e and ε.

Another method of providing colloidal stability is to coat the particles with a layer of polymer, which can be either physically adsorbed to the surface or chemically bonded. This is called *steric* stabilization. The general principle can be explained by considering a close approach of such core-shell particles. The compression of the interpenetrating polymer layer will cause a strong repulsion overcoming the van der Waals attraction. At slightly larger distances, where the polymers are no longer compressed but the layers still overlap, the specific polymer-polymer interactions become important. Their character depends on the temperature-dependent degree of solvency of the suspending liquid for the polymer. In *good solvents*, the polymer-solvent contacts are energetically favoured over polymer-polymer and solvent-solvent contacts. This results in a repulsive interaction between the polymer chains and expansion of the random coil polymers. On the other hand, *poor solvents* are defined as the ones in which the polymer-polymer contacts are favoured, leading to attractive potential, association of the polymer molecules and contracted polymer coils. For a given polymer-solvent pair, the so-called θ-temperature can be found, at which there are no interactions between the polymers [Pusey 1991, Hunter 1989].

Steric stabilization offers several advantages over electrostatic. First of all, charge stabilization is very sensitive to the presence and concentration of electrolytes in the dispersion, while the steric stabilizing layer is weakly influenced by this factor. Secondly, coatings can be found which will provide stability in both aqueous and non-aqueous media. Charge stabilization is not as effective in non-polar liquids as it is in polar ones. Third, the two methods also differ in effectiveness at high volume fractions, with steric stabilization being superior in this aspect. Another advantage is that dispersions stabilized sterically usually have a good freeze–thaw stability, as well as reversible flocculation, which is less common with electrostatically stabilized suspensions. [Hunter 1989].

3.1.2 Phase diagram of hard-sphere colloids

As in the case of molecular systems, also for colloids a phase diagram can be found for a given interaction potential. For the simplest hard-sphere interaction the

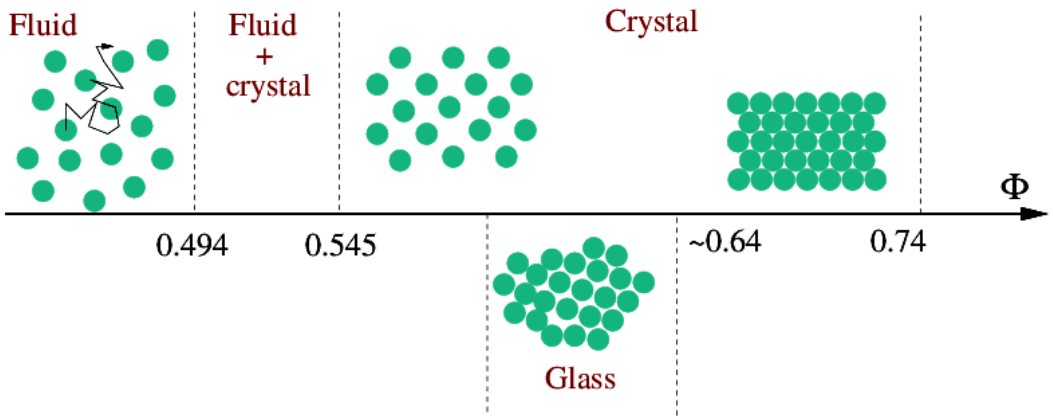

Figure 3.1: A schematic representation of the hard-sphere phase diagram (courtesy of Dr Andrei Fluerasu).

phase diagram is governed by a single parameter – the particle volume fraction Φ, which is defined as the ratio between the volume occupied by the total number of particles in the sample N and the sample volume V:

$$\Phi = \frac{4}{3}\pi R^3 \frac{N}{V}. \tag{3.6}$$

The phase diagram is schematically presented in figure 3.1. Upon increasing Φ the "hard-sphere fluid" undergoes a freezing transition at $\Phi_F = 0.494$. A narrow region of fluid-crystal coexistence is identified between $0.494 < \Phi < 0.545$. Above the melting point $\Phi_M = 0.545$ the equilibrium state is reached in face centred cubic (FCC) structure. The highest possible crystal packing is reached at $\Phi = 0.74$. Fast enough compression may overcome crystallization, leading to a "supercooled" liquid state above Φ_F, which finally leads to a solid glass state. The glass transition has been identified from computer simulation studies at $\Phi_g \approx 0.58$ [Woodcock 1981]. The highest concentration available for an amorphous hard-sphere system is the random close-packing (RCP) $\Phi_R \approx 0.64$ [Pusey 1991].

Pusey and van Megen [Pusey 1986] have demonstrated that a model system of sterically stabilized poly(methyl methacrylate) (PMMA) particles suspended in an index matching mixture of decalin and carbon disulphide follows very well the hard-sphere phase diagram sketched above.

3.2 The samples

There are several commonly encountered model colloidal suspensions of spherical particles. They differ in the particle composition, the suspending medium and inter-particle potential. A broad overview is given in e.g. [Pusey 1991]. This section gives the details of two systems used in this study: silica spheres suspended in propylene glycol (PG) and PMMA particles suspended in decalin.

3.2.1 Silica spheres

The sample used for studies at low volume fractions under flow was prepared from a dispersion of silica spheres in deionized water purchased from Thermo Scientific. The particles are sold as size standards. Their basic physical properties are presented in table 3.1. Silica spheres are charge-stabilized by a surface layer of hydroxyl groups (Si–O–H), which dissociate in water leaving the particles negatively charged:

$$\mathrm{SiOH} \rightarrow \mathrm{SiO^-} + \mathrm{H^+} \tag{3.7}$$

Table 3.1: Characteristics of the silica spheres in water according to the manufacturer's documents.

Parameter	Value
Diameter	0.49 μm $\pm$ 0.02 μm
Density	1.83 g/cm^3
Vol. frac.	0.02

These relatively large particles were chosen to obtain enough scattered intensity even from a suspension at volume fraction of about 0.01. The aim of suspending liquid exchange, from water to PG, was to slow down particle sedimentation, thanks to approximately 50 times higher viscosity of PG at room temperature.

The solvent exchange procedure included two steps. First, water was exchanged to methanol. In the second step methanol was exchanged to propylene glycol. The first step was applied in order to facilitate the evaporation of residual liquid from PG. Liquid exchange was done by centrifuging the desired volume of the sample in a plastic vial for about 5 min. at 5000 rpm. After carefully removing the supernatant, a volume of the target liquid was added. The particles were redispersed with a vortex mixer. The step of exchange to methanol was repeated 10 times. The exchange to PG was performed only once to avoid the difficulties of particle redispersion in the highly viscous medium. The amount of PG added was calculated to give a suspension of about 0.01 volume fraction. In order to get rid of the residual methanol and air bubbles, the sample was left for several hours under vacuum in a dessicator.

Part of the silica samples used in this work was prepared by Chiara Caronna.

3.2.2 Polymethylmetacrylate particles in decalin

One of the systems most often used in the study of dynamics of colloidal suspensions consists of PMMA particles, sterically stabilized by a thin layer of poly-12--hydroxystearic acid (PHSA), suspended in decahydronaphthalene (decalin). The samples used in this work, purchased from Andrew Schofield [1], were synthesized

1. University of Edinburgh

according to the procedure described in details in [Antl 1986].

This particular system is very well suited for dynamic light scattering experiments due to the possibility of suppressing multiple scattering. Since visible light scatters at the interfaces with different refractive index, the amount of multiple scattering can be decreased by choosing a suspending liquid which has the refractive index similar to the one of the suspended particles. A detailed study of the phase diagram of a colloidal suspension of PMMA particles has been shown to follow that of perfect hard spheres [Pusey 1986].

In order to determine the mass fraction of the stock suspension the following procedure was applied. A sample of 2 ml was carefully weighed using a standard laboratory electronic balance. This sample was then left to dry in a furnace at 80 $°C$ for approximately 24 hours. After that the sample was kept under vacuum in a dessicator for another 24 hours in order to get rid of possible traces of the suspending liquid. The dried particles were weighed, giving the mass fraction by calculating:

$$C_m = \frac{m_p}{m_p + m_s} \tag{3.8}$$

where m_p is the mass of dry particles and m_s is the solvent mass. The obtained value was $C_m = 0.348 \pm 0.002$ with the uncertainty calculated from the balance precision.

To roughly estimate the stock solution volume fraction, the obtained mass fraction was converted to Φ using a literature value of dry PMMA density: $d_p = 1.188 \pm 0.016\ g/cm^3$ [Lide 2010]. The solvent density was measured at 20 $°C$ using a PAAR DMA 58 density meter, giving a value of $d_s = 0.880 \pm 0.001\ g/ml$, in perfect agreement with tabulated values. Calculation of the volume fraction:

$$\Phi = \frac{V_p}{V_p + V_s}, \tag{3.9}$$

where V_p and V_s are the volumes of the particles and the suspending liquid respectively, was done by expressing the volumes in equation 3.9 by corresponding densities and masses: $V = m/d$. Simple transformations using equations 3.8 and 3.9 then lead to the following expression:

$$\Phi = \frac{1}{1 + d_p/d_s(1/C_m - 1)} = 0.28 \pm 0.01. \tag{3.10}$$

The uncertainty of Φ was calculated using error propagation, including the uncertainty of C_m and d_p, the latter estimated as the difference between the bulk PMMA density used in this thesis and a measured value of particle density, reported in table 1 of reference [Bartlett 1992].

A higher estimate of $\Phi = 0.335$ of the stock solution volume fraction was obtained from fits of the SAXS curve measured at the ID02 beamline at ESRF (lower panel of figure 3.2). The scattering intensity was fitted with the analytical expression for a polydisperse Percus-Yevick fluid, assuming Schulz distribution of particle radii, as derived in [Griffith 1987] and described in more details in section 1.2.2 of

this thesis. There are several factors which can contribute to this large discrepancy. First of all, the particle density is usually lower than the dry PMMA density assumed in the calculation using equation 3.10, because of possible mixing of the stabilizing polymers with the particle core. Secondly, the particle size distribution function may be different from the one assumed in the fitted model. This can also influence the obtained value of Φ. Thirdly, a concentration gradient might have been present in the sample used for SAXS measurement due to the density difference between the particles and decalin. In this case a measurement taken on the bottom part of the capillary would lead to the value of Φ higher than that of the stock suspension.

The uncertainty of the fitted value of Φ cannot be reasonably estimated using the standard statistical approach because of the extremely small uncertainties of the measured $I(q)$ values – typically 0.1% of $I(q)$. The disagreement between the model curve and the data at high q ($q > 0.08\ nm^{-1}$), probably originating from the different particle size distribution than the assumed in the model, makes the best fit not satisfying in terms of the reduced χ^2, calculated as:

$$\chi^2_{red} = \frac{1}{\nu}\sum_{i=1}^{N}\frac{(I_i - I_i^m)^2}{\sigma_i^2}. \tag{3.11}$$

Here ν is the number of degrees of freedom: $\nu = N-n-1$, where N is the number of data points and n is the number of fitted parameters, I_i^m denotes the fitted value of intensity and σ_i^2 is the experimental uncertainty of the measured intensity I_i. A fit is considered good when $\chi^2_{red} \approx 1$, that is when the squared differences between the data and the model are of the order of σ_i^2. In the case of fits presented in figure 3.2, the calculated χ^2_{red} is of the order of 10^6, rendering the calculation of fit parameter uncertainties meaningless. Following the discussion presented in [Poon 2012], the practical uncertainty of any volume fraction estimate should be assumed $\gtrsim 0.03$.

A SAXS measurement taken at the ID02 beamline on a sample prepared by diluting the stock suspension 200 times was used as an "experimental form factor" and to obtain the particle radius and polydispersity (see the upper panel of figure 3.2). In both fits of the stock and dilute sample the amplitude of high q oscillations is smaller in the fitted curve than in the experimental data. One possible explanation of this feature is that the real particle size distribution function is more skewed towards larger sizes than the assumed Schulz distribution [Narayanan 2008].

Samples at higher volume fractions were prepared by first centrifuging a known mass of the stock suspension at 5000 rpm for about 24 hours, until all the particles were compacted on the bottom of the vial. The mass of solvent δ_m which was extracted to obtain the desired final volume fraction Φ_f was calculated from the following expression [Segrè 1995a]

$$\Phi_f = \frac{\Phi_i}{1 + \delta_m/m_T[(d_p/d_s - 1)\Phi_i + 1]}. \tag{3.12}$$

Here Φ_i is the stock suspension volume fraction, m_T is the total mass of the sample, d_p – particle density and d_s – solvent density. Because the above method

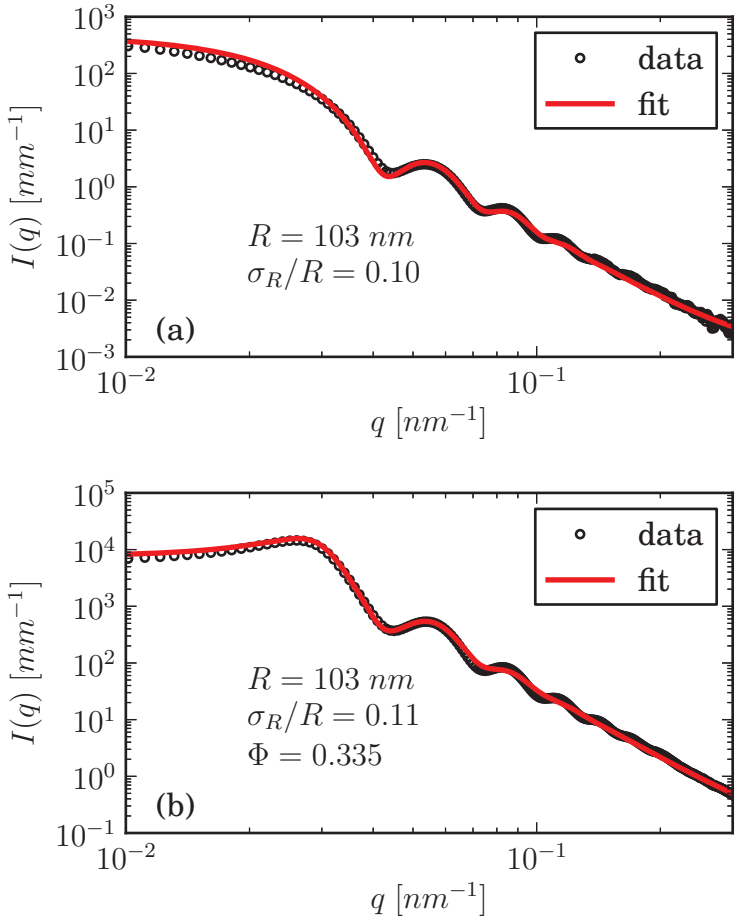

Figure 3.2: Results of fits of the scattered intensity from PMMA particles: (a) measurement taken on a sample diluted 200 times from the stock suspension; (b) data from the stock suspension. The continuous red line is a fit of the analytical expression derived in [Griffith 1987], describing the scattered intensity from a polydisperse Percus-Yevick fluid of hard spheres with radii distributed according to the Schulz distribution.

of determining Φ requires the knowledge of particle density, which is difficult to obtain with good precision, the volume fraction of the samples was again measured by fitting SAXS data.

3.3 Dynamics of hard-sphere colloids

The large difference in size between the suspending liquid molecules and colloidal particles allows to apply a coarse-grained description of the suspension's dynamics. Instead of using Newton's laws of motion, describing the time evolution of

individual molecular trajectories, or the Liouville equations, giving the phase-space probability density time evolution, the effect of the suspending liquid molecules can be averaged to random forces acting on the colloidal particles. Two equivalent approaches have been developed for this purpose. One of them is the Fokker-Planck equation describing the probability density of the particles' positions and velocities, analogically to the Liouville equation. The analogue of Newton's equations of motion is a set of Langevin equations. The large mass of particles makes their velocity fluctuations occur on a time scale τ_B, over which their position changes very little – a small fraction of their radii. This allows for further reduction of the description to a configuration space containing explicitly only particle positions, leading the Fokker-Planck equation to the many-particle diffusion Smoluchowski equation. In the Langevin equations, the velocity integration leads to coupled position Langevin equations. At this level of description it is possible to identify three factors which influence the motion of colloidal particles: Brownian forces, resulting from multiple collisions with the liquid molecules, leading to random particle displacements on time scales $\gg \tau_B$; direct particle interactions, like collisions, and indirect hydrodynamic interactions, mediated by the suspending medium. In practice, diluting the suspension decreases the strength of hydrodynamic interactions. It is convenient to consider separately the simpler case in which the hydrodynamic interactions can be neglected – a dilute colloidal suspension, and the more complex system, e.g. a suspension of hard spheres at high volume fractions, in which the interactions mediated by the suspending liquid are important [Pusey 1991]. The connection between the correlation function measured using XPCS (or, more generally - photon correlation spectroscopy) and the free diffusion coefficient characterizing Brownian dynamics of a dilute colloidal suspension of hard spheres has been discussed in the example presented in section 2.3.1. Here an introduction is given to the dynamics at high volume fractions.

3.3.1 Relevant time scales

Dynamics of colloidal suspensions at high volume fractions is a very complex problem, even in the simple case of hard-sphere like particles. All three factors influencing the particle movement – Brownian forces, particle collisions and hydrodynamic interactions, must be taken into account. A characteristic time scale can be related to each of these contributions.

The Brownian relaxation time, τ_B, can be calculated given the particle mass m and its friction coefficient in the suspending liquid $f = 6\pi\eta_0 R$:

$$\tau_B = \frac{m}{6\pi\eta_0 R} \tag{3.13}$$

with η_0 denoting the dynamic viscosity of the suspending liquid. For times $\tau \gg \tau_B$ the particle movement can be considered diffusive, while at shorter times, $\tau \ll \tau_B$, it evolves from ballistic to diffusive. Considering the mean-square displacement of a free Brownian particle:

$$\langle \Delta r^2(t) \rangle = 6D_0 t \tag{3.14}$$

it can be calculated that the typical particle displacement in time of the order of τ_B is much smaller than its radius. A more detailed discussion presented in [Pusey 1991] shows that direct particle interactions require much larger movements. The related *structural relaxation time* τ_R can be evaluated from:

$$\tau_R = \frac{R^2}{D_0}. \tag{3.15}$$

The values of τ_B and τ_R calculated for the PMMA suspension in decalin used in this thesis are presented in table 3.2.

The time relevant for hydrodynamic interactions τ_H can be estimated as the time taken by a viscous shear wave to propagate between two particles:

$$\tau_H \approx (\rho^{-1/3})^2 \frac{\mu_0}{\eta_0} \tag{3.16}$$

with ρ being the particle number density and μ_0 the suspending medium density. Knowing that the mean interparticle spacing in a moderately concentrated suspension is of the order of particle radius, τ_H is similar to τ_B. Since the time scales accessible for XPCS (or DLS) in the systems considered in this thesis are well above τ_B, the hydrodynamic interactions are practically instantaneous.

Table 3.2: Characteristic time scales for PMMA particles – τ_B, calculated using equation 3.13 and τ_R with equation 3.15. The following values were taken: 1.188 g/cm^3 for PMMA density, $\eta = 2.6\ mPa \cdot s$, $D_0 = 8.5 \times 10^{-13}$ m^2/s.

R [nm]	τ_B [s]	τ_R [s]	τ_R/τ_B
103	1.08×10^{-9}	1.2×10^{-2}	1.16×10^{7}

A clear separation between τ_B and τ_R (see: the value of τ_R/τ_B in table 3.2) allows to define short- and long-time dynamics limits. At short times, $\tau_B \ll t < \tau_R$, particle Brownian motion is influenced only by hydrodynamic interactions. In the long-time limit, that is for times $t > \tau_R$, both hydrodynamic and direct interactions contribute. In the context of an experimentally accessible intermediate scattering function, inclusion of particle interactions can be accounted for by a q and time dependent diffusion coefficient, expressed by the derivative of $g_1(q,t)$:

$$\frac{\partial g_1(q,t)}{\partial t} = -D(q,t)q^2 g_1(q,t). \tag{3.17}$$

In analogy to the time scales, short- and long-time diffusion coefficients can be defined, as:

$$D_S(q) \equiv \lim_{\tau_B \ll t < \tau_R} D(q,t) \tag{3.18}$$

$$D_L(q) \equiv \lim_{t > \tau_R} D(q,t) \tag{3.19}$$

The above discussion can be concluded in a remark that the dynamics on different time scales is based on different mechanisms. In the short-time limit the particles move by a fraction of their radius and their configuration is not distorted. Long-time dynamics includes significant configuration changes caused by multiple collisions between the particles.

3.3.2 Short- and long-time diffusion

The short-time diffusion coefficient includes contributions from Brownian diffusion and the solvent-mediated interactions, which can be expressed by the hydrodynamic function $H(q)$:

$$D_S(q) = D_0 \frac{H(q)}{S(q)} \tag{3.20}$$

where $S(q)$ is the static structure factor, indicating also the structural dependence of $D_S(q)$. In the high dilution limit $H(q) \to 1$ and $S(q) \to 1$, leaving D_S equal to the free diffusion coefficient. At higher concentrations the hydrodynamic function typically takes values $H(q) < 1$, leading to a slowing down of the diffusion. The theory describing $D_S(q)$ including hydrodynamic interactions in a hard-sphere system was developed by Beenakker and Mazur in [Beenakker 1983, Beenakker 1984]. Its predictions were demonstrated to be in good agreement with DLS [Segrè 1995a] and XPCS [Orsi 2012b] results up to particle volume fraction $\Phi \sim 0.4$. For higher concentrations (up to $\Phi \sim 0.494$) the rescaled mode-coupling theory (MCT) [Banchio 1999b] provides better predictions for the peak position of $H(q)$ vs Φ, as was demonstrated in a comparison of simulation and experimental data by Banchio *et al.* [Banchio 2008], as well as in the XPCS study of Orsi *et al.* [Orsi 2012b].

Long-time behaviour is a more complex problem, its theoretical treatment is less developed. Few approximative theoretical approaches exist, e.g. [Medina-Noyola 1988, Tokuyama 1995]. A detailed discussion, presented e.g. in [Pusey 1991, Zhang 2006], introduces the long-time diffusion coefficient related to the memory function, indicating the dependence of $\partial g_1(q,t)/\partial t$ also on the condition at time $t' \leq t$. Calculation of the memory function is not trivial and requires approximations. It has been performed within the mode-coupling approximation [Hess 1980, Hess 1983], which in principle does not include hydrodynamic interactions. In the MCT the short-time relaxation is called the β relaxation and is related to the particle motion within a cage formed by its neighbours. Caging implies that the process is nonergodic. It is followed by the long-time, ergodicity-restoring α relaxation, which diverges when glass transition is approached. The α process is related to the breakdown of the cages leading to large-scale particle diffusion. Particle caging has been directly observed in hard-sphere like suspensions using optical video microscopy [Kasper 1998]. In its basic version, the MCT predicts a glass transition of hard spheres at a volume fraction of $\Phi = 0.525$, significantly smaller than the experimentally observed value of $\Phi \approx 0.58$ [van Megen 1994]. A phenomenological correction can be applied of rescaling the volume fraction as $\Phi \to \Phi(\Phi_g/0.525)$, with Φ_g determined so that the theory reproduces Brownian

dynamics simulation results at high volume fractions, that is $\Phi_g = 0.62$ – this time a value larger than experimentally observed [Banchio 1999a]. The predictions of MCT have been compared with experimental results (DLS) giving good quantitative agreement at a large range of volume fractions and times probed [van Megen 1994, Banchio 1999a, van Megen 2007b]. This, as well as the general difficulty of accurate determination of a transition point from first principles [Götze 1999], are good arguments which can justify the above described Φ_g scaling procedure.

Résumé du Chapitre 4

Ce chapitre montre comment l'information à propos de la dynamique et du profil de vitesse d'une suspension colloïdale diluée en écoulement peut être obtenue via une étude par XPCS (résultats publiés dans [Fluerasu 2010]). L'expérience rapportée ici est un développement de la méthode présentée dans [Fluerasu 2010, Busch 2008]. Elle montre que dans certaines conditions, il est possible d'extraire la composante diffusive de la dynamique des particule en supension dans un fluide sous cisaillement. Le chapitre présente tout d'abord l'influence de l'écoulement sur les signaux obtenus en XPCS. Les temps de corrélation mesurés dans un système en écoulement ne dépendent pas seulement de l'amplitude du vecteur diffusion, mais aussi de son orientation relative par rapport à la direction de l'écoulement. Les mesures décrites ici ont été effectuées dans une cellule d'écoulement simple, consistant en un canal cylindrique. Les faibles débits utilisés permettent d'obtenir un écoulement laminaire. Une bonne séparation des échelles de temps concernant l'advection et la diffusion a permis une mesure simultanée du coefficient de diffusion de Stokes-Einstein et du temps de relaxation lié au cisaillement.

Chapter 4

Dynamics of dilute colloidal suspensions under flow

Contents

This chapter presents how information about the dynamics and flow velocity profile can be obtained from an XPCS measurement of a dilute colloidal suspension under flow (results published in [Fluerasu 2010]).

The experiment reported here is a development of the method presented in [Fluerasu 2008, Busch 2008]. It demonstrates that under certain conditions it is possible to extract the diffusive component of the dynamics of particles suspended in a fluid undergoing shear flow. XPCS is used to measure both the diffusive and advective (flow induced) motion of the scatterers by taking the advantage of the anisotropy present in the correlation functions.

The chapter begins with an explanation of flow influence on the XPCS measurement. The correlation times measured in a flowing system depend not only on the magnitude of the scattering vector $q = |\vec{q}|$, but also on the relative orientation between the scattering vector and the flow direction.

4.1 XPCS under flow

Flow introduces two additional aspects to the movement of scatterers: relative velocity difference between scatterers at different locations and their transit through the scattering volume. Here the theory derived for visible light photon correlation spectroscopy in laminar flow in [Fuller 1980] is presented. It has been successfully applied to XPCS in [Busch 2008].

The following discussion is restricted to the simple case of non-interacting, spherical particles. In this dilute regime the static structure factor $S(q, 0) = 1$ and the cross terms in equation 2.12 ($n \neq m$) average to zero, simplifying the intermediate

scattering function to:

$$g_1(\vec{q},t) \propto \sum_{k=1}^{N} \langle E_k^*(0) E_k(t) \cdot \exp\left[i\vec{q}[\vec{r'}_k(0) - \vec{r'}_k(t)]\right]\rangle. \tag{4.1}$$

Particle displacement, included in the phase factor of the above equation, can be separated into terms describing diffusive and flow-related motion:

$$\exp\left[i\vec{q}\cdot\left(\vec{r'}_k(0) - \vec{r'}_k(t)\right)\right] = \\ \exp\left[i\vec{q}\cdot(\vec{r}_k(0) - \vec{r}_k(t))\right] \cdot \exp\left(i\vec{q}\cdot\vec{v}_0 t\right) \cdot \exp\left(i\vec{q}\cdot\delta\vec{v}t\right). \tag{4.2}$$

Here $\vec{r'}_k(t)$ – the k th particle position at time t in the presence of flow is separated into $\vec{r}_k(t)$ – position due to diffusion only, flow displacement due to $\vec{v}_0$ – average velocity throughout the sample and $\delta\vec{v}$ – the flow velocity difference of particle k between positions $\vec{r}_k(0)$ and $\vec{r}_k(t)$.

This simple consideration shows that the intermediate scattering function depends on three factors, characterized by the corresponding time scales: diffusive, with $\tau_D = 1/Dq^2$, D being the diffusion coefficient; amplitude, measuring the scattered intensity for each particle k, $I_k = \langle E_k^*(0) \cdot E_k(t)\rangle$, sensitive also to the transit time τ_T of particles through the scattering volume $\tau_T = L/v_0$, where L is the length scale characteristic for the scattering volume; and shear factor, with time scale τ_S, inversely proportional to the local flow velocity gradient $\dot{\gamma}$. It can be shown that [Fuller 1980]:

$$\tau_S \propto (q\dot{\gamma}L\cos\vartheta)^{-1}. \tag{4.3}$$

Here ϑ denotes the angle between the scattering vector $\vec{q}$ and the local velocity vector $\vec{v}$.

As derived in details in [Fuller 1980], assuming that the three time scales are well separated, the ISF can be written in terms of independent contributions from the relaxation mechanisms described above:

$$|g_1(\vec{q},t)| = |g_{1,D}(\vec{q},t)| \cdot |g_{1,T}(t)| \cdot |g_{1,S}(\vec{q},t)|. \tag{4.4}$$

The first factor, $g_{1,D}(\vec{q},t)$, accounts for the thermally driven diffusion, $g_{1,T}(t)$ describes the transit time through the scattering volume and $g_{1,S}(\vec{q},t)$ is related to shear. Their exact form will depend on the type of flow. Choosing for example a simple shear flow with a constant shear rate $\dot{\gamma}$, it can be shown [Ackerson 1981] that the diffusive part becomes anisotropic, with diffusion enhanced by the flow:

$$|g_{1,D}(\vec{q},t)|^2 = \left[-2Dq^2 t\left(1 - \frac{q_\parallel q_\perp}{q^2}\dot{\gamma}t + \frac{1}{3}\frac{q_\parallel^2}{q^2}(\dot{\gamma}t)^2\right)\right], \tag{4.5}$$

here $q_\parallel$ and $q_\perp$ denote the components of $\vec{q}$ parallel and perpendicular to the flow velocity (see figure 4.1). It should be noted that by choosing the scattering geometry so that $\vec{q} \perp \vec{v}$, the parallel component is equal to zero and equation 4.5 takes the

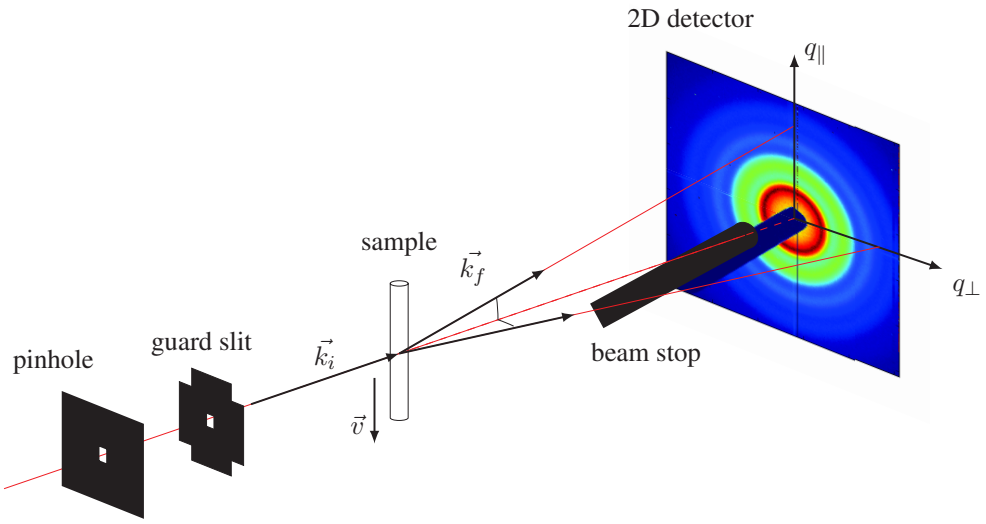

Figure 4.1: Schematic representation of an XPCS measurement under flow in SAXS geometry. The flow velocity $\vec{v}$ is oriented vertically, as marked by the arrow on the side of the sample cell. Direction of the scattering vector at which the measurement is taken may be chosen to be parallel ($q_\parallel$) or perpendicular ($q_\perp$) to flow velocity vector.

simple exponential decay form, identical to the case of non-interacting particles undergoing Brownian motion without flow:

$$|g_{1,D}(\vec{q},t)|^2 = \exp\left[-2Dq^2t\right] \tag{4.6}$$

Flow related transit of scatterers through the scattering volume leads to a decorrelation of the dynamic structure factor which can be characterized by a frequency $f_{tr} \propto v_0/h$. It has been shown ([Berne 2000]) that the contribution to the measured correlation function can be understood as the effect of flowing scatterers *scanning* the beam profile. In a typical XPCS experiment the beam is defined by rectangular slits, therefore the incident beam intensity profile has the shape of a $\left(\frac{\sin(r)}{r}\right)^2$ function (squared Fourier transform of a rectangle function). The usage of guard slits aligned to suppress higher-order diffraction peaks allows to approximate the intensity distribution at the sample as a Gaussian. This leads to the following simple form of the transit time contribution to the correlation function:

$$|g_{1,T}(t)|^2 \propto \exp\left[-(f_{tr}t)^2\right] \tag{4.7}$$

The above equation shows that this contribution does not depend on the scattering vector $\vec{q}$.

To understand the shear influence on the measured correlation functions it is convenient to consider a pair of particles moving with different velocities due to

presence of shear. Velocity difference $\delta\vec{v}$ will cause a Doppler shift in frequencies of radiation scattered from these particles. The induced self-beat frequency will be equal to $\vec{q}\cdot\delta\vec{v}$. Calculating the contribution from all particles in the scattering volume requires summing over all pairs of scatterers. Assuming small transverse beam size, the scattering volume can be approximated by a line of length $2R$, then the shear contribution to $g_1(\vec{q},t)$ is given by:

$$|g_{1,S}(\vec{q},t)|^2 = \frac{1}{4R^2}\int_{-R}^{R}\int_{-R}^{R}\cos\left(\vec{q}\cdot\delta\vec{v}(r_1,r_2)t\right)\mathrm{d}r_1\mathrm{d}r_2 \tag{4.8}$$

Analytical solution to the above integral has been performed for a uniform shear rate [Narayanan 1997], giving:

$$|g_{1,S}(\vec{q},t)|^2 = \frac{\sin\left(q_\parallel v_0 t\right)}{q_\parallel v_0 t} \tag{4.9}$$

A more complicated form of the solution has been found for the parabolic velocity profile (Poiseuille flow in a cylindrical channel) [Busch 2008]:

$$|g_{1,S}(\vec{q},t)|^2 = \frac{\pi^2}{16 q_\parallel t v_0}\left|\mathrm{erf}\left(\sqrt{\frac{4iq_\parallel t v_0}{\pi}}\right)\right|^2 \tag{4.10}$$

Another interesting flow geometry is the flow in a rectangular channel. In this case, the velocity profile can be described by a series of sine functions [Spiga 1994]:

$$u_x(y,z) = \sum_{n\ odd}^{\infty}\sum_{m\ odd}^{\infty} u_{nm}\sin\left(n\frac{\pi}{w}y\right)\sin\left(m\frac{\pi}{h}z\right) \tag{4.11}$$

with

$$u_{nm} = \frac{16}{\pi^4}\frac{\Delta p}{\eta L}\frac{1}{nm\left(\frac{n^2}{w^2}+\frac{m^2}{h^2}\right)}. \tag{4.12}$$

Here w is the channel width, h – height and L – length, as depicted in figure 4.2. Calculation of the integrals in equation 4.8 for this profile can be performed numerically. The result, compared to other velocity profiles, is presented in figure 4.3.

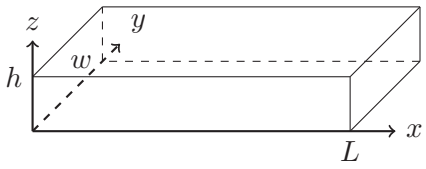

Figure 4.2: Geometry of the rectangular channel.

Equations 4.9 and 4.10 allow to define a shear-induced frequency as:

$$\Gamma_S = \vec{v_0}\cdot\vec{q}. \tag{4.13}$$

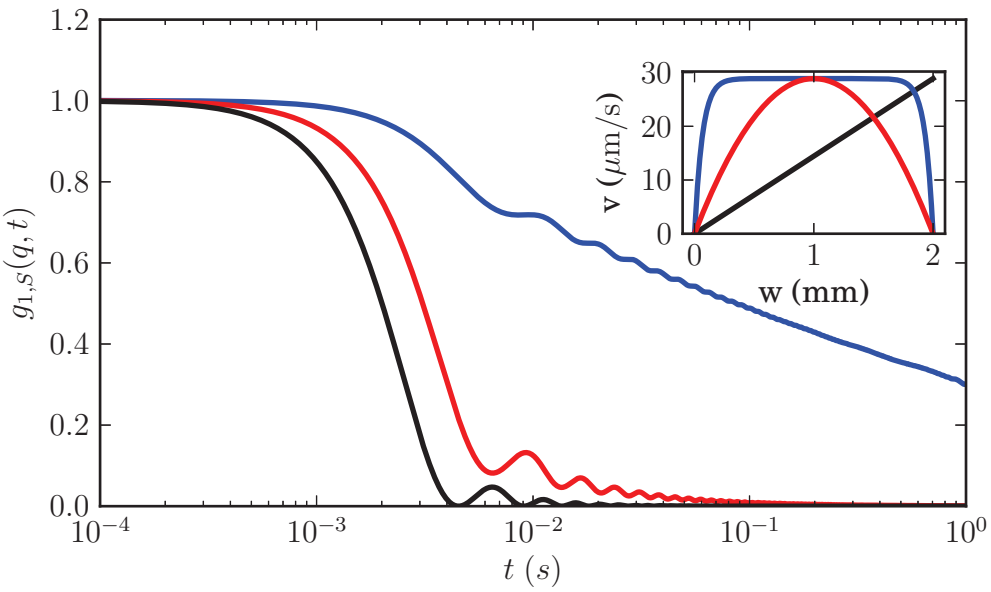

Figure 4.3: Comparison of shear contributions to the intermediate scattering function for different flow velocity profiles, calculated for $q = 2.4 \times 10^{-3}$ $\mathring{A}^{-1}$. The curves for simple shear (black) and parabolic profiles (red) where calculated analytically, by solving equations 4.9 and 4.10, respectively. The $g_{1,S}$ for rectangular channel velocity profile (blue) was calculated numerically. Corresponding velocity profiles are presented in the inset.

In case of perfectly transversal scattering alignment, that is $\vec{q} \perp \vec{v}$, $\Gamma_S = 0$, leaving the measured correlation functions unaffected by shear. It is worth emphasizing that the shear-related anisotropy of the coherent scattering pattern is related exclusively to the *dynamic* part, that is – the speckles. Due to shear the speckle fluctuation frequency increases when measured in $\vec{q} \parallel \vec{v}$. The static part, which can be retrieved by averaging the measured $I(\vec{q}, t)$ over time, remains isotropic.

4.2 Experimental setup

The flowcell used in this experiment was made out of a Kapton tube with inner radius $R = 0.66$ mm and ≈ 100 μm thick walls. Sample flow was provided by a syringe pump (Harvard Apparatus Inc.) with a Hamilton syringe, connected to the flowcell via PEEK^{TM}polymer tubes, leak-tight fittings and adapters, purchased from Upchurch Scientific.

Flow rates applied during the measurements were between $Q = 0$ and 80 $\mu l/h$. These values can be translated into average flow velocities, $v_0 = Q/\pi R^2$, giving $0 < v_0 < 16$ μm/s. Reynold's number calculated for the above parameters using

$Re = 2Rv_0\rho/\eta$, where ρ is the density and η the dynamic viscosity of PG, has a value $Re < 10^{-6}$. Under these conditions the flow in the tube can be considered laminar, with the velocity profile described by a parabola:

$$v(r) = 2v_0\frac{R^2 - r^2}{R^2}. \tag{4.14}$$

4.3 Results

4.3.1 Free diffusion coefficient measured under flow

The free diffusion coefficient D_0 was determined by fitting the transverse flow correlation functions to simple exponentials. The results are shown in figure 4.4. In the low-flow limit D_0 is, as expected, independent of both q and the flow rate. At higher flow rates ($Q > 40\mu l/h$) the correlation functions (shown in the inset) start deviating from single-exponential (straight lines in the lin-log representation) and the fitted correlation times shift towards faster values due to the increasing longitudinal components of the flow velocity. These components are present because of the finite widths of the detector regions over which $g_2(q,t)$ are ensemble averaged. The value obtained from the simple exponential fits for D_0 is 2.25×10^6 $\mathring{A}^2/s$. The viscosity was determined using the Einstein-Stokes relationship,

$$D_0 = \frac{k_B T}{6\pi\eta R} \tag{4.15}$$

yielding $\eta = 38 \pm 1$ $mPa\ s$ at room temperature – a value in fair agreement with the tabulated one [Lide 2010] for PG, $\eta = 40.4 \pm 0.4$ $Pa\ s$ (at 25 °C). The difference probably comes from a small amount of residual water present in the solvent.

4.3.2 Shear-induced relaxation time

The speckle contrast β and the baseline value g_∞ of the measured correlation functions were first obtained from fits with stretched exponentials following the Kohlrausch-Williams-Watts (KWW) form:

$$\beta \exp\left[(2\Gamma t)^\gamma\right] + g_\infty. \tag{4.16}$$

The γ parameter in this formula allows to stretch (or compress) the exponential decay to fit the data well, although in this case it carries no physical meaning – it is used simply as the initial step for further data analysis. Subsequently, the normalized correlation functions $g_2^{\text{norm}} = (g_2 - g_\infty)/\beta$ were fitted using equation 4.4, with the value measured for D_0 kept constant. Examples of fits for normalized correlation functions measured in transverse flow (blue circles) and longitudinal flow (red triangles) geometries, for a single value of the scattering wave vector $q = 2.8 \times 10^{-3}$ $\mathring{A}^{-1}$ and a single position in the flowcell (at the center, $x/R = 0$) at different flow rates $Q = 20 - 80\mu l/h$, are shown in figure 4.5. The position

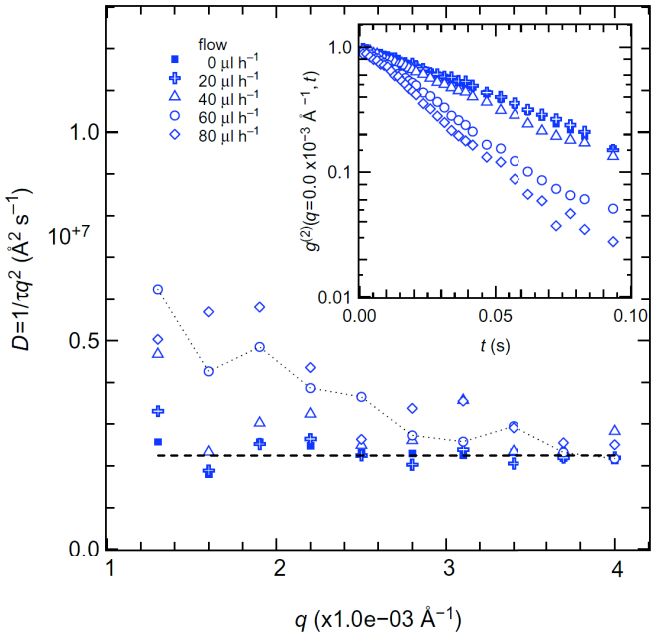

Figure 4.4: Free diffusion coefficient obtained from single exponential fits of the transverse flow correlation functions shown in the inset for a single value of $q = 2.5 \times 10^{-3}$ $\mathring{A}^{-1}$. In the low-flow limit (< 40 $\mu l/h$) the correlation times (τ) are independent of the flow rate and τq^2 are *q-independent* and equal to the inverse of the free diffusion coefficient $D_0 \approx 2.2 \times 10^6 \mathring{A}^2/s$.

dependence of the correlation functions for the same value of q, a single flow rate $Q = 40\mu l/h$ and the same scattering geometries is displayed in figure 4.6.

The fits show that the very simple model used here, assuming a parabolic-shaped Poiseuille flow and hence an exact form for $g_2(\vec{q}, t)$, describes the experimental data remarkably well. The most significant fitting parameter here is the shear-induced relaxation rate, $\Gamma_S = \vec{q} \cdot \vec{v}$, where $\vec{v}$ is the maximum flow velocity along the direction of the beam (y). Since this is obtained at different positions across the flow tube (x), the fitted values also depend on x: $\Gamma_S(x) = q \cdot v(x)$. Here, we omit the vectorial notation and the dot product because only values measured from longitudinal flow fits are used. The x-dependence of the maximum flow velocity along the y-direction in a Poiseuille-flow geometry is easily obtained from equation 4.14, and we obtain:

$$\Gamma_S(x) \propto \frac{qQ}{\pi R^2} \left(1 - \frac{x^2}{R^2}\right). \tag{4.17}$$

Fits with equation 4.17 for the shear-induced relaxation rates obtained from the fits at different locations in the flow tube are shown in figure 4.7(a). The data shown here were measured at four different flow rates and two different values of q.

From equation 4.17 one can also see that a scaled relaxation rate

$$\gamma_S = \frac{\Gamma_S}{qQ/\pi R^2} \propto 1 - \left(\frac{x}{R}\right)^2 \tag{4.18}$$

should follow a single, flow- and q-independent parabolic profile across the tube (figure 4.7(b)).

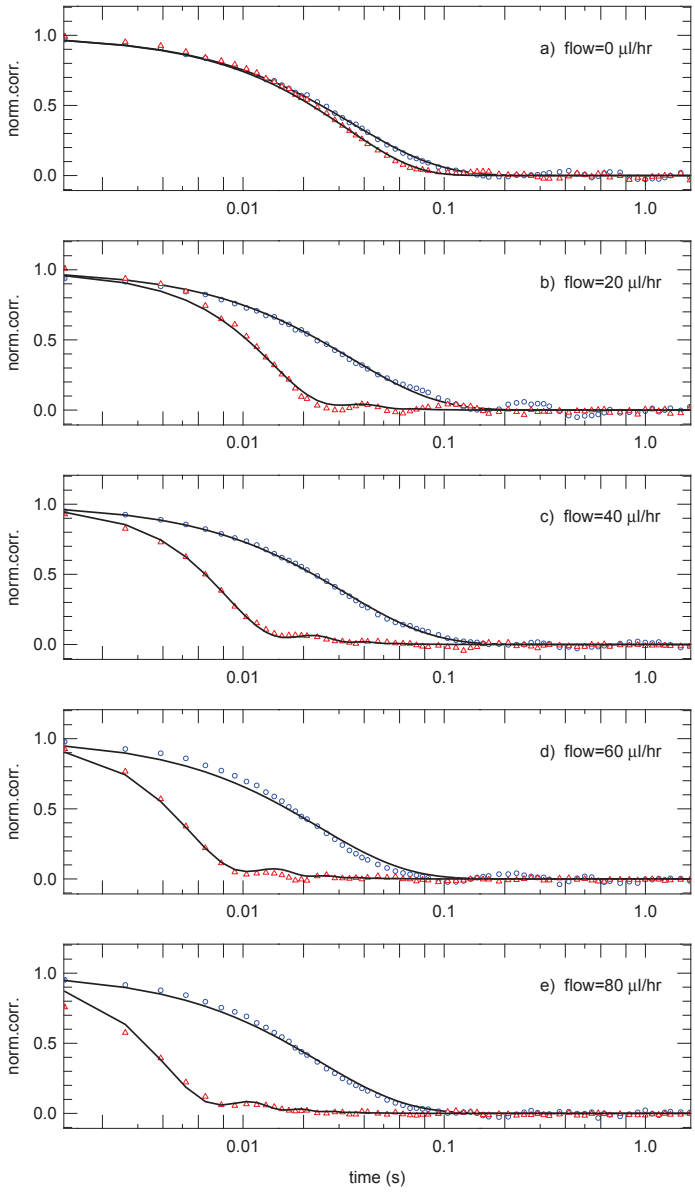

Figure 4.5: Normalized correlation functions and fits for $q = 2.8 \times 10^{-3} \mathring{A}^{-1}$ and $x/R = 0$ (center of the flowcell) measured at different flow rates: Q = 0-80 $\mu l/h$ (a)-(e). Blue circles: transverse flow correlation functions, $q \perp$ flow. Red triangles: longitudinal flow, $q \parallel$ flow.

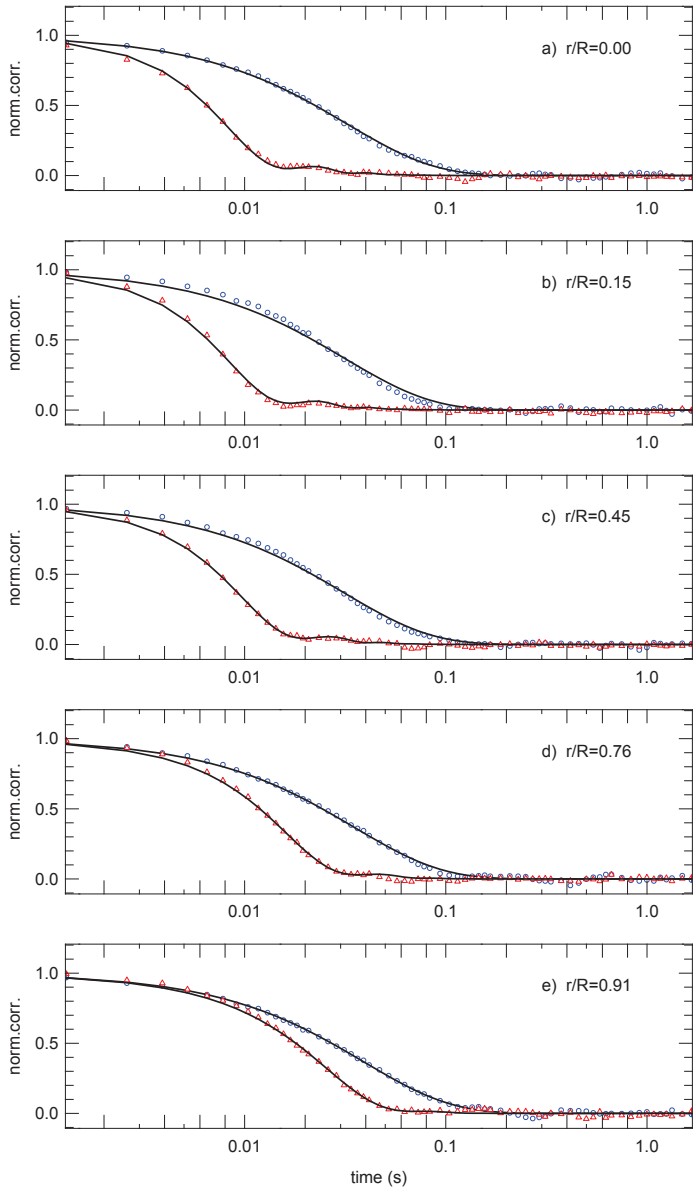

Figure 4.6: Normalized correlation functions and fits for $q = 2.8 \times 10^{-3} \mathring{A}^{-1}$ and $Q = 40\mu l/h$ measured at different locations across the flowcell x/R = 0-0.91 (a)--(e). Blue circles: transverse flow correlation functions, $q \perp$ flow. Red triangles: longitudinal flow, $q \parallel$ flow.

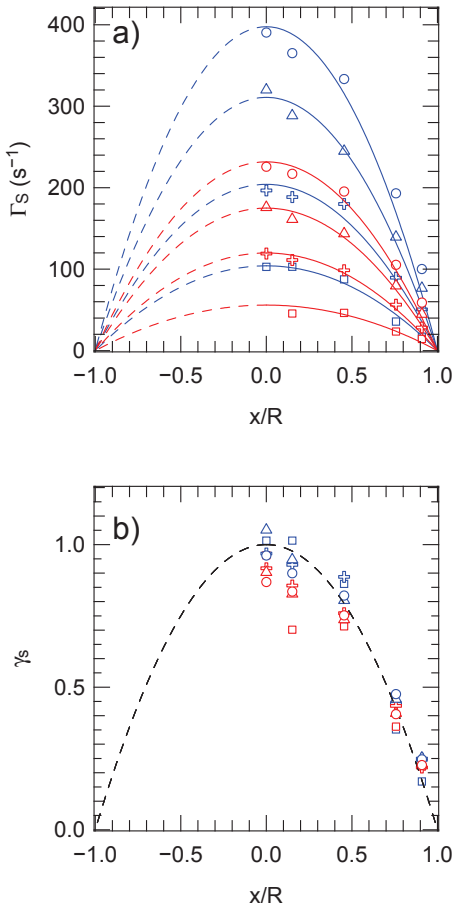

Figure 4.7: (a) Fitted shear-induced relaxation as a function of position (x/R) for four different flow rates: 20 $\mu l/h$ (squares), 40 $\mu l/h$ (crosses), 60 $\mu l/h$ (triangles) and 80 $\mu l/h$ (circles) - and two values of q: 1.6×10^{-3} $\mathring{A}^{-1}$ (blue) and 2.5×10^{-3} $\mathring{A}^{-1}$ (red). The solid lines show fits with a parabolic profile; the dashed lines (extension to negative values of x) are guides to the eye. (b) Scaled relaxation rates (γ_s) for the same values of the flow rate Q and wave vector q collapse on a single parabolic profile across the tube.

Résumé du Chapitre 5

La dynamique des colloïdes à forte fraction volumique fait l'objet de recherches poussées. L'intérêt n'est pas que fondamental: ce type de système est très présent dans des applications industrielles.

Ce chapitre commence par un rappel des propriétés dynamiques des colloïdes concentrés, suivi par une description des procédures d'acquisition et de traitement de données. Les résultats expérimentaux sont ensuite discutés, en commençant par la détermination de la fraction volumique qui se fait via des ajustements de profils d'intensité radiale de systèmes modèles de sphères dures, moyennés axialement et dans le temps.

Les fonctions de diffusion intermédiaires obtenues à partir de mesures de XPCS effectuées sur plusieurs tavelures ("multi-speckles") sont analysées dans les limites des temps longs et des temps courts. Une procédure numérique est utilisée pour déterminer la fin du comportement de diffusion aux temps courts. La comparaison de ce temps avec le temps moyen entre deux collisions de particules permet de conclure que le comportement diffusif aux temps courts est perdu en quelques collisions. L'analyse de la fonction hydrodynamique, à des fractions volumiques plus faibles qui décrivent l'influence des interactions indirectes médiées par le liquide environnant, indique également une influence non négligeable des interactions directes entre particules même dans la limite des temps courts.

Une relation exponentielle entre l'inverse du coefficient de diffusion et la fraction volumique a été mise en évidence pour $\Phi > 0.5$. Cette relation est bien reproduite avec la formule de Vogel-Fulcher-Tammann, ce qui laisse supposer qu'on a affaire à un blocage cinétique ("jamming") plutôt qu'à une transition vitreuse. Mais les prédictions de la théorie du couplage de modes, qui correspondait bien aux résultats expérimentaux pour les suspensions diluées, ne permet pas de rendre compte de la dépendance en fraction volumique des coefficients de diffusion, ni pour les temps longs ni pour les temps courts.

Nous avons néanmoins effectué un test sur le comportement d'échelle de la fonction de diffusion intermédiaire. Il avait été précédemment montré que le tracé de $\ln\left[g1(q,t)\right]/D_S(q)q^2$ en fonction du temps se réduit à une courbe maîtresse pour une large gamme de valeurs de q [Segrè 1996]. Les résultats présentés dans cette thèse montrent que ceci n'est plus valable dans la gamme de fractions volumiques étudiée ($0.5 < \Phi < 0.6$).

Une étude plus détaillée des fonctions de corrélation mesurées sur l'échantillon le plus concentré (Φ=0.597) révèle une décroissance plus rapide qu'exponentielle dans le régime des temps longs, sans signe d'hétérogénéité dynamique. Cette observation elle aussi est cohérente avec un scénario de blocage cinétique pour expliquer le ralentissement de la dynamique. Le processus de vieillissement est observé via les fonctions de corrélation à deux temps. Une dynamique complexe, non stationnaire, est mise en évidence. Ce comportement n'est pas accessible aux fonctions de

corrélation moyennées dans le temps qui sont couramment utilisées dans ce type d'études. Une analyse qualitative des fonctions de corrélation à deux temps montre que la dynamique est affectée à toutes les échelles de temps et de longueur par des événements de type avalanche. Une analyse plus quantitative nécessite d'être développée pour aller plus loin dans cette compréhension.

Chapter 5

Dynamics of concentrated colloidal suspensions

Contents

5.1 Introduction

In colloidal suspensions at high volume fractions (close to $\Phi = 0.5$) the static structure factor shows a pronounced peak at $2\pi/q \approx 2R$, R being the particle radius, which is explained as the effect of short-range ordering (formation of a cage) of particles surrounding a chosen particle [Pusey 1997]. As previously discussed in section 3.3, the dynamics is influenced by their interactions, both direct and solvent-mediated hydrodynamic interactions (HI). Two experimentally relevant time scales can be distinguished: the short-time diffusive limit for $\tau_B \ll t < \tau_R$, and the long-time limit for $t > \tau_R$. At longer times than the Brownian relaxation time τ_B (equation 3.13) a diffusive description of particle motion is justified. Also, the motion of a particle suspended in a liquid induces a velocity field, which propagates on time a scale $\tau_H \sim \tau_B$ and influences the motion of other particles. The structural relaxation time τ_R (equation 3.15) is defined as the time needed for a free particle to displace by a distance equal to its radius. At times longer than τ_R interparticle collisions are considered significant, further complicating the dynamics [Pusey 1991, Zhang 2006].

The slowing down of the diffusion due to HI is taken into account via the short-time diffusion coefficient $D_S(q) < D_0$, which can be probed in a photon correlation experiment by measuring the intermediate scattering function in the appropriate time scale:

$$g_1(q, t < \tau_R) = \exp\left[-D_S(q)q^2 t\right]. \tag{5.1}$$

The influence of HI is represented by the hydrodynamic function:

$$D_S(q) = D_0 \frac{H(q)}{S(q)}. \tag{5.2}$$

A comprehensive theory of short-time dynamics in concentrated suspensions of hard spheres including hydrodynamic interactions was developed by Beenakker and Mazur [Beenakker 1983, Beenakker 1984]. It has been demonstrated to be in agreement with experimental results up to volume fractions $\Phi \sim 0.4$ [Segrè 1995a, Orsi 2012b]. At higher concentrations (up to the freezing transition at $\Phi = 0.494$) the rescaled MCT [Banchio 1999b] proved to represent the Φ dependence of the $H(q)$ peak value better, both for experimental and simulation results [Banchio 2008, Orsi 2012b].

The long-time dynamics can be characterized by a second, slower, approximately exponential decay:

$$g_1(q,t) \propto \exp\left[-D_L(q)q^2 t\right], \tag{5.3}$$

with the q-dependent long-time diffusion coefficient $D_L(q) < D_S(q)$, characterizing the jumps between cages or the dissolution of cages which occur after large structural rearrangements. The theory of dynamics at these time scales is more complex, since it requires including direct particle interactions. Approximate treatments were developed by Medina-Noyola [Medina-Noyola 1988] and Tokuyama and Oppenheim [Tokuyama 1995].

By analogy to molecular systems with the same interaction potential, the dynamics of hard-sphere suspensions can be treated with the formalism of the mode-coupling theory [Götze 1991] and the β and α relaxations, corresponding to short- and long-time regimes, respectively. In this picture particle caging leads to a dynamic arrest (glass transition), characterized by the algebraic divergence of the ergodicity restoring α relaxation time at the glass transition volume fraction Φ_g:

$$\tau_\alpha \propto (\Phi_g - \Phi)^{-\gamma}. \tag{5.4}$$

Predictions of the MCT have been shown to reproduce well numerous experimental results [van Megen 1994, Fuchs 1999, Götze 1999]. Hydrodynamic interactions, which are not taken into account in the basic version of the theory, can be included by empirical scaling procedures [Banchio 1999a].

This chapter presents the results of dynamics measurements performed on suspensions of PMMA particles, described in more details in section 3.2.2. The probed volume fraction range is above the hard-sphere freezing point ($\Phi = 0.494$). Colloidal crystal growth is suppressed within the experimentally relevant time due to particle size polydispersity, allowing for unperturbed measurement of the samples in the "supercooled" fluid state. The use of multi-speckle XPCS technique to probe the dynamic properties of the colloids allows to address several interesting problems. Both structure and dynamics can be probed over a wide q range. This is difficult to achieve with visible light scattering techniques, typically used in such studies. The time range probed gives access to both short- and long-time

dynamic regimes. The short-time limit allows to study the influence of hydrodynamic interactions at volume fractions higher than previously reported (see e.g. [Segrè 1995a, Phan 1996, Orsi 2012b]). Dynamics in the long-time limit which is more challenging both from an experimental and a theoretical point of view, is also interesting. The complexity of interparticle interactions limits any theoretical predictions beyond simple approximations. Examples of different experimental results on similar systems can also be found, e.g. in [van Megen 1998] and [Brambilla 2009]. Both works investigate the dynamics of a hard-sphere suspension similar to the one used in this thesis. The authors of [van Megen 1998] found quantitative agreement with predictions of the scaled MCT, with a clear glass transition at $\Phi_g \approx 0.57$, where the long-time relaxation diverged. On the contrary, Brambilla *et al.* report strong deviations from the MCT model, including ergodic behaviour at $\Phi > 0.59$. This observation rather supports a scenario where the free volume is responsible for kinetic arrest at $\Phi \approx \Phi_{RCP}$, which is the random close packing volume fraction.

5.2 Data acquisition and processing

The samples at high packing fractions display a sufficiently slow dynamics for multi-speckle XPCS with the MAXIPIX detector to be used. The highest possible frame rate was $\approx$ 1 kHz and for each measurement a series of 10000 scattering patterns was recorded. This gives approximately 13 s of sample exposure to X-rays, including 3 ms dead-time of the detector. To minimize the possible influence of radiation damage, the sample was moved to a fresh spot before repeating the measurement.

Determination of whether the static structure of the sample evolves during acquisition time can be done by time- and azimuthal-averaging of the scattering patterns. For this purpose the frames are grouped into 10 bins, containing 1000 images each. Next, averaging is performed over all images in each bin, giving 10 static scattering curves, as presented in figure 5.1. Each curve is labelled with the delay time between the beginning of the measurement and the acquisition time of the center frame of the corresponding bin.

Before calculating the correlation functions, several preparative steps are taken in order to exclude bad data from the analysis. First, on the basis of a scattering pattern time-averaged over all acquired images a mask is prepared which allows to exclude the detector area covered by the beam stop as well as pixels that were strongly influenced by parasitic scattering from the beam defining pinhole, which can never be perfectly screened by the guard slits.

In a second step this mask is refined by analysing the intensity in single-pixel wide rings, corresponding to the same value of $|\vec{q}|$, which is expected to fluctuate around an angle-independent mean value. All pixels recording intensities above an arbitrary threshold of 3 times the standard deviation from the mean value $\pm 3\sigma$ are masked (see figure 5.2). This step also allows to detect a deviation of the assumed direct beam position on the detector from the real one. As seen in figure 5.3, even

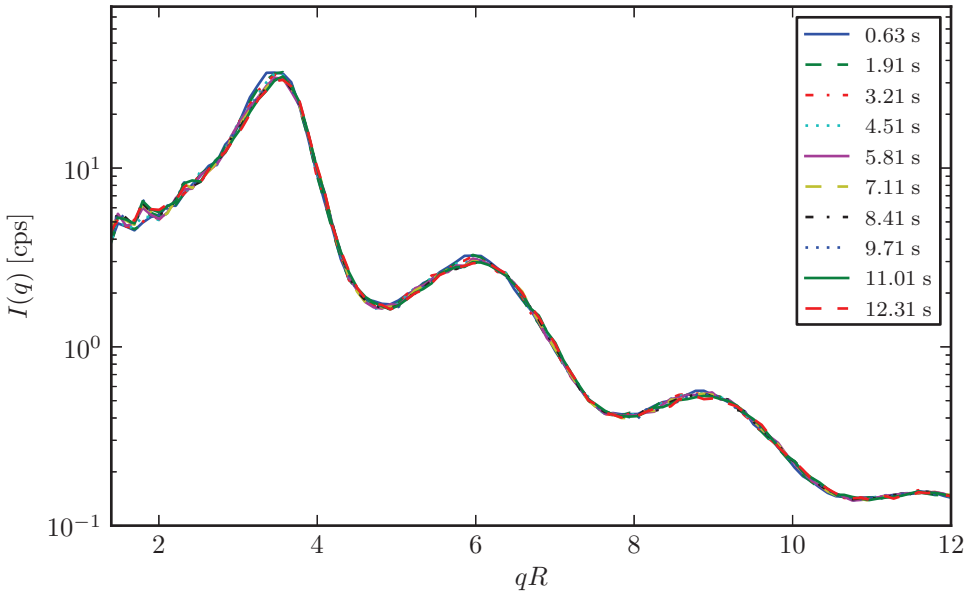

Figure 5.1: Time evolution of the time- and azimuthally-averaged scattered intensity calculated from a series of 2D speckle patterns used for XPCS. The resemblance between the curves indicate a stable structure during the measurement and hence there are no signs of beam damage.

a slightly mispositioned center results in clear angular dependence of the intensity fluctuations in one ring.

Further refinement of the mask is achieved by calculating the normalized variance of intensity in time. The same 3σ threshold is then applied to discard pixels, which display a too high variance value compared to the average calculated in a single-pixel wide, *iso*-$|\vec{q}|$ ring.

The intermediate scattering function g_1 is extracted from the measured correlation functions using the Siegert relationship (see section 2.3.1). Non-linear least-square fits of a stretched exponential form:

$$g_2(q,t) = \beta \exp\left[-2(\Gamma(q)t)^{\gamma}\right] + g_\infty \tag{5.5}$$

are used to obtain a first approximation of the experimental contrast β and the baseline value g_∞. Next, a simple exponential form is fitted only to the initial part of g_2 with a fixed value of g_∞, obtained from the first fit. This step is applied to refine the experimental contrast value and obtain the first estimate of the short-time diffusion coefficient. The two steps allow to calculate the intermediate scattering function as:

$$g_1(q,t) = \sqrt{\frac{1}{\beta}(g_2(q,t) - g_\infty)} \tag{5.6}$$

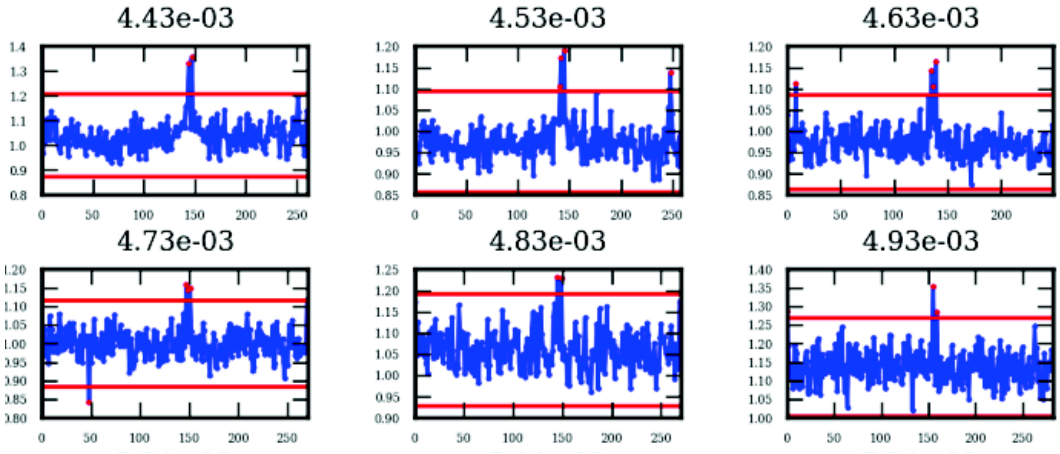

Figure 5.2: Intensity fluctuations in a chosen subset of single-pixel wide rings of the time-averaged scattering pattern. Horizontal red lines indicate the 3σ deviations from the mean levels. Pixels with intensity value above or below the 3σ value are excluded from further analysis.

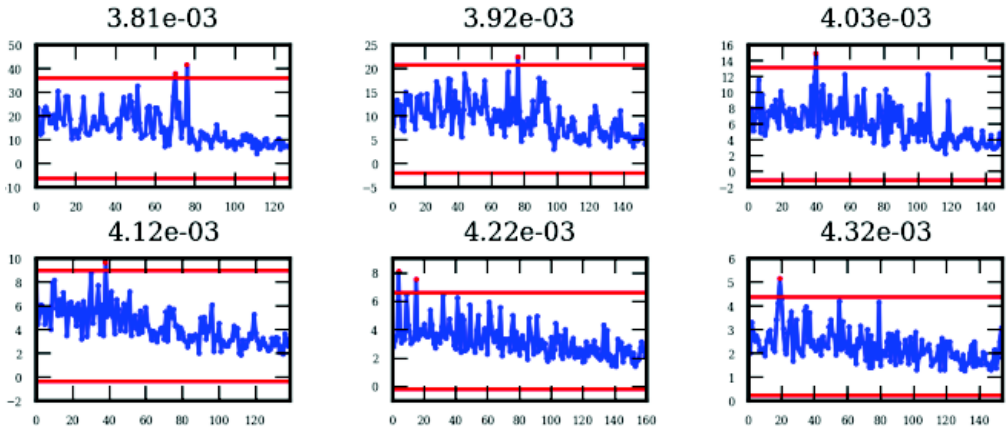

Figure 5.3: Intensity fluctuations in a chosen subset of single-pixel wide rings of the time-averaged scattering pattern calculated with a direct beam position deviated by one pixel from the real value.

5.3 Results and discussion

5.3.1 Sample characterization using static scattering

The particle volume fractions Φ for every sample were obtained from fitting the time- and azimuthally- averaged scattered intensity profile. The fitted model was the analytical solution for the scattering function of a polydisperse hard sphere fluid

in the Percus-Yevick approximation with a Schulz distribution of particle diameters, derived in [Griffith 1987] (see section 1.2.2). Instrumental resolution was taken into account by convolving the model function with a Gaussian distribution, calculated using the pixel size as the width parameter. Results are presented in the left panel of figure 5.4, with the fitted values of Φ indicated in the legend. The experimental

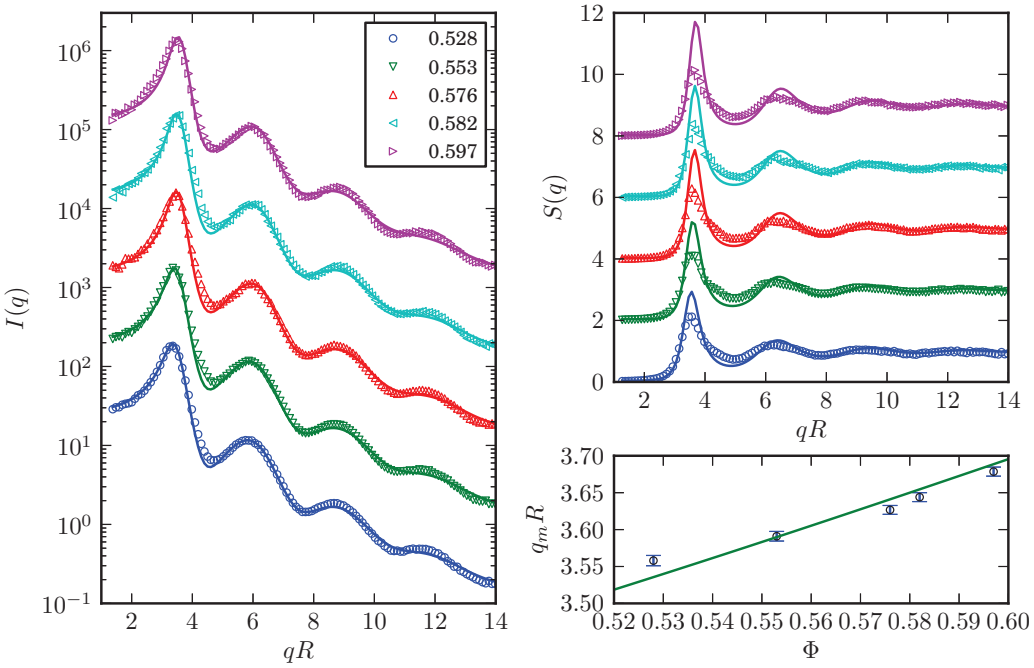

Figure 5.4: The left panel shows fits of the time- and azimuthally- averaged scattered intensity profiles using the analytical solution for the scattering function of a polydisperse Percus-Yevick fluid with Schulz distribution of particle diameters. Detector resolution (pixel size) has been taken into account by convolution of the model with a Gaussian. Symbols represent the experimental data, the fits are marked with solid lines. All curves have been shifted for clarity. The fitted volume fractions Φ are indicated in the legend. The upper right panel presents "experimental" structure factors, determined as $S(q) = I(q)/P(q)$, where the form factor $P(q)$ has been obtained from SAXS measurements of a highly dilute suspension (see figure 3.2 a). The lower right panel is a plot of the experimental $S(q)$ peak position (symbols) and the theoretical $S(q)$ peak position vs volume fraction Φ.

structure factor $S(q)$, shown in the right upper panel of figure 5.4, was calculated assuming that

$$I(q) \propto P(q) \cdot S(q) \tag{5.7}$$

where the data set presented in figure 3.2a was taken as the experimental form factor $P(q)$. Solid lines in the $S(q)$ plot were calculated using values for particle radius,

polydispersity and Φ obtained from $I(q)$ fits. The highly overestimated value of the $S(q)$ peak is a sign of limited validity of the factorization applied [Chen 1986].

An important argument for the agreement between the experimental $S(q)$ and the hard sphere model is presented in the lower right panel of figure 5.4, which shows the first peak position (as $q_m R$) as a function of volume fraction. The symbols mark the values extracted from the data by fitting a Gaussian function to the first peak of $S(q)$ and taking the mean of the distribution. Error bars correspond to 2σ, where σ is the standard deviation from the mean. The solid line is extracted from the model $S(q)$ for hard spheres [Griffith 1986]. Fair agreement of the first $S(q)$ peak position extracted from the data with the hard sphere model, as well as a good fit of the model at higher q values justify the hypothesis of detector resolution and, mainly, the limited validity of the factorization expressed by equation 5.7 being responsible for the experimental $S(q)$ peak height not following the model.

5.3.2 Short- and long-time dynamics

The validation of the presence and identification of the exact range of the short- and long-time diffusive regions can be done by calculating a time-dependent diffusion coefficient, as shown with DLS data in [Segrè 1996, Martinez 2011]:

$$D(q,t) = -\frac{1}{q^2}\frac{\mathrm{d}\ln\left[g_1(q,t)\right]}{\mathrm{d}t} \tag{5.8}$$

On a plot of $D(q,t)$ as a function of time, diffusive regions would appear as plateaus. Since equation 5.8 requires numerical differentiation, the result can be noisy, even in the case of low noise DLS data. With XPCS and correlation functions calculated from 2D detector data using the multi tau algorithm, the analysis of $D(q,t)$ becomes challenging, due to the non-linear spacing of data points, which introduces jumps in the derivative of $g_1(q,t)$. A different approach can be taken, using the so called width function, defined analogically to the mean squared displacement [Martinez 2008]:

$$w(q,t) = -\frac{\ln\left[g_1(q,t)\right]}{q^2} \tag{5.9}$$

By substituting the intermediate scattering function with the form including a generalized diffusion coefficient we obtain:

$$g_1 = \exp\left[-D(q)q^2 t\right] \tag{5.10}$$

we obtain from equation 5.9:

$$w(q,t) = D(q)t \tag{5.11}$$

It is particularly useful to present the width function in log-log representation, since:

$$\log\left[w(q,t)\right] = \log\left[D(q)t\right] = \log\left[D(q)\right] + \log\left(t\right) \tag{5.12}$$

This means that in case of diffusive dynamics, the plot of $\log\left[w(q,t)\right]$ vs $\log\left(t\right)$ would place the data points on lines with slope 1, intersecting the $\log\left(t\right) = 0$ line at value equal to $\log\left[D(q)\right]$.

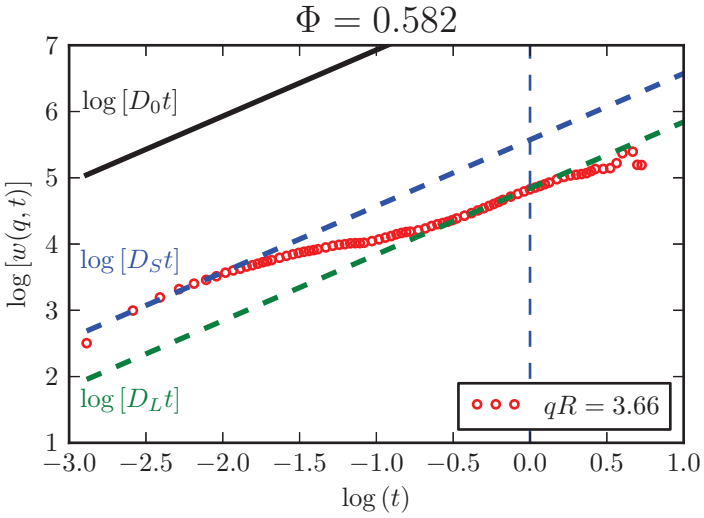

Figure 5.5: Logarithm of the width function plotted for a single volume fraction and qR value indicated.

Figure 5.5 presents an example of the width function calculated for a sample at $\Phi = 0.582$. The dashed lines show the fitted values of $\log[D_S t]$ and $\log[D_L t]$. The black solid line marks the free diffusion coefficient – $\log[D_0 t]$, obtained from DLS measurements of a highly diluted sample. A significant difference between D_0 and $D_S(q)$ illustrates the strong influence of hydrodynamic interactions on the dynamics. The obvious advantage of this data representation is that both the short- and long-time regimes can be illustrated without the need of rescaling the time axis.

The width functions at qR near the structure factor peak are presented in figure 5.6 for all volume fractions. As expected, the increase of particle packing results in slowing down of the dynamics and a more pronounced separation between the two diffusion coefficients. The presence of two diffusive time scales is shown well in the left panel of figure 5.7, where the fitted values of $D_S(q)$ and $D_L(q)$ are used to plot the dashed lines corresponding to $\log[D_S(q)t]$ and $\log[D_L(q)t]$ for the same qR value as in figure 5.6. The curves in figure 5.7 are separated for clarity by subtracting a constant. The linear fits were done on the appropriate regions of $w(q,t)$ with only one free parameter – the slope, which in the logarithmic representation is transformed into the intercept with the ordinate axis. For comparison, the right panel of figure 5.7 shows the data and fits for a qR value away from the $S(q)$ peak. While in the short-time limit, the data remain well fitted by the straight lines, indicating diffusive behaviour, the presence of long-time diffusive region can be determined only in the case of most concentrated sample. A similar observation was made in [Martinez 2011]. There, the authors were unable to unambiguously identify a long-time diffusive region away from the structure factor peak. However, the volume fractions investigated in this thesis go above the ones used in the work

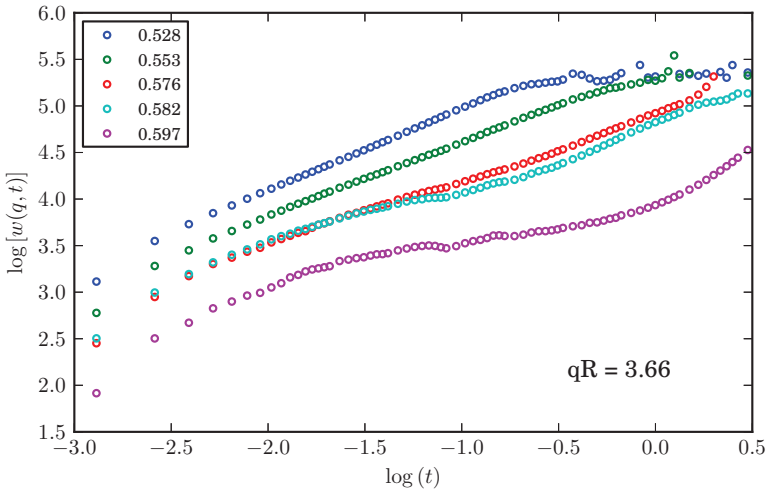

Figure 5.6: Logarithm of the width function plotted for volume fractions and qR value indicated. The relative volume fractions of the samples are well resolved, with both the static fits (values indicated in the legend) and the slowing down of the dynamics (especially in the long-time limit) giving the same order of samples in terms of Φ.

of Martinez and co-workers, where the most concentrated sample was $\Phi = 0.549$.

For a more quantitative evaluation of the end of short- and beginning of long--time diffusive regions, a simple numerical procedure has been applied, illustrated in figure 5.8. First, the absolute difference between the fitted value of $\log[D_S(q)t]$, $\log[D_L(q)t]$ and $\log[w(q,t)]$ was calculated:

$$\begin{aligned} \delta D_S &= |\log[D_S(q)t] - \log[w(q,t)]| \\ \delta D_L &= |\log[D_L(q)t] - \log[w(q,t)]| \end{aligned} \tag{5.13}$$

The values of δD_S and δD_L are shown as dotted lines in figure 5.8. Next, linear fits were performed on two regions of each of the curves – the time independent part was fitted with a constant ($y = b$) and the initial part of the slope with a linear form ($y = ax + b$). The cross points of the two lines are taken as the end of short-time diffusive region (t_S), extracted from δD_S, and the beginning of long-time diffusion (t_L) from δD_L. Additionally, the crossing point of δD_S and δD_L has been found and marked as t_m. It is expected to correspond to the inflection point of the $\log[w(q,t)]$ curve, which in this case is difficult to identify from numerical derivative for reasons explained earlier. All the characteristic times for $qR = 3.66$ (near the principal peak of $S(q)$) and the different volume fractions probed are collected in table 5.1.

A diffusive behaviour is expected to persist as long as the particles do not interact directly with each other. Having this in mind it is interesting to compare the experimentally observed value t_S to the average time between particle encounters

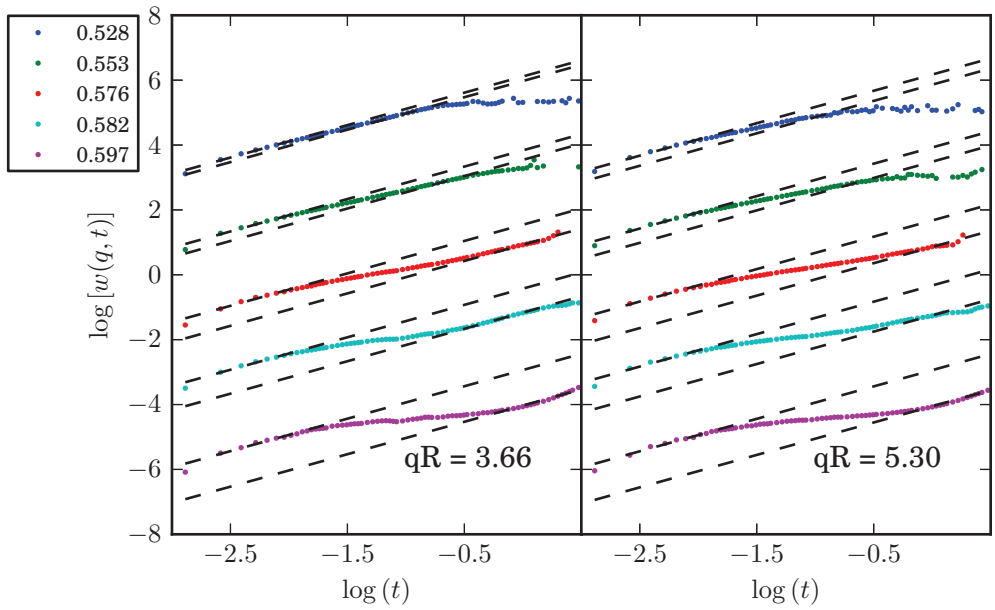

Figure 5.7: Logarithm of the width function plotted for volume fractions and two values of qR – near the $S(q)$ peak (left panel) and away from it (right panel). While near the $S(q)$ peak both diffusive regions are well pronounced at all volume fractions probed, at higher values of q long-time diffusive behaviour can be distinguished clearly only at the highest concentrations.

τ_c, which can be estimated from the average gap between particles R_c at a given volume fraction [van Megen 2005]

$$R_c = \left(\frac{\Phi_R}{\Phi}\right)^{1/3} - 1. \tag{5.14}$$

Here it is assumed that the particles are in contact at the random close packing concentration $\Phi_R = 0.67$ [Schaertl 1994]. The value of R_c calculated from equation 5.14 is given in units relative to the particle radius. Assuming diffusive dynamics, the average time between collisions can now be calculated from the experimentally determined short-time diffusion coefficient as:

$$\tau_c = \frac{R_c^2}{6D_S}. \tag{5.15}$$

The results of these calculations are also presented in table 5.1. Surprisingly, t_S is approximately one order of magnitude larger than τ_c and the ratio t_S/τ_c can be taken as a measure of the average number of collisions before the short-time diffusive character of the dynamics is lost. This suggests that the diffusive behaviour of the measured intermediate scattering function (ISF) is lost only after several collisions between particles have taken place, and not just after the first encounter.

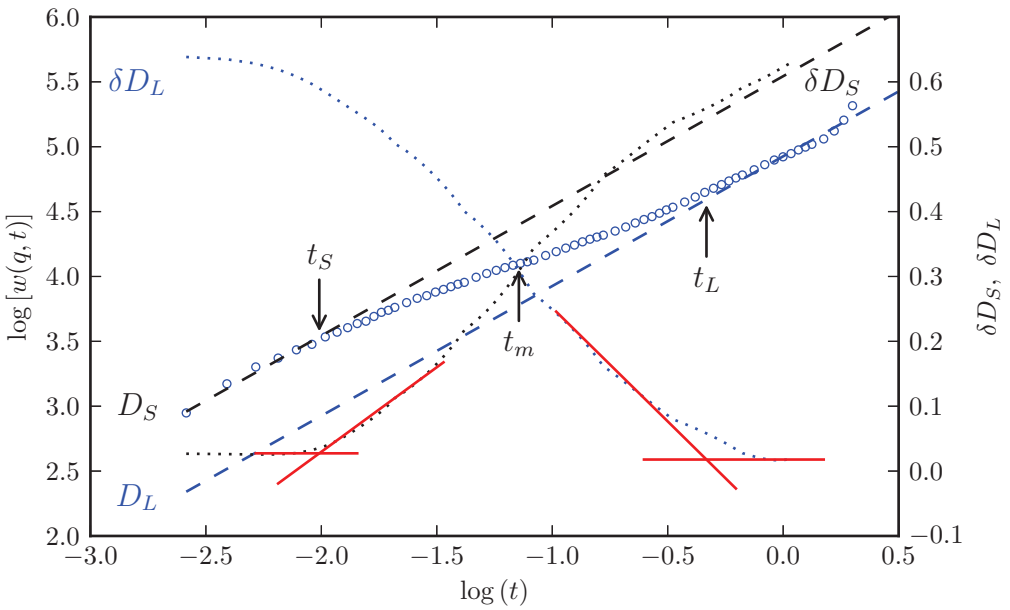

Figure 5.8: Illustration of the procedure identifying the limits of short- and long-time diffusive regions.

An inverse approach can also be applied by calculating the square root of the mean squared displacement associated with the time t_S:

$$R_S = \frac{\sqrt{6 D_S t_S}}{R}. \tag{5.16}$$

A comparison to R_c (see table 5.1) leads to the same conclusion – the average distance travelled by a particle before the dynamics looses diffusive character is larger than the separation between particles.

Additionally, the measured t_S shows no clear volume fraction dependence, as can be seen in figure 5.10, while τ_c is by definition Φ dependent. The value of t_S is remarkably close to the structural relaxation time defined by $\tau_R = R^2/D_0 = 12$ ms, which is commonly accepted as the time after which direct particle interactions cannot be neglected [Pusey 1991].

As the diffusive regime is clearly identified at short times, the $D_S(q)$ extracted from fits of the width functions has been used to calculate the hydrodynamic function $H(q)$ from equation 5.2, as the input structure factor using the analytically solved Percus-Yevick approximation including Schulz size distribution [Griffith 1986]. The model function for $S(q)$ was used to calculate the $H(q)$ instead of the experimental structure factor. The result is presented in figure 5.11, which, in addition to data for samples at $\Phi > 0.5$ includes a lower concentration sample at $\Phi = 0.466$ measured with a point detector. The values of $H(q)$ become much smaller for the more concentrated samples. For hard-sphere suspensions up to the

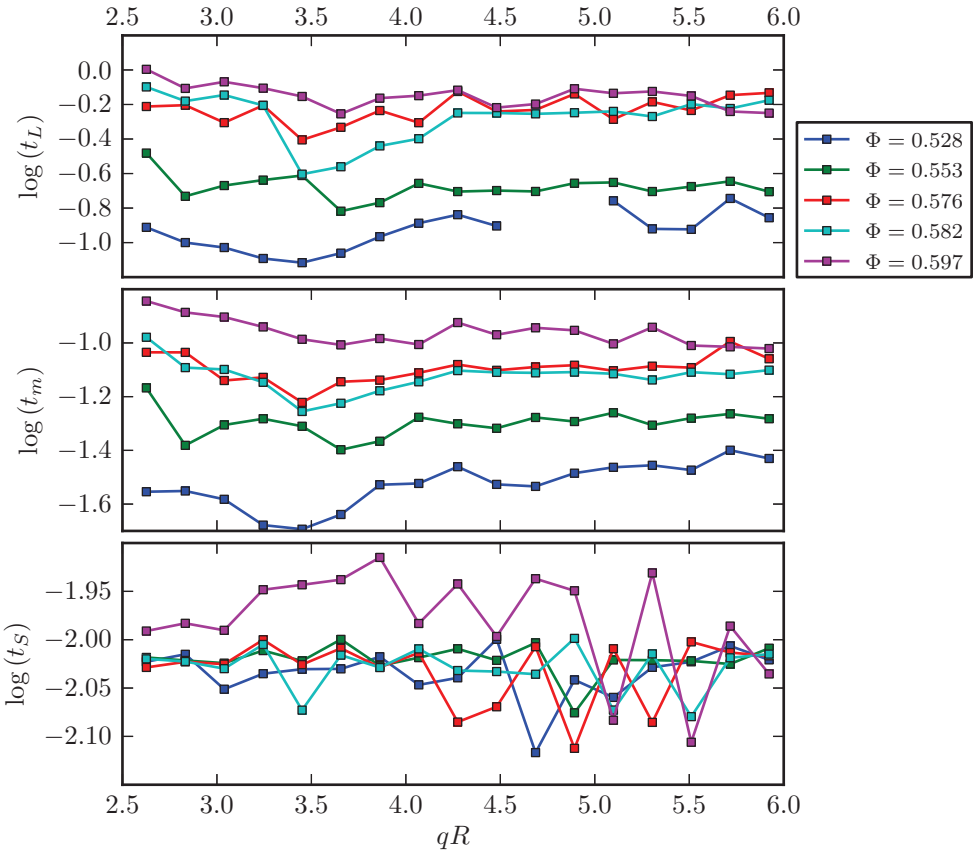

Figure 5.9: A plot of the two limiting times: t_S (circles) and t_L (squares) as a function of q. Different colors correspond to different volume fractions, as indicated in the legend.

Table 5.1: Characteristic times for different volume fractions at $qR = 3.66$. For comparison, the structural relaxation time: $\tau_R = R^2/D_0 = 12.481$ ms

Φ	t_S [ms]	t_m [ms]	t_L [ms]	R_S	R_c	τ_c [ms]	t_S/τ_c
0.528	9.33	22.97	86.91	0.262	0.083	0.93	10.03
0.553	10.01	40.02	152.06	0.197	0.066	1.13	8.86
0.576	9.80	71.69	465.44	0.139	0.052	1.35	7.26
0.582	9.64	59.63	275.04	0.143	0.048	1.09	8.84
0.597	11.54	98.31	556.72	0.087	0.039	2.34	4.93

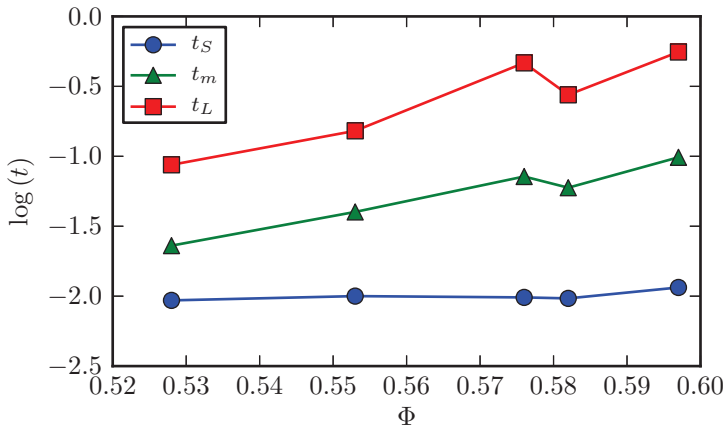

Figure 5.10: Volume fraction dependence of the characteristic time scales at $q \approx q_m$.

freezing transition volume fraction the decrease of $H(q)$ value indicates an increase in the strength of hydrodynamic interactions. The calculation of $H(q)$ is a complex, many-body problem and only an approximate theoretical treatment is feasible. Nevertheless, significant amount of experimental and simulation data on short-time dynamics of suspensions up to $\Phi \approx 0.494$ has been analysed and understood within the modified mode-coupling theory. A good example is given by Banchio *et al.* in [Banchio 2008], where the results of accelerated Stokesian dynamics (ASD) simulation are compared to several theoretical predictions and experimental results of Segrè *et al.* [Segrè 1995a]. In Stokesian dynamics the colloidal suspension is described by solving the Langevin equation, which is the equivalent of the Newton's second law of motion for a Brownian particle and takes the form [Banchio 2003]:

$$\mathbf{m} \cdot \frac{\mathrm{d}\vec{u}}{\mathrm{d}t} = \vec{F}^h + \vec{F}^b + \vec{F}^p, \tag{5.17}$$

where $\mathbf{m}$ is the generalized mass/moment of inertia tensor, $\vec{u}$ is the particle velocity vector and on the right hand side are the forces/torques acting on the particles, including the hydrodynamic forces $\vec{F}^h$, stochastic Brownian forces $\vec{F}^b$ and the deterministic nonhydrodynamic forces $\vec{F}^p$, either interparticle or external. The important feature of the Stokesian dynamics approach is the inclusion of many-body long-range hydrodynamic interactions, which are simplified in the popular, Brownian dynamics technique of solving equation 5.17. The ASD algorithm developed by Banchio and Brady [Banchio 2003] is an improvement reducing the computational cost of calculating the hydrodynamic interactions.

The principal peak $H(q_m)$ of $H(q)$ is shown in [Banchio 2008] to occur practically at the same wavevector value as the $S(q)$ peak. The peak amplitude as a function of Φ follows very well the simple empirical form obtained from rescaled MCT:

$$H(q_m) = 1 - 1.35\Phi \tag{5.18}$$

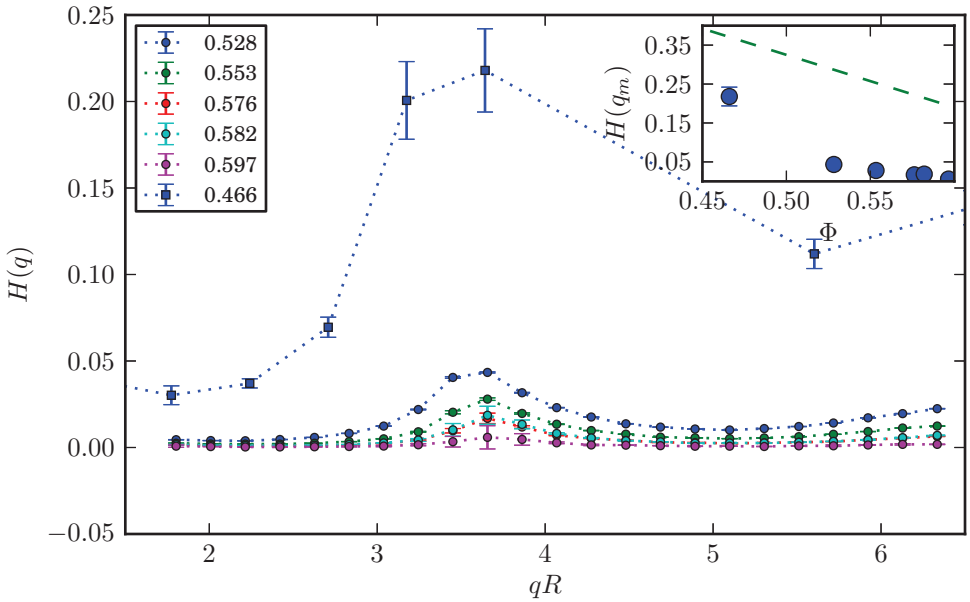

Figure 5.11: Hydrodynamic function $H(q) = S(q)D_S(q)/D_0$. The inset – $H(q_m)$ vs Φ (symbols) compared to the theoretical prediction from MCT [Banchio 1999b]: $H(q_m) = 1 - 1.35\Phi$.

up to the freezing transition. XPCS data presented in [Orsi 2012b], again at concentrations up tp $\Phi \sim 0.5$, are also in good agreement with equation 5.18. The inset of figure 5.11 shows the volume fraction dependence of $H(q_m)$ for the samples investigated in this thesis. The dashed green line is a plot of equation 5.18. It largely overestimates the value of $H(q_m)$ at $\Phi > 0.5$. The first data point, which is within the equilibrium fluid concentration range, lies much closer to the model curve. Considering the 3% uncertainty of the value of Φ and that the q value of this point is not exactly equal to q_m, it can be argued that the 0.466 concentration remains in agreement with previous results and fits well with equation 5.18, even though the statistical error bar (of the order of symbol size in the inset of figure 5.11) is much smaller than the distance to the theoretical curve. In summary, although the overall shape of $H(q)$ for hard-sphere suspensions does not significantly change above the freezing volume fraction, its magnitude is no longer described by predictions valid for $\Phi < 0.5$. A possible explanation can be that at these high volume fractions direct interparticle interactions become important even at short times, as concluded from the comparison of t_S and τ_c. Indeed, collisions can be responsible for the additional slowing down of particle dynamics, which is not explained by pure HI.

Focusing on the long-time dynamic behaviour, an approximately diffusive regime can always be observed in the data near the wavevector q_m, corresponding to the structure factor peak value. The time t_L indicating the beginning of long-time diffusion, is shown as a function of Φ in figure 5.10. With increasing particle volume fraction t_L moves towards longer times, indicating the approach of an arrested state. However, the anticipated freezing of the long time relaxation is not observed in the sample at $\Phi \approx 0.597$, which is above the previously identified glass transition volume fraction of ~ 0.58 [Orsi 2012b]. It should be stressed that the high uncertainty of the determined volume fraction (3%) prevents from drawing strong conclusions from this observation [Poon 2012]. Looking at the plot of normalized short- and long--time diffusion coefficients in figure 5.12 it is clear that the slowing down of the dynamics observed between the sample at $\Phi = 0.582$ and 0.597 is much larger than between the samples at lower concentrations.

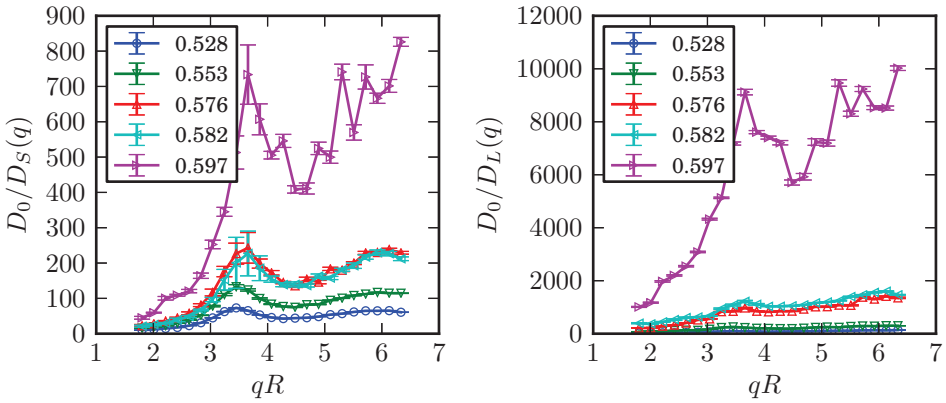

Figure 5.12: Inverse relative short- and long-time q-dependent diffusion coefficient (left and right panel respectively) as a function of qR for volume fractions indicated in the legend.

A comparison of results from viscometry and TCDLS presented in [Segrè 1995b] revealed a remarkable scaling between the long-time diffusion coefficient and the low-shear-rate viscosity of a similar suspension of hard-sphere particles. More precisely, the cited results show that:

$$\frac{D_0}{D_L(q_m)} = \frac{\eta}{\eta_0} \tag{5.19}$$

Here η is the suspension viscosity and η_0 is the viscosity of the suspending liquid. Although no viscometric measurements were performed for this thesis, equation 5.19 can be used to compare the values of $D_0/D_L(q_m)$ to a model of $\eta(\Phi)$ derived by Cohen *et al.* in [Cohen 1997]. There the authors present an approximate equation for the low-shear-rate viscosity as a function of volume fraction, which is shown to follow well several data series taken on sterically stabilized silica suspensions. The

equation has the form:

$$\eta(\Phi) = \eta_0 \chi(\Phi) \left[1 + \frac{1.44\Phi^2 \chi^2(\Phi)}{1 - 0.1241\Phi + 10.46\Phi^2} \right] \tag{5.20}$$

where $\chi(\Phi)$ is the fraction of particle pairs at contact, calculated from the Carnahan-Starling expression:

$$\chi(\Phi) = \frac{1 - 0.5\Phi}{(1 - \Phi)^3}. \tag{5.21}$$

A comparison of η/η_0 derived from equation 5.20 and the experimental data for $D_0/D_L(q_m)$ is presented in figure 5.13. Additionally to the samples at $\Phi > 0.5$, a data point for $\Phi = 0.466$ is added, obtained from a point detector measurement. The data points clearly deviate from the theoretical curve at high volume fractions. This behaviour is in qualitative agreement with the observations reported in [Phan 1996], where it has been shown that the relative viscosity data for concentrated suspensions of PMMA-PHSA spheres, above the freezing transition at $\Phi \approx 0.494$, significantly deviate towards higher values from the ones reported for silica suspensions.

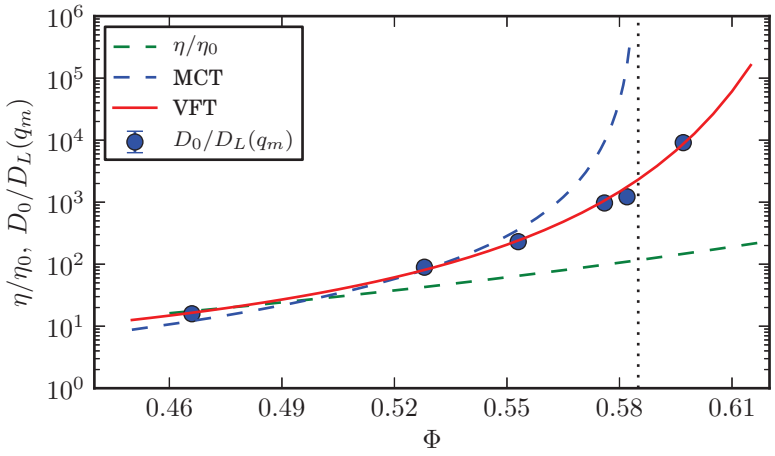

Figure 5.13: Comparison of the model expression for η/η_0 (from equation 5.20) and the experimental data for $D_0/D_L(q_m)$. The uncertainties of the data points are smaller than the markers used to plot them.

The strong divergence of η/η_0 (or $D_0/D_L(q_m)$) resembles the behaviour of the viscosity in fragile glass formers, described by the Vogel-Fulcher-Tammann (VFT) form [Debenedetti 2001]:

$$\eta = A \exp\left[\frac{B}{T - T_0} \right] \tag{5.22}$$

where A and B are temperature-independent constants, and T_0 is the transition temperature. For the description of a hard-sphere colloidal suspension, equation

5.22 can be transformed to describe the volume fraction dependence of the structural relaxation time τ_α [Brambilla 2009]:

$$\tau_\alpha = \frac{1}{D_L(q)q^2} = C \exp\left[\frac{D}{(\Phi - \Phi_0)^\delta}\right] \tag{5.23}$$

with the appropriate set of constants C and D. A simple transformation of equation 5.23 allows to fit the data presented in figure 5.13, allowing for variation of parameters C, D, Φ_0 and δ. The resulting best fit (dashed red line) follows the data very well with parameter values presented in table 5.2. The error bars in figure 5.13 are smaller than the data point markers. The fitted critical value Φ_0 agrees remarkably

Table 5.2: Fit results for the VFT formula (equation 5.23).

C ($\times 10^{-4}$) [s]	D	Φ_0	δ
3 ± 2	0.8 ± 0.3	0.68 ± 0.01	1.00 ± 0.01

well with the random close packing volume fraction found in simulation studies for hard spheres with 10% polydispersity [Schaertl 1994]. In conclusion, these results show an exponential divergence of τ_α at a critical volume fraction $\Phi_0 \approx \Phi_R \approx 0.68$, significantly above the commonly quoted value of glass transition of hard sphere colloids at $\Phi_g \approx 0.58$. Similar findings using a combination of DLS and computer simulations were reported in [Brambilla 2009]. There, good agreement with formula 5.23 has been found with $\delta = 2$. The obtained value of $\Phi_0 = 0.637$ was also significantly higher than Φ_g. However, the Φ_0 value is significantly smaller than found in this thesis.

Further insight into the form of dynamical slowing down of the colloidal suspension can be gained by looking at the peak value of the reduced, short- and long-time diffusion coefficients: $D_S(q_m)/D_0$ and $D_L(q_m)/D_0$, which correspond to the MCT β and α relaxation measured near $q = q_m$. Plotted as a function of the so-called "separation parameter" $|\Phi_g - \Phi|$, the short-time relaxation has been shown to follow a power scaling law [van Megen 2007a, Orsi 2012b]:

$$D_S(q_m) \propto |\Phi_g - \Phi|^{1.66} \tag{5.24}$$

which should be valid not only in the liquid state but in a glass as well [Götze 1991]. A different power is predicted for $D_L(q_m)$:

$$D_L(q_m) \propto |\Phi_g - \Phi|^{2.58}. \tag{5.25}$$

The two scaling laws described by equations 5.24 and 5.25 are tested in figure 5.14. Additional, lower concentration data is also shown, previously obtained by Orsi *et al.* [Orsi 2012b] and Zontone *et al.* [Zontone] in a similar system (sterically stabilised PMMA hard-sphere particles). Although the lower concentration data appear to follow the theoretical lines reasonably well, the points for concentrations

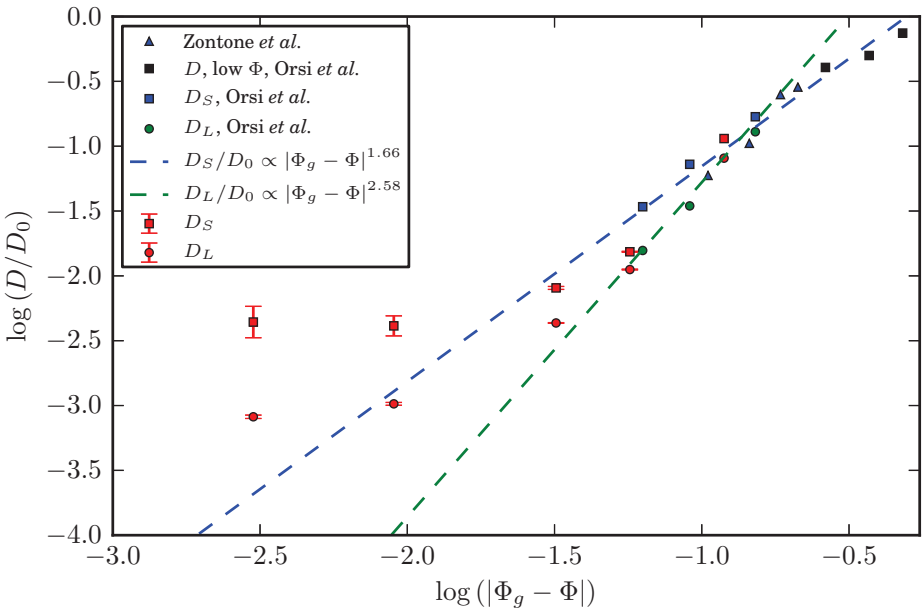

Figure 5.14: Normalized diffusion coefficient measured at $q \approx q_m$ vs the separation parameter $|\Phi_g - \Phi|$, where $\Phi_g = 0.585$. The dashed blue and green lines correspond to the MCT predictions described by equations 5.24 and 5.25.

closer to Φ_g deviate towards higher values, avoiding the final freezing at the assumed glass transition point. The interpretation of figure 5.14 should be cautious. Firstly, the determination of the absolute sample volume fraction is not precise [Poon 2012]. Shifting the fitted values of Φ within the estimated uncertainty of 3% can lead to different conclusions. Secondly, the location of the colloidal glass transition point, the very nature of the transition and the form of the structural relaxation time divergence remain open issues [van Megen 1998, Cheng 2002, Brambilla 2009]. Nevertheless, together with the analysis presented in figure 5.13, the results point towards the conclusion that near the MCT predicted glass transition a cross over from an algebraic (equation 5.25) to an exponential (equation 5.22) divergence of the relaxation occurs. Hence, there is no glass transition visible in the data.

5.3.3 Scaling of the intermediate scattering function

An interesting observation regarding dynamics of colloidal hard spheres at high volume fractions has been reported in [Segrè 1996]. The authors used dynamic light scattering to measure the intermediate scattering functions $g_1(q,t)$ in a range of volume fractions encompassing the equilibrium and metastable fluid states. The results reveal a simple scaling procedure which collapses the $g_1(q,t)$ measured for different q values on a single master curve. The procedure can be described by the

following equation:

$$\frac{\ln\left[g_1(q,t)\right]}{D_S(q)q^2} = -\chi(t), \tag{5.26}$$

where $\chi(t)$ is a q independent function of time. An example of the scaling is shown in figure 5.15. This behaviour was observed for all Φ values up to the glass transition.

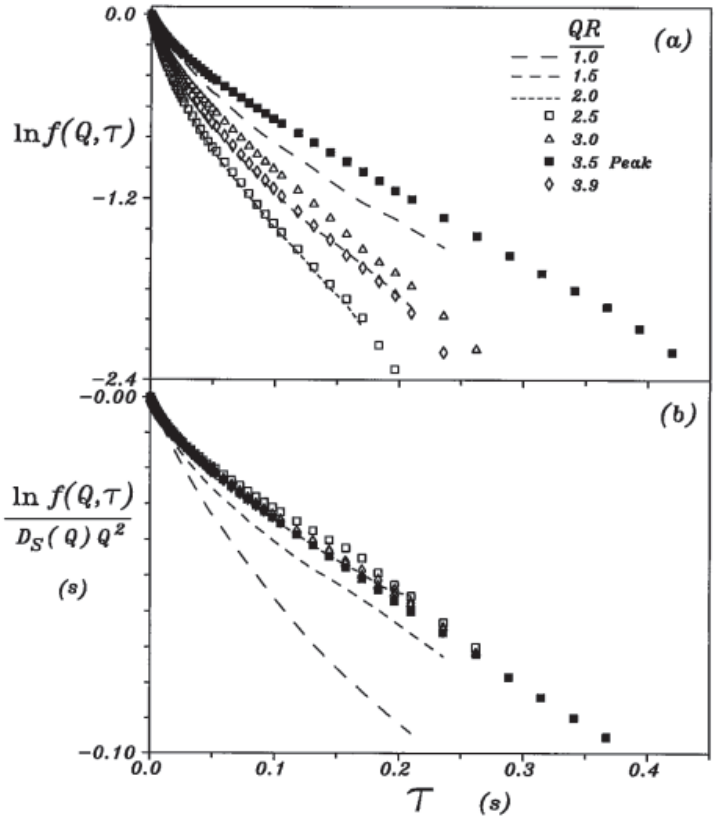

Figure 5.15: The intermediate scattering functions from DLS measurements of hard-sphere particles at volume fraction $\Phi = 0.465$. Panel (a) shows the natural logarithm of the ISF vs. time. In panel (b), the scaling procedure, described by equation 5.26 has beed applied, leading to the collapse of the data on a single master curves for qR values above 2.7. Figure reproduced from [Segrè 1996].

When the short- and long-time diffusion coefficients were plotted as $D_0/D_S(q)$ and $D_0/D_L(q)$, they followed the oscillations of the structure factor, being related to each other by a factor of roughly 4.3 at $\Phi = 0.465$ (see figure 5.16). The suggested interpretation of this finding is that the two relaxation mechanisms: short- and long-time, are both related to self-diffusion. This is counterintuitive, since the long-time relaxation origins from large-scale collective motion of particles, and its connections to single-particle diffusion is not obvious.

The system used by Segrè et al comprised PMMA particles, sterically stabilized with thin layers of poly-12-hydroxystearic acid, suspended in *cis*-decalin or *cis*-

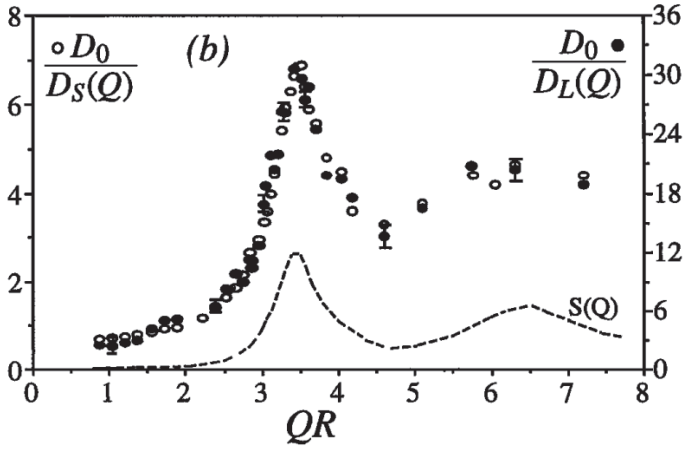

Figure 5.16: Normalized short- and long-time diffusion coefficients extracted from fits of the linear regions in $\ln[g_1(q,t)]$ vs q^2t at volume fraction $\Phi = 0.465$. The dashed line is the the theoretical static structure factor $S(q)$. Figure reproduced form [Segrè 1996].

-decalin/tetralin mixture (to suppress multiple scattering by matching the index of refraction of the particles and the suspending medium). In order to probe a wide range of volume fractions, two preparations of particles were used. First set of samples, with *cis*-decalin as the suspending medium, was composed of particles of a mean radius $R = 178\ nm$ and size polydispersity $\sigma \approx 0.05$. A method reported in details in [Segrè 1995a] was used to calibrate the sample volume fraction Φ by assuming the observed freezing concentration to be $\Phi = 0.494$, corresponding to the value predicted for perfect hard spheres. Samples at lower Φ were prepared by dilution. To study $\Phi > 0.494$ the authors used particles of $R = 207\ nm$ and larger polysdispersity, $\sigma \approx 0.12$, which prevented crystallization.

Several studies, both experimental and theoretical, have been reported up to date in the subject, giving different results. XPCS measurements on concentrated, *charge-stabilized* polystyrene latex spheres suspended in glycerol ([Lurio 2000]) showed no scaling of $g_1(q,t)$. The authors investigated a range of samples with volume fractions $0.027 \lesssim \Phi \lesssim 0.52$. They were able to recognize the two diffusive regions for $\Phi \gtrsim 0.34$. The short- and long-time diffusion coefficients were determined by linear least-square fits of time ranges where the $log[g_1(q,t)]$ showed linear time dependence. The calculated $D_S(q)/D_L(q)$ ratio was clearly q dependent. Also, the intermediate scattering functions, scaled as in [Segrè 1996] did not collapse on a single master curve. The discrepancy between the presented results and those of [Segrè 1996] has been attributed to the possible difference in the dynamic behaviour of sterically- and charge-stabilized systems, which in fact has been reported in a recent study [Robert 2008].

Surprisingly, the authors of [Holmqvist 2010] obtained results confirming the scaling in a suspension of charge-stabilized particles (DLS study). They also found

that the scaling is an approximate feature and the long-time mode is clearly observable only where the $S(q)$ is large. Particles used in their work were silica spheres coated with trimethoxypropyl methacrylate of radius $R = 136$ nm and polydispersity of $\sigma_R/R = 0.06$ (determined by SAXS), suspended in an index-matching 80:20 toluene-ethanol mixture. Volume fractions up to the freezing transition at $\Phi \approx 0.16$ were investigated.

The idealized MCT [Götze 1991] has been used to provide a semiquantitative explanation of the $g_1(q,t)$ scaling [Fuchs 1999], even though in MCT the α and β relaxations have different physical origins. The long-time, structural relaxations (α) have a non-diffusive character, but at high enough scattering vector q values and low enough values of time, this behaviour may not be very well pronounced. As a result, the intermediate scattering functions scaled as in equation 5.26 approximately collapse on a single master curve. The authors stress that this behaviour may be restricted to the specific system of sterically stabilized hard-sphere like colloids, and may not necessarily be present in other, like charge stabilized particles. The above mentioned experimental results reported in [Lurio 2000, Lumma 2000a] are in good agreement with this statement.

Another theoretical approach has been presented in [Verberg 1999, Verberg 2000]. The authors extend the results obtained by Beenakker and Mazur in [Beenakker 1984] by describing $D_S(q)$ and $D_L(q)$ in terms of the cage-diffusion process, using a mean-field approximation of the diffusion tensor. The derived expressions are in relatively good agreement with the experimental results of Segrè and Pusey [Segrè 1996]. Collective short- and long-time diffusion coefficients are shown to oscillate in a similar manner around the corresponding self-diffusion coefficients – $D_S^s(q)$ and $D_L^s(q)$. Their ratio, being approximately q independent, is the source of the observed scaling. It holds only near the principal peak of $S(q)$ due to the limiting values of the derived expressions, which show that $D_L/D_S \to 1$ for both $q \to 0$ and $q \to \infty$.

In [Martinez 2011] the authors only observe the long-time diffusive behaviour of the sterically stabilized particles at q values near q_m. Although the short-time diffusive regimes were clearly visible in the data over several decades for all volume fractions and qR values probed, the long-time diffusive behaviour could only be identified at q values corresponding to the structure factor peak (q_m) for $\Phi \geq 0.498$. Consequently, the authors were unable to test whether or not the ratio $D_S(q)/D_L(q)$ is q-independent. Instead, the ratio of an apparent diffusion coefficient $D(q,\tau_x)$ at several delay times τ_x was defined and the ratio of $D(q,\tau_x)/D_S(q)$ was calculated for several volume fractions. The results showed no signs of scaling. The normalized inverse of the short-time diffusion coefficient $D_0/D_S(q)$ was shown to scale with the structure factor oscillations, in agreement with previous results. The authors also note that with increasing volume fraction a faster deviation from diffusive behaviour was observed, even though the dynamics was slowing down. Although the long-time diffusive behaviour has not been observed, a plot of the time--dependent diffusion coefficient, $D(q,t) = \partial \ln[g_1(q,t)]/q^2\partial t$ divided by $D_S(q)$ was shown to collapse on a single master curve for $qR \gtrsim 2$, in agreement with the findings

reported in [Segrè 1996]. The authors explain the lack of a long-time diffusive regime by reasoning that in the accessible time scales the particles are unable to move the distances necessary for the number density fluctuations to forget packing constraint effects. The suspension studied by Segrè *et al.* comprised particles of a copolymer core of methylmethacrylate and trifluorethylmethacrylate, the latter added to enable refractive index matching in the suspending liquid – *cis*-decalin. Particles were sterically stabilized by an approximately 10 nm thick layer of poly-12-hydroxystearic acid and had a radius $R = 185$ nm with 8% - 9% polydispersity. The range of volume fractions used was $0.01 \leq \Phi \leq 0.549$.

To relate the results presented in this thesis to previous finding, the scaling is first tested by plotting the intermediate scattering functions in the same form as presented in [Segrè 1996], that is $\ln[g_1(q,t)]/D_S(q)q^2$, for $q > 2.5$ and all volume fractions are presented in figure 5.17. The curves collapse on a single master curve reasonably well up to the solid blue line, indicating t_L. They diverge above that value, suggesting that the D_S/D_L ratio is *not* q-independent. This behaviour is similar to the one observed by Martinez *et al.* [Martinez 2011], who also found that the the scaling by $D_S(q)$ fails at long times for a similar, sterically stabilized system. Corresponding results were also obtained for charge stabilized particles, presented in [Lurio 2000].

The ratio of the short- and long-time diffusion coefficients is plotted as a function of qR for all samples in figure 5.18. Significant q dependence is clearly visible near q_m. Although for $qR \gtrsim 4$ the ratio becomes reasonably constant, it should be stressed, that in this region the long- time diffusive behaviour, and therefore $D_L(q)$, is not very well defined for the lowest concentrations studied.

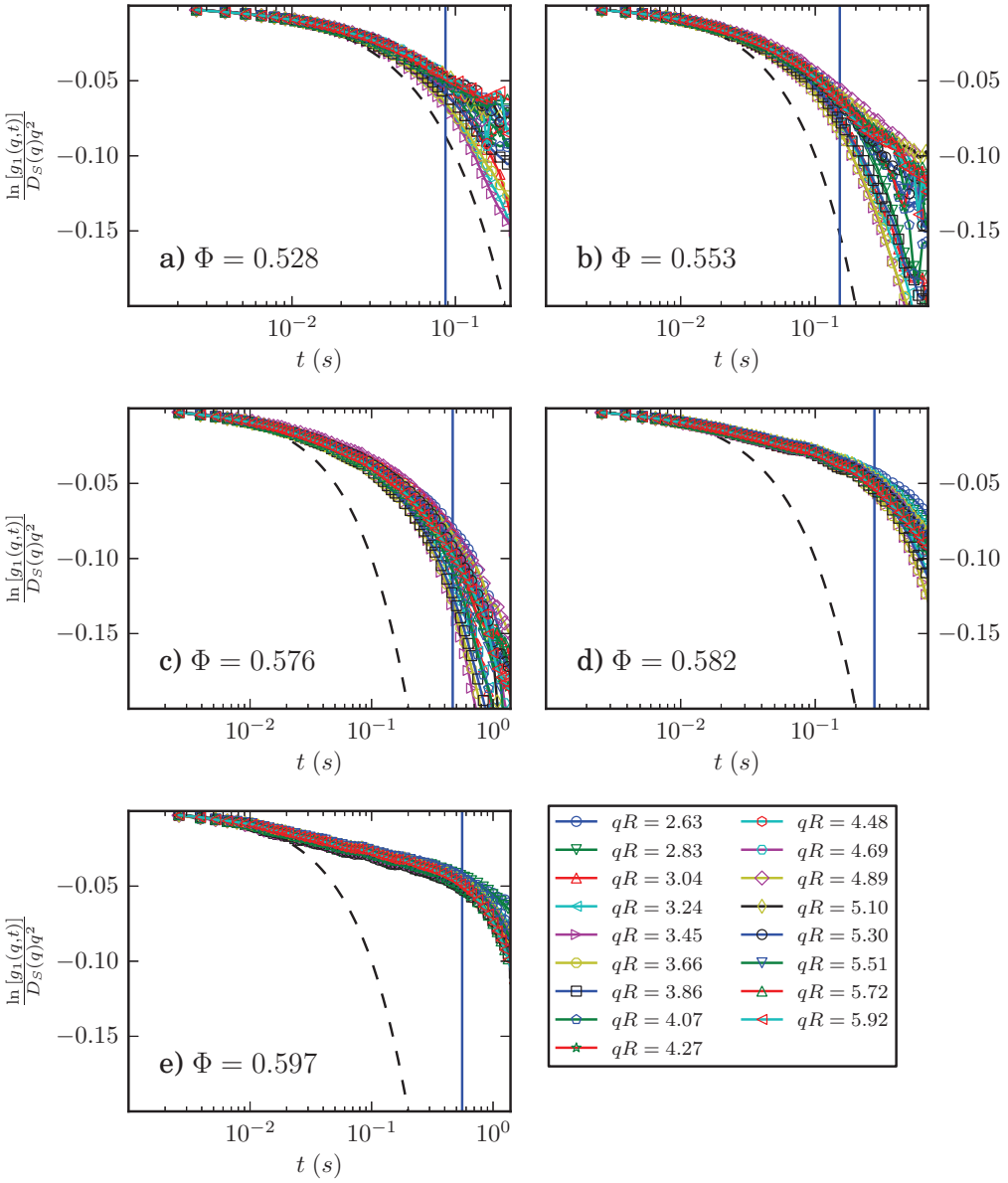

Figure 5.17: Logarithm of the intermediate scattering function ($g_1(q,t)$) divided by the short-time diffusion coefficient $D_S(q)q^2$ for volume fractions and qR values as indicated. In this representation the data shown in [Segrè 1996] collapsed onto a single master curve for $qR \gtrsim 2.5$. The black dashed line represents the short-time diffusion coefficient (slope -1). Vertical solid line marks the beginning of the long-time diffusive region (t_L) for $g_1(q_m,t)$ – measured near the $S(q)$ peak.

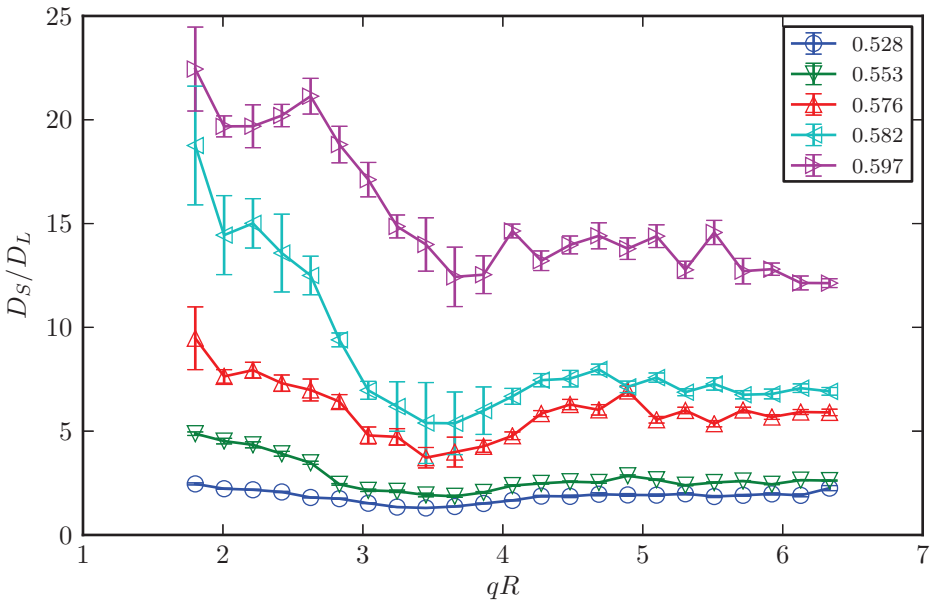

Figure 5.18: Ratio of the short- and long-time diffusion coefficients as a function of qR for samples at different volume fractions.

5.3.4 Non-exponential long-time relaxation

Another interesting observation can be made by comparing the normalized correlation function for different concentrations and qR values, plotted in the typical log-lin representation (figure 5.19). It becomes evident that for the most concentrated sample not only the relaxation time becomes slower, but also the shape of the correlation function changes. To quantify this decay the long-time parts of the

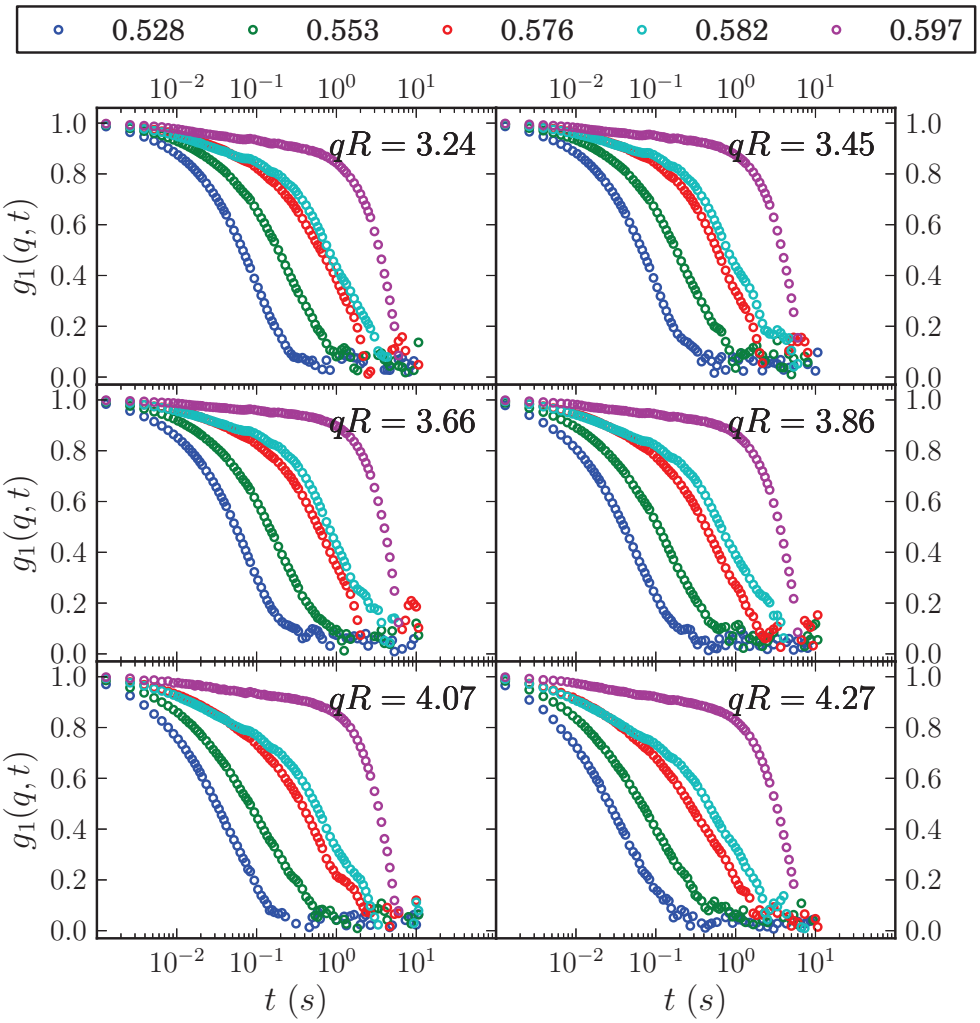

Figure 5.19: Comparison of the intermediate scattering functions for all volume fractions probed at qR values indicated in the figure.

correlation functions have been fitted with the KWW formula:

$$g_2(q,t) = 1 + \beta \exp\left[-2(\Gamma t)^{\gamma}\right]. \tag{5.27}$$

The correlation functions together with the fits are shown for several q values in figure 5.20. The resulting values of γ and Γ are plotted as a function of qR in the

two bottom panels of figure 5.20. The larger than one value of γ indicates faster than exponential decay, which is very unusual for this system. Typically, the α relaxation of a glass-forming liquid is well described by a stretched exponential, with $\gamma < 1$ [Debenedetti 2001]. Compressed exponential relaxation with $\gamma \approx 3/2$ has been observed by Cipelletti *et al.* [Cipelletti 2000] in a fractal colloidal gel of aggregating polystyrene particles. A convective rather than diffusive mechanism was proposed to explain the relaxation behaviour, although density matching of the system rules out a global sedimentation effect. The 3/2 value of the KWW exponent has been explained by heterogeneous "micro collapses" of the gel and its elastic (solid-like) response to the resulting deformation. A model for the local rearrangements has been proposed by Bouchaud and Pitard in [Bouchaud 2002], providing an analytical form of the dynamic structure factor which is in agreement with the experimental results of Cipelletti *et al.* Later experiments on different systems reported in [Cipelletti 2003] suggest that such non-diffusive slow dynamics may be a universal feature of disordered, jammed soft-matter. The compressed exponential shape and q proportionality of the relaxation rate can be explained by ultraslow ballistic motion of the scatterers, caused by release of internal stresses. In fact, the exponent $1 < \gamma < 2$ can be explained by a wide distribution of ballistic relaxation times, while $\gamma < 1$, often observed in glassy materials, indicates a wide distribution of diffusive or subdiffusive relaxation times [Cipelletti 2003]. The explanation proposed by Cipelletti *et al.* for $\gamma = 3/2$ and quantified by Bouchaud and Pitard points towards dynamical heterogeneities, which can be detected by calculating the normalized variance $\chi(q,t)$ of the two-time correlation function (equation 2.22), which is related to the dynamic susceptibility [Madsen 2010, Duri 2006]. The use of the MAXIPIX detector allowed to calculate normalized variance $\chi(q,t)$ of the two time correlation function (see section 2.3.2), which is plotted as red lines, together with $g_2(q,t)$ in figure 5.20. Clearly, $\chi(q,t)$ is flat which is a sign of simple Gaussian, non-heterogeneous dynamics. This result can be compared to similar observations made on a system of cross-linked polymer gels during formation [Czakkel 2011]. In that work compressed exponential decays of the long-time ISF were also observed, together with a $\Gamma \propto q$ scaling. Additionally, a strong ageing of the dynamics was observed, with no signs of dynamical heterogeneity. The system studied by Czakkel *et al.* is fundamentally different from the one used in this thesis. In particular, no significant age dependence of the dynamics during the measurement time is detected in the hard-sphere suspension, as can be seen in the plot of the two-time correlation function in figure 2.6, given as an example of stationary dynamics. We conclude that the dynamics of the concentrated colloidal suspension is best described within a jamming model behaving in a solid-like manner but without dynamical heterogeneity. This implies kinetic arrest rather than a glass transition scenario being responsible for the slowing down of dynamics.

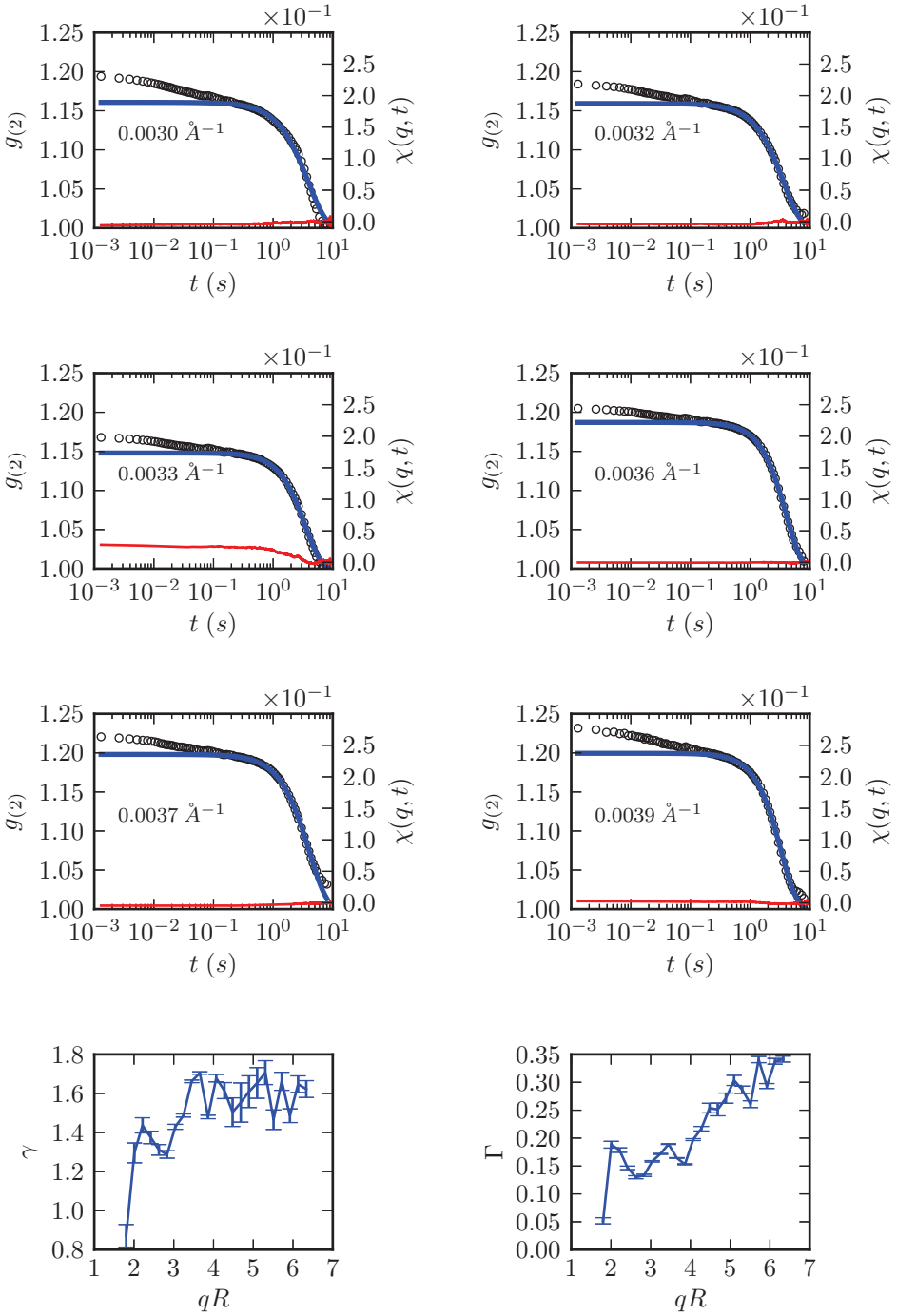

Figure 5.20: A plot of correlation functions $g_2(q,t)$ measured on the sample at $\Phi = 0.597$ for several q values. Blue solid lines indicate fits of the long-time regions with the KWW formula. Fit parameters of the exponent γ and the relaxation rate Γ are presented as a function of q in the lower left and right panels respectively.

5.3.5 Two-time correlation functions

Jammed, soft-matter systems have been reported to undergo ageing on very long time scales of the order of hours, like in the case of a colloidal suspension of laponite [Bellour 2003]. In search of such behaviour in the most concentrated sample used in this thesis ($\Phi = 0.597$), several XPCS data series were taken over a period of ~ 9 hours counting from the capillary filling time. Figure 5.21 presents three two-time correlation functions $G(q, t_1, t_2)$ measured for the same q value at different sample ages. The two-time correlation in the left panel was previously shown in figure 2.6. It shows stationary dynamics with no pronounced signs of ageing. This data set has been used to calculate $g_2(q, t)$, which has been analysed in the previous sections of this chapter. The normalized variance $\chi(q, t)$ of this series, presented in figure 5.20 also showed no signs of dynamical heterogeneity. A measurement taken ~ 2 hours later on a different location of the sample (to exclude the potential influence of radiation damage) reveals a dramatic change in the dynamics (middle panel of figure 5.21). Several transitions from slow to fast decorrelation can be seen within the presented time window. This behaviour persists even after 9 hours from the capillary filling time (right panel in figure 5.21).

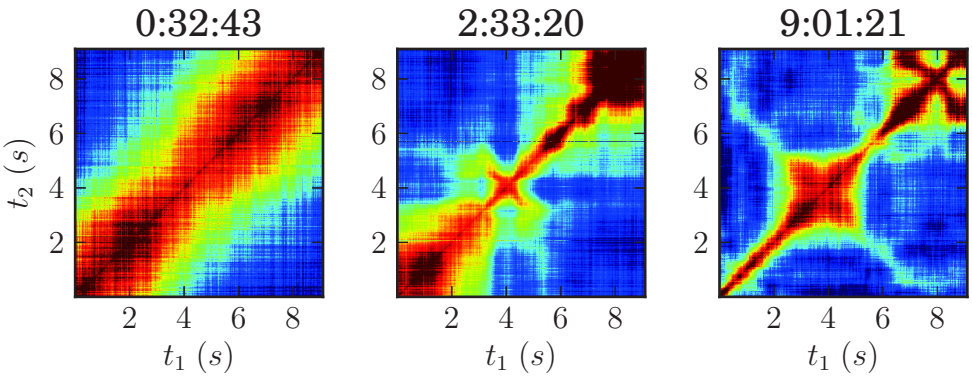

Figure 5.21: Two time correlation functions for the same sample and q value at different sample ages, measured from the capillary filling time.

As explained in section 2.3.2, by averaging of the two-time correlation function along the diagonal $t = (t_1 + t_2)/2$ the regular correlation function $g_2(q, t)$ is retrieved. This procedure has been performed on the $G(q, t_1, t_2)$ presented in the middle panel of figure 5.21. Several regions were chosen to calculate $g_2(q, t)$, as marked by the numbered shaded areas in the left panel of figure 5.22. These correlation functions, plotted in the upper right panel, reveal significant changes in the long-time range, as well as contrast variations. Normalized variance $\chi(q, t)$ shown in the lower right panel of figure 5.22 has a broad peak in the same time range in which $g_2(q, t)$ significantly varies with measurement time. As mentioned before, this could indicate dynamical heterogeneities, however such an interpretation is not

necessarily valid. The complex, non-stationary dynamics may also be responsible for this peak. In the work of Czakkel *et al.* [Czakkel 2011], despite the ageing behaviour observed in $G(q, t_1, t_2)$, no peak in $\chi(q, t)$ and therefore no heterogeneities are seen when the time evolution of $G(q, t_1, t_2)$ is properly normalized out. An opposite example can also be given. The study of a 2D gel formed by a monolayer of gold nanoparticles reported in [Orsi 2012a] shows clearly stationary two-time correlation functions, indicating no age dependence of the dynamics, but strong peaks in $\chi(q, t)$ are unambiguously associated to heterogeneous dynamics.

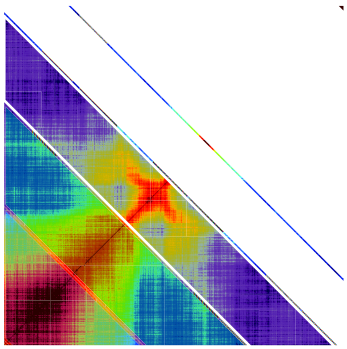

shorter and grows with sample age, indicating that the dynamics is affected at all time scales by the events observed in $G(q, t_1, t_2)$.

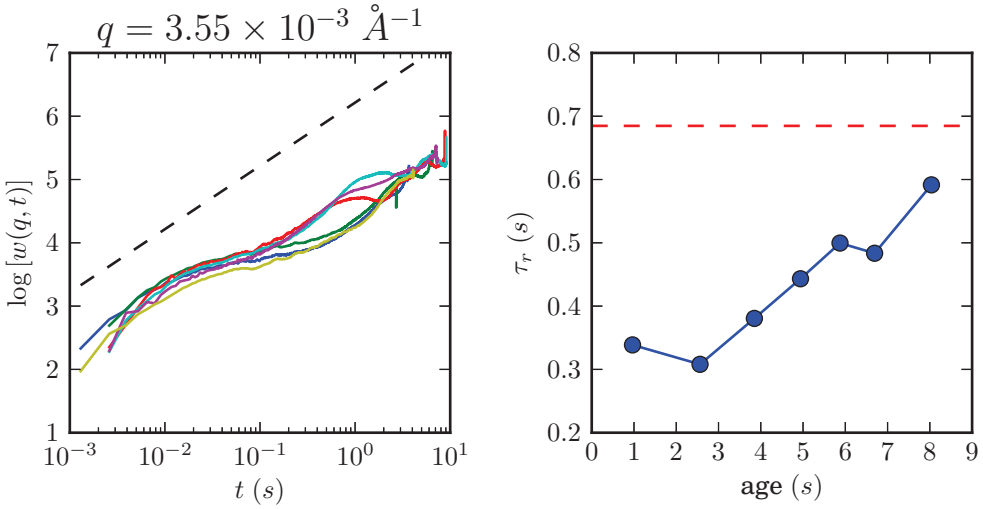

Figure 5.23: Left panel: width functions calculated for the correlation functions extracted from $G(q, t_1, t_2)$ for the sample $\sim$ 2.5 h old. The dashed black line indicates slope 1. Right panel: age dependence of the short-time relaxation times τ_r. The dashed red line marks the relaxation time extracted from the stationary data series.

Access to different q values allows to look at the character of the dynamics at different length scales. The two-time correlation functions for $2.75 \times 10^{-3} \leq q \leq 4.95 \times 10^{-3}$ Å^{-1} are plotted in figure 5.24. They all present similar features, indicating that the physical process behind them simultaneously affects all length scales probed. This is better seen in the "waterfall plot", shown in figure 5.25 for the sample 9 hours old, presenting the time evolution of the intensity of all pixels corresponding to the same q, near the structure factor peak. Several points in time can be found where the speckles "jump" simultaneously in many pixels. These points can be identified as the onsets of slowing down or speeding up of the dynamics seen in the two time correlation function plot (right panel of figure 5.21).

Although it is difficult to quantify this process, some qualitative comparisons can be made with results found in literature. The distinct square seen in the $G(q, t_1, t_2)$ plot in the right panel of figure 5.21 describes a slowing down of the dynamics up to a certain moment in time followed by the reverse process – transition from slow to fast decorrelation. Many of the features present can be described in a similar manner, with varying times of duration and relaxation. Similar behaviour has been reported in [Sanborn 2011], where the authors use multi-speckle XPCS to study the martensitic phase transition in cobalt. It is a structural transformation between two crystalline phases involving atomic rearrangement which shear the unit cell. The produced strains are released in rapid avalanche-like events, which lead to

characteristic features in the two-time correlation functions, resembling the above described square in the right panel of figure 5.21. This scenario also fits well the concentrated colloidal suspension studied in this thesis. The exponential form of $D_0/D_L(q_m)$ vs Φ being well described by the VFT formula (section 5.3.2) together with compressed exponential relaxation of the $g_2(q,t)$ for the most concentrated sample (section 5.3.4) and complex, non-stationary dynamics, observed after a certain waiting time all point towards a jammed state of the particles being reached upon increase of Φ. The sample at $\Phi = 0.597$ behaves nearly like a solid. The complex features present in $G(q,t_1,t_2)$ could than be explained as originating from large, sudden particle rearrangements – avalanches, caused by releases of stress accumulated over time.

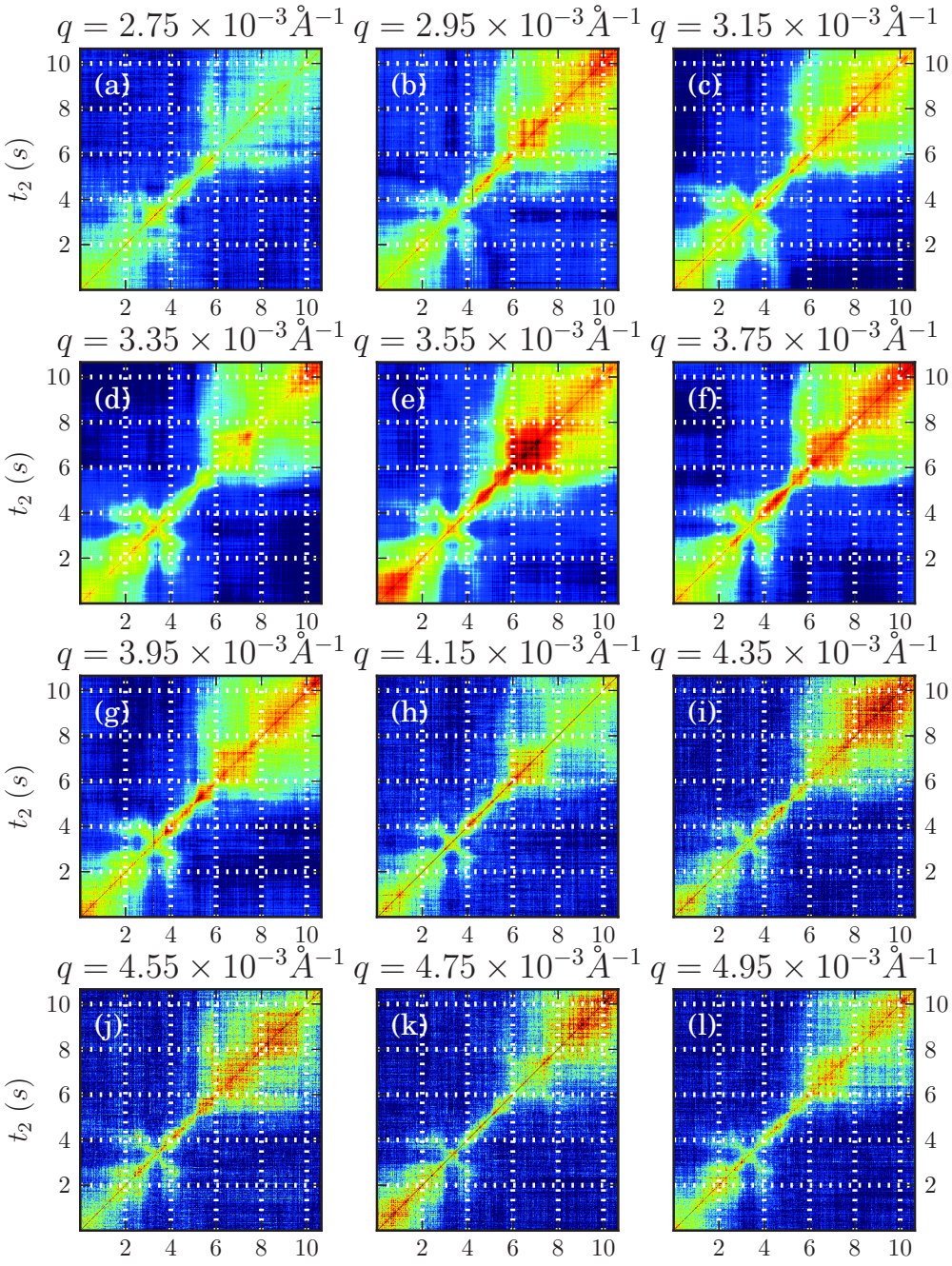

Figure 5.24: Two time correlation function for different q values.

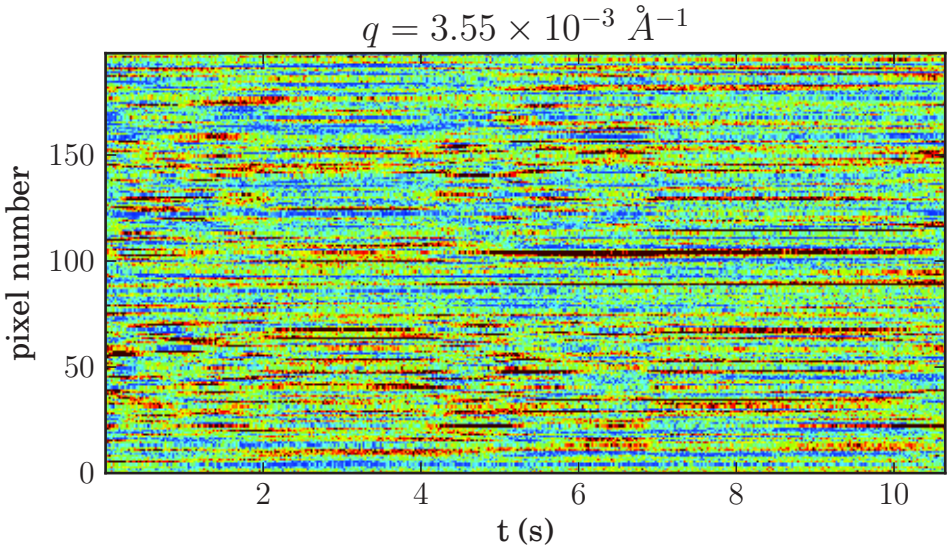

Figure 5.25: The so-called "waterfall plot" of time evolution of the intensity of all pixels corresponding to the same q. Measurement taken on a sample approximately 9 hours old.

Conclusion et perspectives (français)

Le sujet de cette thèse était d'étudier le comportement dynamique d'une suspension colloïdale de particules de type sphères dures. Plus spécifiquement, l'intérêt portait sur la dynamique complexe à haute fraction volumique en particules, avec le but d'explorer le phénomène d'arrêt dynamique observé, qui n'est accompagnée d'aucune signature structurelle. Cette étude a éte effectuée principalement par diffusion de rayons X aux petits angles (SAXS) et spectroscopie de corrélation de photons X (XPCS).

Des études précédentes, combinant un dispositif d'écoulement et XPCS, ont montré la faisabilité de mesures simultanées de la dynamique diffusive et de la réponse advective au cisaillement appliqué. Il était intéressant d'appliquer cette technique, non plus à une suspension diluée mais à des colloïdes concentrés susceptibles de présenter un comportement non-Newtonien. Mis à part l'intérêt fondamental d'étudier l'écoulement, le comportement dynamique des particules, et leurs interactions, l'écoulement de l'échantillon pendant l'expérience est également une façon très pratique d'éviter l'endommagement par irradiation de l'échantillon. Ceci est montré de manière qualitative sur la figure 5.26, qui montre l'évolution au cours du temps d'une figure de diffusion en SAXS dans un set typique de données XPCS. Les données présentées dans la série supérieure de courbes ont été acquises sur un échantillon sans écoulement. Une augmentation systématique de l'intensité avec le temps peut être observée aux petits vecteurs d'onde, indiquant la croissance d'agrégats de particules. Ceci est clairement modifié quand l'échantillon est soumis à écoulement pendant la mesure, ainsi qu'on peut le voir dans la partie inférieure de la figure 5.26, où toutes les courbes se confondent. L'endommagement par irradiation est évité grâce au renouvellement constant de l'échantillon. Néanmoins, cette méthode a ses limitations. Pour l'XPCS, la présence de l'écoulement induit un mécanisme de décorrélation lié au mouvement advectif des particules, qui s'ajoute à la diffusion. Si les échelles de temps caractéristiques qui correspondent à ces processus ne sont pas bien séparées, il peut être impossible de les distinguer et de tirer des conclusions exploitables sur la dynamique des diffuseurs. Ceci est un problème dans le cas de suspensions concentrées, où la dynamique devient très lente. Imposer un écoulement à l'échantillon peut alors mener à une décorrélation complète de la fonction de diffusion intermédiaire mesurée, qui ne rendra compte que de la translation des particules à travers le volume diffusant. Une telle mesure ne contient pas d'information utile. Les limitations pratiques doivent aussi être considérées – il n'est pas toujours possible d'appliquer un écoulement continu suffisamment lent pour effectuer l'expérience.

En utilisant les propriétés uniques d'une source de rayonnement synchrotron de troisième génération, et le détecteur MAXIPIX rapide à comptage de photon unique disponible sur la ligne ID10 de l'ESRF, il a été possible de mesurer les fonctions de diffusion intermédiaires dans une gamme de vecteurs d'onde et de concentrations peu accessible expérimentalement via d'autres techniques. Les fractions volumiques ont été déterminées en ajustant les profils radiaux de la figure de diffusion moyennés axialement et dans le temps. Pour la première fois, à notre connaissance, des mesures de XPCS ont été effectuées sur des suspensions de sphères dures à des fractions volumiques comprises entre 0.5 et 0.6. La décroissance en deux temps caractéristique des fonctions de diffusion intermédiaires a été observée. En représentant les données sous forme de "fonctions de largeur" (width functions), le caractère des relaxations a pu être déterminé sans modèle a-priori. Dans la limite des temps courts, une décroissance exponentielle a pu être observée pour toutes les concentrations dans une large gamme de q. Néanmoins, aux temps longs une décroissance approximativement exponentielle a pu être distinguée pour chaque échantillon seulement aux environs de $q = q_m$. Cette décroissance a persisté à de plus grandes valeurs de q seulement pour les échantillons les plus concentrés ($\Phi = 0.597$).

Une analyse des échelles de temps limitantes extraites des fonctions de largeur avec une procédure numérique simple a montré que le régime diffusif aux temps courts est perdu uniquement après plusieurs collisions entre particules, et non pas après une collision unique comme le laisse suggérer une hypothèse largement répandue. L'influence possible des interactions directes entre particules, même dans le régime des temps courts, est compatible avec le fait que les amplitudes observées de la fonction hydrodynamique $H(q)$ sont significativement plus basses que celles prédites par extrapolation du modèle valide pour les concentrations plus basses.

La loi d'échelle entre le temps de diffusion aux temps longs normalisé et la viscosité aux faibles taux de cisaillement, trouvé par Segrè et al. [Segrè 1995b], a été utilisé pour montrer une discordance entre les résultats obtenus dans cette thèse et un modèle qui décrit bien les données de viscosité des colloïdes à $\Phi < 0.5$. Les amplitudes des coefficients de diffusion normalisés, aux temps courts aussi bien qu'aux temps longs, se sont aussi avérés s'éloigner du comportement prédit par la théorie du couplage de modes. La dépendance de $D_0/D_L(q_m)$ avec la fraction volumique pourrait être modélisée convenablement par la loi de Vogel, Fulcher et Tammam (VFT) [Debenedetti 2001], indiquant plutôt un scénario cinétique qu'une transition vitreuse.

Nous avons également testé le possible comportement en échelle des coefficients de diffusion aux temps longs et aux temps courts, dont il a été montré que le rapport est indépendant de q dans un système similaire de sphères dures [Segrè 1996]. Il a été montré que les fonctions de diffusion intermédiaires normalisées par $D_S(q)$ se rassemblent approximativement sur une même courbe pour toutes les fractions volumiques étudiées dans cette thèse, mais seulement jusqu'au temps qui a été identifié comme le début de la diffusion aux temps longs. Le tracé du rapport $D_S(q)/D_L(q)$ en fonction de qR montre une grande dépendance avec le vecteur

d'onde, surtout dans le région de q_m où le coefficient de diffusion aux temps longs est identifié sans ambigüité. La variation avec q devient plus forte quand Φ augmente, ce qui n'exclut pas que la loi d'échelle soit valide pour des fractions volumiques inférieures à celles étudiées ici.

Une analyse plus détaillée de la fonction de corrélation mesurée pour l'échantillon le plus concentré a révélé que sa forme peut être bien décrite par une décroissance exponentielle comprimée plutôt qu'étirée, contrairement à ce qui est observé pour la relaxation α dans les liquides formant verre [Debenedetti 2001]. Après avoir indiqué d'autres exemples de comportements de ce type dans la littérature [Cipelletti 2000, Czakkel 2011], nous supposons que cette observation reste bien dans l'axe de la conclusion que le ralentissment de la dynamique est causé par un arrêt cinétique et non pas par une transition vitreuse.

Profitant des performances du détecteur 2D MEDPIX, nous avons calculé les fonctions de corrélation à deux temps, qui révèlent un comportement en vieillissement complexe, affectant toutes les échelles de longueur et de temps explorées. La structure temporelle inhabituelle des corrélations observées peut être interprétée dans le cadre du modèle "solide bloqué" comme liée à des avalanches de particules, qui relaxent les contraintes accumulées au cours du temps. Il est important de souligner que les fonctions de corrélation régulières moyennées dans le temps, typiquement utilisées dans ce type d'études, conduiraient inévitablement à des conclusions trompeuses si elles étaient appliquées à cette dynamique non stationnaire.

Il serait intéressant de continuer la recherche dans les directions indiquées dans cette thèse. Construire un dispositif dédié permettant les expériences sous écoulement, et l'utiliser pour étudier les suspensions colloïdales concentrées, pourrait mener à une compréhension meilleure des influences réciproques entre la dynamique et la rhéologie dans ces systèmes. Elargir la gamme des fractions volumiques étudiées faciliterait la comparaison avec les théories et résultats expérimentaux déjà existants. Une méthode d'analyse plus quantitative des fonctions de corrélation à deux temps devrait être développée afin d'exploiter au mieux leurs propriétés uniques.

Conclusions and outlook

The subject of this thesis project was to study the dynamic behaviour of a colloidal suspension of hard sphere particles. More specifically, the complex dynamics at high particle volume fractions was targeted, with the goal of giving insight into the phenomena of the observed dynamical arrest, not accompanied by any structural signature. The techniques employed included Small-Angle X-ray Scattering (SAXS) and X-ray Photon Correlation Spectroscopy (XPCS), with the latter being for the first time applied to hard-sphere colloids at so high volume fractions ($0.5 \lesssim \Phi \lesssim 0.6$). The most important conclusion of this thesis is the observed lack of the relaxation time divergence at concentrations near the MCT predicted glass transition value (~ 0.58). The volume fractions dependence of $D_0/D_L(q_m)$ could be well modelled with the VFT form [Debenedetti 2001]. Together with the observed change of shape of the intermediate scattering function to compressed exponential decay, this points towards a kinetic scenario of jamming rather than a glass transition.

A combination of a simple flow device and XPCS demonstrated the possibility of simultaneous measurements of both the diffusive dynamics and the advective response to the applied shear. This technique, here applied to a dilute suspension, would be very interesting to use with concentrated colloids which demonstrate non--Newtonian flow behaviour. Apart from the pure interest of studying the shear and dynamic behaviour and their interplay, the flow of the sample during data acquisition would also be a very practical way of avoiding radiation damage of the sample. This is demonstrated in a qualitative manner in figure 5.26, which shows the time evolution of SAXS patterns during a typical XPCS data series. The data presented in the upper panel were acquired on a sample without any flow. A systematic increase of intensity with time can be observed in the low q region, indicating growth of particle clusters. This clearly changes when the sample is flowing during the measurement, as depicted in the lower panel of figure 5.26, where all the curves are the same. Radiation damage is avoided by constantly renewing the sample. However, this method has its limitations. For XPCS the presence of flow introduces a decorrelation mechanism additional to diffusion – the advective motion of particles. If the characteristic time scales corresponding to these processes are not well separated it may be impossible to distinguish them and draw any useful conclusions about the dynamics of the scatterers. This is a valid problem in the case of concentrated colloidal suspensions, where the dynamics becomes very slow. Imposing a flow of the sample may then lead to a complete decorrelation of the measured intermediate scattering function simply due to the translational motion of the particles through the scattering volume. Such a measurement contains no useful information. Technical limitations should also be considered – it may not be

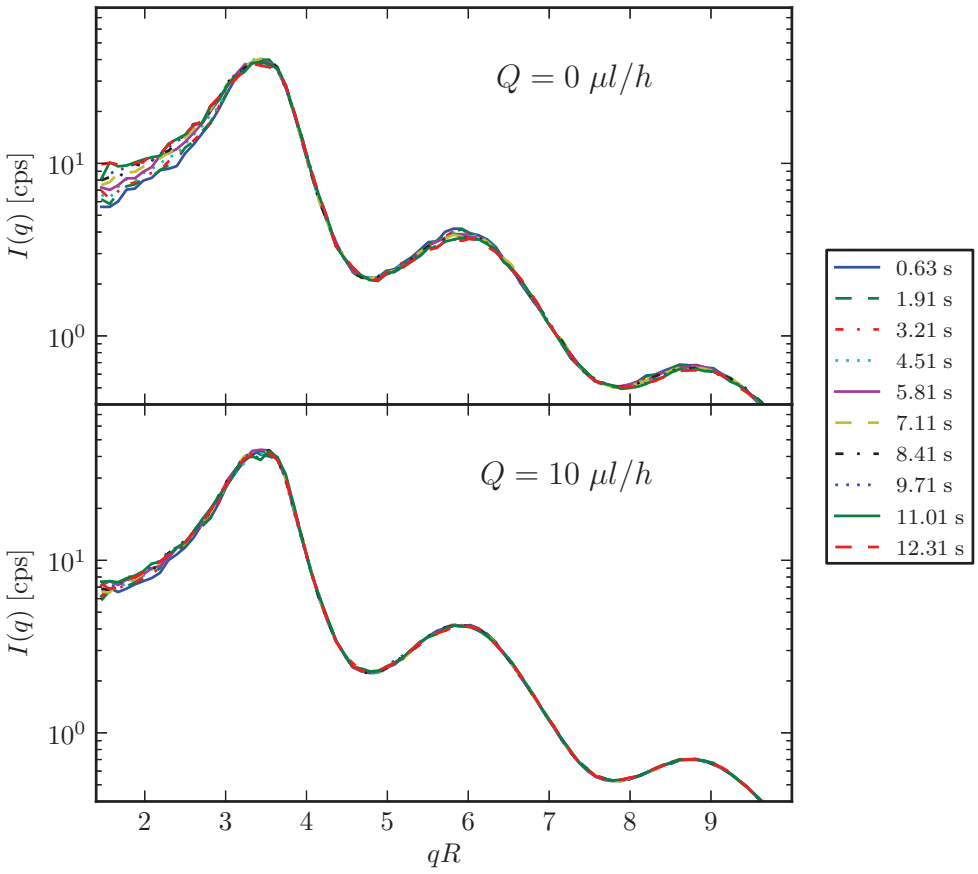

Figure 5.26: SAXS evolution during a measurement series taken with and without flow.

feasible to apply a continuous flow slow enough to perform the experiment.

By utilizing the unique properties of a third generation synchrotron radiation source and the fast, single photon counting MAXIPIX detector available at the ID10 beamline of the European Synchrotron Radiation Facility (ESRF), it was possible to measure the intermediate scattering functions in a range of scattering vector values and sample concentrations not easily accessible for other techniques. Sample volume fractions were determined by fitting the time- and azimuthally-averaged radial profiles of the scattering pattern. The characteristic, two-step decay of the intermediate scattering functions was observed. By representing the data in the form of width functions the character of the relaxations could be determined

without assuming an arbitrary model. In the short-time limit an exponential decay could be seen for all sample concentrations in a wide q range. However, in the long times an approximately exponential decay could be distinguished for each sample only near $q = q_m$. It persisted in higher q values only in the sample at highest Φ probed (0.597).

An analysis of the limiting time scales extracted from the width functions with a simple numerical procedure showed that the short-time diffusive regime is lost only after several particle collisions. This is in conflict with the commonly accepted assumption that a single encounter breaks the diffusive character of particle motion. Possible influence of direct particle interactions even in the short-time regime is consistent with the observed amplitudes of the hydrodynamic function $H(q)$ being significantly lower than predicted by extrapolating a model valid for lower concentrations.

The scaling between the normalized long-time diffusion coefficient and low-shear-rate viscosity found by Segrè *et al.* [Segrè 1995b] was used to show a discrepancy between the results obtained in this thesis and a model well describing viscosity data of colloids at $\Phi \lesssim 0.5$. The amplitudes of both normalized short- and long-time diffusion coefficient were also shown to depart from the behaviour predicted by the MCT.

We also tested the putative scaling of the short- and long-time diffusion coefficients, which ratio has been found to be q independent in a similar system of hard-sphere particles [Segrè 1996]. The intermediate scattering functions normalized by $D_S(q)$ were shown to approximately collapse for all volume fractions studied in this thesis, but only upto the time which has been identified as the onset of long-time diffusion. A plot of the $D_S(q)/D_L(q)$ ratio vs qR shows important wavevector dependence, particularly in the region of q_m, where the long-time diffusion coefficient is unambiguously identified. The variation with q becomes stronger with increasing Φ, which does not exclude that the scaling may be valid for volume fractions lower than the ones studied here.

A more detailed analysis of the correlation function measured for the most concentrated sample revealed that its shape can be well described by a compressed exponential decay rather than a stretched one, typically observed for the α relaxation in glass-forming liquids [Debenedetti 2001]. After pointing to other examples of such behaviour found in literature ([Cipelletti 2000, Czakkel 2011]) we postulate that this observation remains well in line with the conclusion that the slowing down of the dynamics is caused by a kinetic arrest and not glass transition.

Taking the advantage of the MEDPIX area detector we calculated two-time correlation functions which revealed a complex ageing behaviour, affecting all length and time scales probed The unusual time structure of the correlations observed can be interpreted within the "jammed solid" model as particle avalanches, releasing stress accumulated over time. It is important to stress that regular time averaged correlation functions, typically employed in such studies, would inevitably lead to misleading conclusions when applied to this non-stationary dynamics.

It would be interesting to continue the research in the directions pointed in

this thesis. Building a dedicated sample environment enabling experiments under flow and using it to study concentrated colloidal suspensions could lead to a better understanding of the interplay between dynamics and rheology in these systems. Broadening the range of volume fractions studied would facilitate the comparison with existing experimental results and theories. A more quantitative method of two-time correlation function analysis should be developed to exploit their unique properties.

Bibliography

[Ackerson 1981] B.J. Ackerson and N.A. Clark. *Dynamic light scattering at low rates of shear*. J. Phys. France, vol. 42, no. 7, pages 929–936, 1981. (Cited on page 44.)

[Als-Nielsen 2011] Jens Als-Nielsen and Des McMorrow. Elements of modern x-ray physics. John Wiley & Sons, Ltd, second édition, 2011. (Cited on pages 3, 4, 5, 9, 15 and 16.)

[Antl 1986] L. Antl, J.W. Goodwin, R.D. Hill, R.H. Ottewill, S.M. Owens, S. Papworth and J.A. Waters. *The preparation of poly(methyl methacrylate) latices in non-aqueous media*. Colloids and Surfaces, vol. 17, no. 1, pages 67 – 78, 1986. (Cited on pages 30 and 35.)

[Aragon 1976] S R Aragon and R Pecora. *Theory of dynamic light scattering from polydisperse systems*. Journal of Chemical Physics, vol. 64, no. 6, pages 2395–2404, March 1976. (Cited on pages 8 and 10.)

[Banchio 1999a] A. J. Banchio, J. Bergenholtz and G. Nägele. *Rheology and Dynamics of Colloidal Suspensions*. Phys. Rev. Lett., vol. 82, pages 1792–1795, Feb 1999. (Cited on pages 41 and 57.)

[Banchio 1999b] Adolfo J. Banchio, Gerhard Nägele and Johan Bergenholtzbra. *Viscoelasticity and generalized Stokes–Einstein relations of colloidal dispersions*. The Journal of Chemical Physics, vol. 111, no. 18, pages 8721–8740, 1999. (Cited on pages 40, 57 and 69.)

[Banchio 2003] Adolfo J. Banchio and John F. Brady. *Accelerated Stokesian dynamics: Brownian motion*. The Journal of Chemical Physics, vol. 118, no. 22, pages 10323–10332, 2003. (Cited on page 68.)

[Banchio 2008] Adolfo J. Banchio and Gerhard Nagele. *Short-time transport properties in dense suspensions: From neutral to charge-stabilized colloidal spheres*. The Journal of Chemical Physics, vol. 128, no. 10, page 104903, 2008. (Cited on pages 40, 57 and 68.)

[Bartlett 1992] P. Bartlett and R. H. Ottewill. *A neutron scattering study of the structure of a bimodal colloidal crystal*. Journal of Chemical Physics, vol. 96, no. 4, pages 3306–3318, February 1992. (Cited on page 35.)

[Beenakker 1983] C.W.J. Beenakker and P. Mazur. *Self-diffusion of spheres in a concentrated suspension*. Physica A: Statistical Mechanics and its Applications, vol. 120, no. 3, pages 388 – 410, 1983. (Cited on pages 40 and 57.)

[Beenakker 1984] C.W.J. Beenakker and P. Mazur. *Diffusion of spheres in a concentrated suspension II*. Physica A: Statistical Mechanics and its Applications, vol. 126, no. 3, pages 349 – 370, 1984. (Cited on pages 40, 57 and 76.)

[Bellour 2003] M. Bellour, A. Knaebel, J. L. Harden, F. Lequeux and J.-P. Munch. *Aging processes and scale dependence in soft glassy colloidal suspensions*. Phys. Rev. E, vol. 67, no. 3, page 031405, Mar 2003. (Cited on page 83.)

[Berne 2000] Bruce J. Berne and Robert Pecora. Dynamic light scattering with application to chemistry, biology and physics. Dover Publications, New York, 2000. (Cited on pages x, xi, 13, 21 and 45.)

[Blum 1979] L. Blum and G. Stell. *Polydisperse systems. I. Scattering function for polydisperse fluids of hard or permeable spheres.* The Journal of Chemical Physics, vol. 71, no. 1, pages 42–46, 1979. (Cited on page 10.)

[Bouchaud 2002] J.-P. Bouchaud and E. Pitard. *Anomalous dynamical light scattering in soft glassy gels.* The European Physical Journal E: Soft Matter and Biological Physics, vol. 9, pages 287–291, 2002. 10.1140/epje/i2002-10075-3. (Cited on page 81.)

[Brambilla 2009] G. Brambilla, D. El Masri, M. Pierno, L. Berthier, L. Cipelletti, G. Petekidis and A. B. Schofield. *Probing the Equilibrium Dynamics of Colloidal Hard Spheres above the Mode-Coupling Glass Transition.* Phys. Rev. Lett., vol. 102, page 085703, Feb 2009. (Cited on pages 58, 72 and 73.)

[Busch 2008] S Busch, T H Jensen, Y Chushkin and A Fluerasu. *Dynamics in shear flow studied by X-ray Photon Correlation Spectroscopy.* The European physical journal. E, Soft matter, vol. 26, no. 1-2, pages 55–62, 2008. (Cited on pages 42, 43 and 46.)

[Chen 1986] S. H. Chen. *Small Angle Neutron Scattering studies of the structure and interaction in micellar and microemulsion systems.* Ann. Rev. Phys. Chem., vol. 37, pages 351–399, 1986. (Cited on page 62.)

[Chen 2002] Wei-Ren Chen, Sow-Hsin Chen and Francesco Mallamace. *Small-angle neutron scattering study of the temperature-dependent attractive interaction in dense L64 copolymer micellar solutions and its relation to kinetic glass transition.* Phys. Rev. E, vol. 66, no. 2, page 021403, Aug 2002. (Cited on page 10.)

[Cheng 2002] Zhengdong Cheng, Jixiang Zhu, Paul M. Chaikin, See-Eng Phan and William B. Russel. *Nature of the divergence in low shear viscosity of colloidal hard-sphere dispersions.* Phys. Rev. E, vol. 65, page 041405, Apr 2002. (Cited on page 73.)

[Cipelletti 1999] Luca Cipelletti and D. A. Weitz. *Ultralow-angle dynamic light scattering with a charge coupled device camera based multispeckle, multitau correlator.* Review of Scientific Instruments, vol. 70, no. 8, pages 3214–3221, 1999. (Cited on page 26.)

[Cipelletti 2000] L. Cipelletti, S. Manley, R. C. Ball and D. A. Weitz. *Universal Aging Features in the Restructuring of Fractal Colloidal Gels.* Physical Review Letters, vol. 84, no. 10, page 2275, 2000. (Cited on pages 81, 91 and 94.)

[Cipelletti 2003] Luca Cipelletti, H. Bissig, V. Trappe, P. Ballesta and S. Mazoyer. *Time-resolved correlation: a new tool for studying temporally heterogeneous dynamics.* Journal of Physics: Condensed Matter, vol. 15, pages S257–S262, 2003. (Cited on page 81.)

[Cohen 1997] E.G.D. Cohen, R. Verberg and I.M. de Schepper. *Newtonian viscosity and visco-elastic behavior of concentrated neutral hard-sphere colloidal suspensions.* International Journal of Multiphase Flow, vol. 23, no. 4, pages 797 – 807, 1997. (Cited on page 70.)

[Czakkel 2011] O. Czakkel and A. Madsen. *Evolution of dynamics and structure during formation of a cross-linked polymer gel.* EPL, vol. 95, no. 2, page 28001, 2011. (Cited on pages 81, 84, 91 and 94.)

[Debenedetti 2001] Pablo G. Debenedetti and Frank H. Stillinger. *Supercooled liquids and the glass transition.* Nature, vol. 410, no. 6825, pages 259–267, March 2001. (Cited on pages 71, 81, 90, 91, 92 and 94.)

[Duri 2006] A. Duri and L. Cipelletti. *Length scale dependence of dynamical heterogeneity in a colloidal fractal gel.* EPL (Europhysics Letters), vol. 76, no. 5, page 972, 2006. (Cited on pages 23 and 81.)

[Einstein 1905] A. Einstein. *Über die von der molekularkinetischen Theorie der Wärme geforderte Bewegung von in ruhenden Flüssigkeiten suspendierten Teilchen.* Annalen der Physik, vol. 322, no. 8, pages 549–560, 1905. (Cited on page 21.)

[Fluerasu 2008] Andrei Fluerasu, Abdellatif Moussaïd, Henri Gleyzolle and Anders Madsen. *X-ray photon correlation spectroscopy under flow.* J. Synchrotron Rad., vol. 15, pages 378–384, 2008. (Cited on page 43.)

[Fluerasu 2010] Andrei Fluerasu, Pawel Kwasniewski, Chiara Caronna, Fanny Destremaut, Jean-Baptiste Salmon and Anders Madsen. *Dynamics and rheology under continuous shear flow studied by x-ray photon correlation spectroscopy.* New Journal of Physics, vol. 12, no. 3, page 035023, 2010. (Cited on pages x, xi, xiv, xvii, xviii, 42 and 43.)

[Fuchs 1999] M. Fuchs and M. R. Mayr. *Aspects of the dynamics of colloidal suspensions: Further results of the mode-coupling theory of structural relaxation.* Phys. Rev. E, vol. 60, pages 5742–5752, Nov 1999. (Cited on pages xiii, xvii, 57 and 76.)

[Fuller 1980] G. Fuller G., M. Rallison J., L. Schmidt R. and G. Leal L. *The measurement of velocity gradients in laminar flow by homodyne light-scattering spectroscopy.* J. Fluid Mech., vol. 100, pages 555–575, 1980. (Cited on pages 43 and 44.)

[Glatter 1982] O. Glatter and O. Kratky, editeurs. Small angle x-ray scattering. Academic Press (London), 1982. (Cited on pages 4 and 6.)

[Goodman 2005] J.W. Goodman. Introduction to fourier optics. McGraw-Hill physical and quantum electronics series. Roberts & Co., 2005. (Cited on page 17.)

[Götze 1991] W. Götze and L. Sjögren. *β relaxation at the glass transition of hard-spherical colloids.* Phys. Rev. A, vol. 43, pages 5442–5448, May 1991. (Cited on pages 57, 72 and 76.)

[Götze 1999] W. Götze. *Recent tests of the mode-coupling theory for glassy dynamics*. Journal of Physics: Condensed Matter, vol. 11, no. 10A, page A1, 1999. (Cited on pages 41 and 57.)

[Griffith 1986] W L Griffith, R Triolo and A L Compere. *Analytical structure function of a polydisperse Percus-Yevick fluid with Shulz (gamma) distributed diameters*. Phys. Rev. A, vol. 33, no. 3, page 2197, 1986. (Cited on pages 62 and 66.)

[Griffith 1987] W L Griffith, R Triolo and A L Compere. *Analytical scattering function of a polydisperse Percus-Yevick fluid with Shulz- (Γ-) distributed diameters*. Phys. Rev. A, vol. 35, no. 5, page 2200, 1987. (Cited on pages 10, 11, 35, 37 and 61.)

[Grübel 2004] Gerhard Grübel and Federico Zontone. *Correlation spectroscopy with coherent X-rays*. Journal of Alloys and Compounds, vol. 362, no. 1-2, pages 3 – 11, 2004. Proceedings of the Sixth International School and Symposium on Synchrotron Radiation in Natural Science (ISSRNS). (Cited on page 16.)

[Grübel 2008] G. Grübel, A. Madsen and Robert A. Soft matter characterization, chapitre 18, pages 953–995. Springer Netherlands, 2008. (Cited on pages 20 and 25.)

[Hess 1980] W Hess and R Klein. *Long-time versus short-time behaviour of a system of interacting Brownian particles*. Journal of Physics A: Mathematical and General, vol. 13, no. 1, page L5, 1980. (Cited on page 40.)

[Hess 1983] W. Hess and R. Klein. *Generalized hydrodynamics of systems of Brownian particles*. Advances in Physics, vol. 32, no. 2, pages 173–283, 1983. (Cited on page 40.)

[Holmqvist 2010] Peter Holmqvist and Gerhard Nägele. *Long-Time Dynamics of Concentrated Charge-Stabilized Colloids*. Phys. Rev. Lett., vol. 104, no. 5, page 058301, Feb 2010. (Cited on pages xiii, xvii and 75.)

[Hunter 1989] R.J. Hunter. Foundations of colloid science. Numeéro v. 1 de Foundations of Colloid Science. Clarendon Press, 1989. (Cited on page 32.)

[Hunter 1990] R.J. Hunter and L.R. White. Foundations of colloid science. Numeéro v. 1 de Foundations of Colloid Science. Clarendon Press, 1990. (Cited on page 30.)

[Jackson 1998] J.D. Jackson. Classical electrodynamics. Wiley, 3 édition, 1998. (Cited on page 5.)

[Kasper 1998] Andreas Kasper, Eckhard Bartsch and Hans Sillescu. *Self-Diffusion in Concentrated Colloid Suspensions Studied by Digital Video Microscopy of CoreShell Tracer Particles*. Langmuir, vol. 14, no. 18, pages 5004–5010, 1998. (Cited on page 40.)

[Klein 1996] Rudolf Klein and Bruno D'Aguano. Light scattering. principles and development. Oxford University Press, 1996. Shelfmark in the library: 17.9/44. (Cited on pages 9 and 10.)

[Klein 2002] R Klein. Neutrons, x-rays and light: Scattering methods applied to soft condensed matter, chapitre 14, pages 351–379. North-Holland, 2002. (Cited on page 10.)

[Kotlarchyk 1983] M. Kotlarchyk and S.-H. Chen. *Analysis of small angle neutron scattering spectra from polydisperse interacting colloids.* Journal of Chemical Physics, vol. 79, page 2461, 1983. (Cited on page 8.)

[Leheny 2012] Robert L. Leheny. *XPCS: Nanoscale motion and rheology.* Current Opinion in Colloid & Interface Science, vol. 17, no. 1, pages 3 – 12, 2012. (Cited on page 14.)

[Lengeler 2001] B Lengeler. *Coherence in X-ray physics.* Naturwissenschaften, vol. 88, no. 6, pages 249–60–, June 2001. (Cited on page 17.)

[Lide 2010] D.R. Lide, editeur. Crc handbook of chemistry and physics. CRC Press, 2010. (Cited on pages 13, 35 and 48.)

[Lindner 2002] P. Lindner and Th. Zemb, editeurs. Neutrons, x-rays and light: Scattering methods applied to soft condensed matter. North-Holland, 2002. (Cited on page 6.)

[Löwen 1994] Hartmut Löwen. *Melting, freezing and colloidal suspensions.* Physics Reports, vol. 237, no. 5, pages 249–324, 1994. (Cited on page 31.)

[Lumma 2000a] D. Lumma, L. B. Lurio, M. A. Borthwick, P. Falus and S. G. J. Mochrie. *Structure and dynamics of concentrated dispersions of polystyrene latex spheres in glycerol: Static and dynamic x-ray scattering.* Phys. Rev. E, vol. 62, pages 8258–8269, Dec 2000. (Cited on page 76.)

[Lumma 2000b] D. Lumma, L. B. Lurio, S. G. J. Mochrie and M. Sutton. *Area detector based photon correlation in the regime of short data batches: Data reduction for dynamic x-ray scattering.* Review of Scientific Instruments, vol. 71, no. 9, pages 3274–3289, 2000. (Cited on page 25.)

[Lurio 2000] L. B. Lurio, D. Lumma, A. R. Sandy, M. A. Borthwick, P. Falus, S. G. J. Mochrie, J. F. Pelletier, M. Sutton, Lynne Regan, A. Malik and G. B. Stephenson. *Absence of Scaling for the Intermediate Scattering Function of a Hard-Sphere Suspension: Static and Dynamic X-Ray Scattering from Concentrated Polystyrene Latex Spheres.* Phys. Rev. Lett., vol. 84, no. 4, pages 785–788, Jan 2000. (Cited on pages xiii, xvii, 75, 76 and 77.)

[Madsen 2010] Anders Madsen, Robert L Leheny, Hongyu Guo, Michael Sprung and Orsolya Czakkel. *Beyond simple exponential correlation functions and equilibrium dynamics in x-ray photon correlation spectroscopy.* New Journal of Physics, vol. 12, no. 5, page 055001, 2010. (Cited on pages 22, 23, 24 and 81.)

[Martinez 2008] V. A. Martinez, G. Bryant and W. van Megen. *Slow Dynamics and Aging of a Colloidal Hard Sphere Glass.* Phys. Rev. Lett., vol. 101, no. 13, page 135702, Sep 2008. (Cited on page 62.)

[Martinez 2011] V. A. Martinez, J. H. J. Thijssen, F. Zontone, W. van Megen and G. Bryant. *Dynamics of hard sphere suspensions using dynamic light scattering and X-ray photon correlation spectroscopy: Dynamics and scaling of the intermediate scattering function.* The Journal of Chemical Physics, vol. 134, no. 5, page 054505, 2011. (Cited on pages x, xi, xiii, xvii, 62, 63, 76 and 77.)

[Medina-Noyola 1988] M. Medina-Noyola. *Long-Time Self-Diffusion in Concentrated Colloidal Dispersions.* Phys. Rev. Lett., vol. 60, pages 2705–2708, Jun 1988. (Cited on pages 40 and 57.)

[Narayanan 1997] Theyencheri Narayanan, Cecil Cheung, Penger Tong, Walter I. Goldburg and Xiao lun Wu. *Measurement of the velocity difference by photon correlation spectroscopy: an improved scheme.* Appl. Opt., vol. 36, no. 30, pages 7639–7644, Oct 1997. (Cited on page 46.)

[Narayanan 2008] T. Narayanan. Soft matter characterization, chapitre 17, pages 899–952. Springer Netherlands, 2008. (Cited on pages 4, 6, 7, 10 and 36.)

[Onsager 1933] Lars. Onsager. *Theories of Concentrated Electrolytes.* Chemical Reviews, vol. 13, no. 1, pages 73–89, 1933. (Cited on page 30.)

[Orsi 2012a] D. Orsi, L. Cristofolini, G. Baldi and A. Madsen. *Heterogeneous and Anisotropic Dynamics of a 2D Gel.* Phys. Rev. Lett., vol. 108, page 105701, Mar 2012. (Cited on page 84.)

[Orsi 2012b] Davide Orsi, Andrei Fluerasu, Abdellatif Moussaïd, Federico Zontone, Luigi Cristofolini and Anders Madsen. *Dynamics in dense hard-sphere colloidal suspensions.* Phys. Rev. E, vol. 85, page 011402, Jan 2012. (Cited on pages x, xi, 40, 57, 58, 69, 70 and 72.)

[Pedersen 1997] Jan Skov Pedersen. *Analysis of small-angle scattering data from colloids and polymer solutions: modeling and least-squares fitting.* Advances in Colloid and Interface Science, vol. 70, pages 171 – 210, 1997. (Cited on pages 7 and 9.)

[Phan 1996] See-Eng Phan, William B. Russel, Zhengdong Cheng, Jixiang Zhu, Paul M. Chaikin, John H. Dunsmuir and Ronald H. Ottewill. *Phase transition, equation of state, and limiting shear viscosities of hard sphere dispersions.* Phys. Rev. E, vol. 54, pages 6633–6645, Dec 1996. Test of hard-sphere behavior of the PMMA particles. (Cited on pages 58 and 71.)

[Pine 1988] D. J. Pine, D. A. Weitz, P. M. Chaikin and E. Herbolzheimer. *Diffusing wave spectroscopy.* Phys. Rev. Lett., vol. 60, pages 1134–1137, Mar 1988. (Cited on page 14.)

[Ponchut 2011] C Ponchut, J M Rigal, J Clément, E Papillon, A Homs and S Petitdemange. *MAXIPIX, a fast readout photon-counting X-ray area detector for synchrotron applications.* Journal of Instrumentation, vol. 6, no. 01, page C01069, 2011. (Cited on page 25.)

[Poon 2012] Wilson C. K. Poon, Eric R. Weeks and C. Patrick Royall. *On measuring colloidal volume fractions*. Soft Matter, vol. 8, pages –, 2012. (Cited on pages 36, 70 and 73.)

[Pusey 1986] P. N. Pusey and W. van Megen. *Phase behaviour of concentrated suspensions of nearly hard colloidal spheres*. Nature, vol. 320, no. 6060, pages 340–342, March 1986. (Cited on pages x, xi, xii, xvi, 33 and 35.)

[Pusey 1987] P. N. Pusey and W. van Megen. *Observation of a glass transition in suspensions of spherical colloidal particles*. Phys. Rev. Lett., vol. 59, pages 2083–2086, Nov 1987. (Cited on pages x, xi, xii and xvi.)

[Pusey 1989] P.N. Pusey and W. Van Megen. *Dynamic light scattering by non-ergodic media*. Physica A: Statistical Mechanics and its Applications, vol. 157, no. 2, pages 705 – 741, 1989. (Cited on page 27.)

[Pusey 1991] P. N. Pusey. Liquids, freezing and glass transition. North-Holland, 1991. (Cited on pages xii, xvi, 21, 30, 31, 32, 33, 38, 39, 40, 56 and 66.)

[Pusey 1997] P. Pusey, P. Segre, O. Behrend, S. Meeker and W. Poon. *Hard-sphere colloidal suspensions studied by two-colour dynamic light scattering*. Progr Colloid Polym Sci, vol. 104, pages 8–11, 1997. 10.1007/BFb0110738. (Cited on page 56.)

[Pusey 2002] P N Pusey. Neutrons, x-rays and light: Scattering methods applied to soft condensed matter, chapitre 1, pages 3–21. North-Holland, 2002. (Cited on page 3.)

[Robert 2008] A. Robert, J. Wagner, W. Härtl, T. Autenrieth and G. Grübel. *Dynamics in dense suspensions of charge-stabilized colloidal particles*. Eur. Phys. J. E, vol. 25, no. 1, pages 77–81, 2008. (Cited on page 75.)

[Sanborn 2011] Christopher Sanborn, Karl F. Ludwig, Michael C. Rogers and Mark Sutton. *Direct Measurement of Microstructural Avalanches during the Martensitic Transition of Cobalt Using Coherent X-Ray Scattering*. Phys. Rev. Lett., vol. 107, no. 1, page 015702, Jun 2011. (Cited on page 85.)

[Schaertl 1994] W. Schaertl and H. Sillescu. *Brownian dynamics of polydisperse colloidal hard spheres: Equilibrium structures and random close packings*. Journal of Statistical Physics, vol. 77, pages 1007–1025, 1994. 10.1007/BF02183148. (Cited on pages 65 and 72.)

[Segrè 1995a] P. N. Segrè, O. P. Behrend and P. N. Pusey. *Short-time Brownian motion in colloidal suspensions: Experiment and simulation*. Phys. Rev. E, vol. 52, no. 5, pages 5070–5083, Nov 1995. (Cited on pages 36, 40, 57, 58, 68 and 75.)

[Segrè 1995b] P. N. Segrè, S. P. Meeker, P. N. Pusey and W. C. K. Poon. *Viscosity and Structural Relaxation in Suspensions of Hard-Sphere Colloids*. Phys. Rev. Lett., vol. 75, pages 958–961, Jul 1995. (Cited on pages 70, 90 and 94.)

[Segrè 1995c] P.N. Segrè P. N., W. Van Megen, P.N. Pusey, K. Schtzel and W. Peters. *Two-colour Dynamic Light Scattering*. Journal of Modern Optics, vol. 42, no. 9, pages 1929–1952, 1995. (Cited on pages xii, xvi and 14.)

[Segrè 1996] P. N. Segrè and P. N. Pusey. *Scaling of the Dynamic Scattering Function of Concentrated Colloidal Suspensions*. Phys. Rev. Lett., vol. 77, no. 4, pages 771–774, Jul 1996. (Cited on pages x, xi, xii, xiii, xvi, xvii, 54, 62, 73, 74, 75, 76, 77, 78, 90 and 94.)

[Spiga 1994] M. Spiga and G. L. Morini. *A symmetric solution for velocity profile in laminar flow through rectangular ducts*. International Communications in Heat and Mass Transfer, vol. 21, no. 4, pages 469–475, 1994. (Cited on page 46.)

[Sutton 2002] M. Sutton. Third-generation hard x-ray synchrotron radiation sources, source properties, optics and experimental techniques. Wiley, 2002. (Cited on page 20.)

[Sutton 2003] Mark Sutton, Khalid Laaziri, F. Livet and F. Bley. *Using coherence to measure two-time correlation functions*. Opt. Express, vol. 11, no. 19, pages 2268–2277, Sep 2003. (Cited on page 22.)

[Tokuyama 1995] Michio Tokuyama and Irwin Oppenheim. *On the theory of concentrated hard-sphere suspensions*. Physica A: Statistical Mechanics and its Applications, vol. 216, no. 1Ǎ0132, pages 85 – 119, 1995. (Cited on pages 40 and 57.)

[van Megen 1991] W. van Megen and P. N. Pusey. *Dynamic light-scattering study of the glass transition in a colloidal suspension*. Phys. Rev. A, vol. 43, pages 5429–5441, May 1991. (Cited on pages xii and xvi.)

[van Megen 1994] W. van Megen and S. M. Underwood. *Glass transition in colloidal hard spheres: Measurement and mode-coupling-theory analysis of the coherent intermediate scattering function*. Phys. Rev. E, vol. 49, pages 4206–4220, May 1994. (Cited on pages xii, xvi, 40, 41 and 57.)

[van Megen 1998] W. van Megen, T. C. Mortensen, S. R. Williams and J. Müller. *Measurement of the self-intermediate scattering function of suspensions of hard spherical particles near the glass transition*. Phys. Rev. E, vol. 58, pages 6073–6085, Nov 1998. (Cited on pages 58 and 73.)

[van Megen 2005] W. van Megen, T. C. Mortensen and G. Bryant. *Change in relaxation scenario at the order-disorder transition of a colloidal fluid of hard spheres seen from the Gaussian limit of the self-intermediate scattering function*. Phys. Rev. E, vol. 72, page 031402, Sep 2005. (Cited on page 65.)

[van Megen 2007a] W. van Megen. *Comparison of dynamic light scattering measurements and mode-coupling theory for the tagged particle dynamics of a hard-sphere suspension*. Phys. Rev. E, vol. 76, page 061401, Dec 2007. (Cited on page 72.)

[van Megen 2007b] W. van Megen and G. Bryant. *Dynamical heterogeneity and the freezing transition in hard-sphere suspensions: Further analysis of the mean square displacement and the velocity autocorrelation function*. Phys. Rev. E, vol. 76, page 021402, Aug 2007. (Cited on page 41.)

[Verberg 1999] R. Verberg, I. M. de Schepper and E. G. D. Cohen. *Theory of long-time wave number dependent diffusion coefficients in concentrated neutral colloidal suspensions*. EPL (Europhysics Letters), vol. 48, no. 4, page 397, 1999. (Cited on page 76.)

[Verberg 2000] R. Verberg, I. M. de Schepper and E. G. D. Cohen. *Diffusion of concentrated neutral hard-sphere colloidal suspensions*. Phys. Rev. E, vol. 61, pages 2967–2976, Mar 2000. (Cited on page 76.)

[Woodcock 1981] Leslie V. Woodcock. *Glass transition in the hard-sphere model and Kauzmann's paradox*. Annals of the New York Academy of Sciences, vol. 371, no. 1, pages 274–298, 1981. (Cited on page 33.)

[Zhang 2006] Hai-yan Zhang and Hong-ru Ma. *Dynamics of the colloidal suspensions*. Frontiers of Physics in China, vol. 1, pages 186–203, 2006. 10.1007/s11467-006-0003-2. (Cited on pages 40 and 56.)

[Zontone] F. *et al.* Zontone. (Cited on page 72.)